Spectral Characterization of Solid-State Photocathode Emission

BY

Gowri Dulanjalee Adhikari
B.S., University of Peradeniya, 2015
M.S., University of Illinois at Chicago, 2018

THESIS

Submitted as partial fulfillment of the requirements
for the degree of Doctor of Philosophy in Physics
in the Graduate College of the
University of Illinois at Chicago, 2020

Chicago, Illinois.

Defense Committee:

W. Andreas Schroeder chair and advisor
Robert Klie
Richard Cavanaugh
Hyowon Park
Linda Spentzouris (Illinois Institute of Technology)

I dedicate this thesis to my wonderful husband, Srinath: Without his patience, understanding, support, and love, the completion of this work would not have been possible; and to my son, Leo: who kept me happy with his innocent smile and hugs.

ACKNOWLEDGEMENT

I would like to take this opportunity to express my profound gratitude and deep regard to my supervisor Prof. Andreas Schroeder for his exemplary guidance, valuable feedback, constant encouragement throughout my Ph.D., and sharing your knowledge with me. You were a great mentor, and I was lucky to work under you. I thank all my committee members, Prof. Robert Klie, Prof. Richard Cavanaugh, Prof. Hyowon Park, and Prof. Linda Spentzouris; I appreciate your time and the value you brought to my work. I owe a special thanks to Prof. Linda Spentzouris, for working with me on a collaborative project and being a part of my thesis committee. I also acknowledge Prof. Howard Padmore from the LBNL, Prof. Siddharth Karkare from Arizona State University, Prof. Sergey Baryshew from Michigan State University, Dr. Alice Galdi from Cornell University and Chen Gongxiaohui from IIT for working with me on several collaborative projects. Their valuable suggestions were of immense help throughout my research work, and also their perceptive criticism kept me working to do this research in a much better way. Working under them was an extremely knowledgeable experience for me. I am highly indebted to the machine shop people, especially Kevin Lynch and Rick Frueh, to provide their expertise. I owe a special thanks to an undergraduate student, Penelope Riely, to help me with small tasks and a graduate student, Eric Mascot, and Dr. Tuo Li, for giving me the first guidance to DFT. I would also like to give my sincere gratitude to my parents, my family, and colleagues for their encouragement, unconditional love, and support, without which this research would be incomplete.

TABLE OF CONTENTS

LIST OF TABLES

TABLE **PAGE**

LIST OF FIGURES

FIGURE **PAGE**

LIST OF ABBREVIATIONS

AES	Auger electron spectroscopy
AG	Analytical gaussian
BBO	β-Barium borate-β-$Ba(BO_2)_2$
bcc	body centered cubic
CCD	Charge-coupled device
CW	Continuous wave
DC	Direct current
DCM	Dispersion compensating mirror
DFT	Density functional theory
DTEM	Dynamic transmission electron microscope
fcc	face centered cubic
FHG	Fourth harmonic generation
FWHM	Full width half maximum
GGA	Generalized gradient approximation
GVD	Group velocity dispersion
IIT	Illinois Institute of Technology
IUPAC	International union of pure and applied chemistry
LBNL	Lawrence Berkley National Lab
LBO	Lithium triborate-LiB_3O_5
LDA	Local density approximation
LDOS	Local density of states
LEED	Low energy electron diffraction
ML	Mode-locked
ML	Mono layer

MTE	Mean transverse energy
NCPM	Non critical phase matched
NEA	Negative electron affinity
OPA	Optical parametric amplification
QE	Quantum efficiency
RMS	Root mean square
SBR	Saturable brag reflector
SCF	Self consistency calculation
SHG	Second harmonic generation
THG	Third harmonic generation
TOF	Time of flight
UED	Ultra high vacuum
UEM	Ultrafast electron microscopy
UIC	University of Illinois at Chicago
UV	Ultra-violet
XFEL	X-ray free-electron laser
YAG	Yttrium aluminium garnet $Y_3Al_5O_{12}$
Yb:KGW	Ytterbium-doped potassium tungstate

SUMMARY

The goal of this thesis work is to connect the electronic properties of a crystal (i.e. its band structure) to its photoemission properties and thereby provide a roadmap for the discovery (or development) of photocathode materials with low intrinsic emittance. Such planar pulsed-laser driven photocathodes are employed in the cutting-edge research instruments that include sub-picosecond X-ray free-electron lasers (XFELs), and single-shot dynamic transmission electron microscopes (DTEM) and ultrafast electron diffraction (UED) systems, and the quality of the front-end photoelectron source determines the performance of these instruments. I have introduced a new photoemission formalism that includes the triangular barrier generated by an applied surface acceleration field E_{acc} of the electron gun, transverse momentum conservation, and the properties of the bulk band and vacuum states involved in the photoemission process. The direct connection between the electronic band structure of a solid-state photocathode material and it's experimentally determined spectral photoemission properties (the mean transverse energy (MTE) and quantum efficiency (QE)) is shown for a Rh(110) photocathode at 300K. Similar consistency between experiment and theory is observed for the more complex multiple band emission from Mo(001) and W(001) photocathodes, although the latter requires careful consideration of relativistic and spin-orbit coupling effects in its *Ab initio* band structure calculation. In accordance with theoretical expectations, a low effective mass (i.e. high dispersion) of the bulk emission bands is shown to be the cause of the significant reduction in the MTE of photoemission from single-crystal Hf(0001) photocathode. Further, modification of the one-step photoemission formalism allowed for an explanation of the observed spectral dependence of the MTE from a Hf(0001)/HfO_2 photocathode through the inclusion of defect state emission from the native oxide layer. In addition, measurements of spectral dependence of the MTE and QE for Cu(100) were obtained at 300K and 35K using the UHV photocathode

characterization system at LBNL. A record low MTE value of 6meV was observed for Cu(001) at 35K and an excess photoemission energy ΔE of 0.11eV. Finally, it is to be noted that all the experimental data indicates that the QE does not depend on ΔE^2, as in prior photoemission analyses, due to the density of states of both the emitting bulk band and recipient vacuum states the joint density of states for the one-step photoemission transition.

CHAPTER 1

INTRODUCTION

Planar pulsed-laser driven solid-state photocathodes are employed as the front-end electron source in high space-time resolution research instruments such as sub-picosecond X-ray free-electron lasers (XFELs)[1], and single-shot dynamic transmission electron microscopes (DTEM) [2] and ultrafast electron diffraction (UED) systems. Such scientific research instruments are specifically designed to follow atomic motion with the sub-Ångstrom spatial and femtosecond temporal resolution required to capture the fastest atomic motions, including the making and breaking of chemical bonds[3]. The performance of these cutting-edge instruments is determined (and currently limited) by primarily the spatial quality of the electron source; in particular by its transverse coherence length L_c defined by $L_c = \frac{\lambda}{2\pi.\Delta\theta}$, where λ is the electron wavelength and Δθ is the rms angular spread of the beam[4] [5]. A larger transverse coherence length will provide for higher quality and higher photon energy x-ray beams generated by XFELs [6] and a significant enhancement in DTEM and UED [7] spatial resolution due to the consequent increase in the coherence of the scattered electron signal forming the image or diffraction pattern.

The transverse coherence length L_c of a photo-generated electron beam can be directly related to the mean transverse energy (MTE) of the electrons photo-emitted from a planar photocathode. For electrons with (longitudinal or z-component) momentum p_0, $\lambda = \frac{h}{p_0}$ and $\Delta\theta = \frac{\Delta p_T}{p_0}$, where h is Planck's constant and Δp_T is the one-dimensional (i.e. x or y) rms transverse momentum of the beam, we then have in this non-relativistic limit $L_c = \frac{\hbar}{\Delta p_T}$ with

$2\pi\hbar = h$. From electron beam physics, the transverse emittance, or as is more usually defined, the *normalized* transverse emittance $\varepsilon_{n,T} = \frac{1}{m_0 c}\Delta p_T . \Delta x$, where Δx is the rms transverse beam size, is conserved in propagation through high-quality (i.e. perfect) electron optics (Liouville's theorem[8]) with a lower $\varepsilon_{n,T}$ being a characteristic of a more spatially coherent beam. Thus, for a given rms laser spot size on the photocathode defining Δx, the spatial quality of an electron beam generated by a pulsed-laser driven photocathode is determined by the rms transverse momentum Δp_T of the electrons photo-emitted from the photocathode surface which is related to their mean transverse energy by $MTE = \frac{(\Delta p_T)^2}{m_0}$, with m_0 being the free electron mass. Consequently, an increase in transverse electron beam coherence length that will lead to improvements in the performance of XFELs, DTEMs and UED systems is directly tied to a reduction in the MTE of electron emission from a planar photocathode surface. The MTE is already known to be dependent upon (i) the dispersion of the electronic states of from which the electrons are emitted into the vacuum [9] (as transverse momentum is conserved in photoemission[10]), (ii) the temperature of the electron distribution in the photocathode material [11], and (iii) surface effects, such as physical [12] and chemical (surface work function variation) roughness [13], that affect the transverse momentum of the electron upon emission.

In the work presented in this thesis, I delineate a path for the development (or discovery) of the needed planar solid-state photocathodes exhibiting (ultra)low emittance (i.e. low MTE) using a combined experimental and theoretical investigation of the spectral emission properties of single-crystal metal photocathodes. Single-crystal photocathodes are employed to obtain a uniform electron beam and to remove any crystal orientation work function anisotropy issues[14]. Unlike for example Cesiated negative electron affinity (NEA) semiconductor

photocathodes[15], metal photocathodes are also generally more robust, have a longer lifetime, and exhibit prompt electron emission due in part to the short ~10nm absorption depths for the incident UV radiation required for photoemission. As a result, metal photocathodes can readily generate the sub-picosecond electron pulses needed for ultrafast electron diffraction and microscopy etc. in photo-electron guns operating in moderate (10^{-7} to 10^{-9} torr) vacuum conditions. Moreover, in many metals, including those I studied, there are no real band states at the vacuum level for the electrons to be excited into from near the Fermi level (see, for example, the Cu band structure in chapter 7). This means that photoemission may be simplified to the 'one-step' process of Mahan[16]; that is, the 'diffusive' transport step in Spicer's three-step model[17] cannot take place unless one means direct 'quantum transport' of the virtual excited state into the vacuum, which is akin to a one-step process in a 'sudden approximation' treatment.

In chapter 2, I will introduce an overview of basic photoemission theory and the prior theoretical explanations of solid-state photocathode emission characteristics; in particular, the Dowell-Schmerge theory[18], its adaptation by Vecchione[19], and the one-step photoemission process. Thereafter, a one-step photoemission analysis is developed, using the exact one-dimensional quantum solution for transmission over and through a triangular barrier presented by R.G. Forbes and H.B. Deane [*Proc. R. Soc. A* **467**, 2927 (2011)], to evaluate the emission properties of a photocathode in an electron gun. The analysis, which employs transverse momentum conservation in electron emission[10], includes the physical attributes (density of states and energy-momentum dispersion) of both the bulk band emission states and the recipient vacuum states in its evaluation of the mean transverse energy and relative quantum efficiency of the emitted electrons[20]. Moreover, I will present simulation results calculated using a Ag(100) photocathode as an exemplar to show the effect of the acceleration field, the

Fermi energy, the electron temperature, and the effective mass of the electron in the emission band. In addition, I briefly explain the *Ab initio* density functional theory (DFT) calculations that I employ to obtain the electronic band structure and work function of the single-crystal metal photocathode materials investigated in this thesis. These DFT calculations include both relativistic and spin-orbit coupling effects.

In chapter 3, I describe the experimental photocathode characterization system used to investigate the emission properties of Rh(110), Mo(001), W(001), and Hf(0001)/HfO_2 photocathodes at the University of Illinois at Chicago (UIC). This system employs a tunable ultraviolet (UV) radiation source driven by a 30 MHz repetition rate, diode-pumped, mode-locked Yb: KGW oscillator[21] to photo-emit electrons from the photocathodes in a 20 kV DC gun. The sub-picosecond UV radiation source employs a cascaded sequence of optical parametric amplification of a nonlinear fiber generated continuum and sum-frequency generation to obtain near-continuous tunability from 3.0-5.3 eV (235-410nm). The solenoid scan technique[9,21] is used to determine the spectral dependence of the MTE by fitting the measured electron beam spot size on a Ce: GAGG[22] scintillator screen (1:1 image onto a CCD camera) as a function of the focal strength of the two counter-wound cylindrical (solenoid) magnetic lenses with an extended Analytical Gaussian (AG) model[11,23,24] simulation of the electron pulse propagation. The experimental system is also equipped to measure the photocathode photoemission quantum efficiency (QE) as a function of photon energy by replacing the scintillation screen by a 5 mm diameter aperture Faraday Cup connected to a pA meter and monitoring the photoemission current as a function of the laser power incident on the solid-state photocathodes.

In chapter 4, I will present a spectral analysis of the photoemission characteristics of a face-centered cubic (fcc) single-crystal Rh(110) photocathode from below the photoemission threshold to excess photo-electron energies of $\Delta E \approx 1.0$eV. The spectral dependence of both the MTE and QE of photoemission are determined at 300K using the tunable sub-picosecond laser-based UV radiation source. The experimental data obtained for the rhodium photocathode are directly compared to expectations from the one-step photoemission model[16,20], described in chapter 2. The observed good agreement between the developed photoemission simulation and the experimental measurements represents a singular benchmarking that provides a roadmap for the development (or discovery) of new (ultra)low emittance photocathodes; that is, the demonstrated baseline for the evaluation of photocathode emission properties using *Ab initio* methods will allow for the development of screening tools to select promising solid-state photocathodes.

In chapter 5, I introduce the spectral characterization of two body-centered cubic (bcc) single-crystal metal photocathodes, Mo(001) and W(001), from near the photoemission threshold to excess photo-electron energies of $\Delta E \approx 1.5$ eV. In contrast to Rh(110) (chapter 4) and many other metal photocathodes[25], the MTE measurements for both Mo(001) and W(001) display a non-uniform increase with excess photoemission energy. This observed behavior is attributed to the dispersion characteristics of the bulk electronic band structure of the emitting states in the Γ-H direction of these bcc metal crystals again in good general agreement with the predictions of the one-step photoemission model described in chapter 2. Differences in the emission characteristics of the two photocathode materials are explained by the atomic number increase from Mo to W, which results in stronger relativistic / spin-orbit coupling effects for Tungsten. As was also noted for Rh(110) in chapter 4, the measured spectral dependence of the quantum efficiency (QE) for both single-crystal metal

photocathodes does not follow the Fowler-DuBridge quadratic dependence with excess photoemission energy[26]. In agreement with the one-step photoemission simulation, this effect is directly related to the influence of both the local density of states of the emitting electronic bands and the vacuum density of states.

In chapter 6, the spectral dependence of the mean transverse energy (MTE) of photoemission from a hexagonal close-packed (hcp) single-crystal Hf(0001) photocathode and its oxidized derivative and Hf(0001)/HfO_2 are analyzed. The MTE measurements are again performed at 300 K using the solenoid scan technique and the sub-picosecond laser-based UV radiation source tunable from 3.0-5.3 eV (235-410 nm) at UIC. The measured low MTE of the Hf(0001) photocathode is confirmed to be due to the low effective mass of the primary metal crystal emission band using the developed one-step photoemission simulation a result demonstrating that band dispersion can be exploited to attain low MTE values from solid-state photocathodes[25]. On the other hand, photoemission from the Hf (0001)/HfO_2 photocathode is shown to be dominated at low excess energies by emission from a populated 1*s*-like oxygen vacancy defect states in the native ~10 Å oxide layer and at higher excess energies by emission from the underlying metal a picture consistent with a presented modification of the one-step photoemission simulation that describes emission from defect states.

In chapter 7, I present the spectral characterization data obtained at Lawrence Berkley National Laboratory for a Cu (100) photocathode at temperatures of 300 K and 35 K. First, I will briefly describe the ultra-high vacuum (UHV) system used to obtain experimental data. This includes a ∼150 fs pulse-width and frequency-tripled Ti-Sapphire oscillator with a repetition rate of 76 MHz provided the 4.2-4.9 eV UV photon energies used for the presented measurements[27]. Since the oxidation rate of Cu photocathodes is high, Ar ion bombardment

and a few cycles of annealing at high temperature is used to obtain clean Cu(001) photocathode surfaces whose quality is checked using low energy electron diffraction (LEED) patterns and Auger electron spectroscopy. Again, I compare the experimental data at both temperatures to the predictions of the one-step photoemission model of chapter 2. In particular, I highlight the presented experimentally obtained record low MTE of 5 meV from the cryogenically cooled 35K (100) surface of copper using near-threshold photoemission.

Finally, in chapter 8, I summarize the experimental and theoretical results presented in this thesis that have provided a clear path for the future discovery of (ultra)low emittance solid-state photocathodes by *Ab initio* methods by developing explanations for the observed spectral electron emission characteristics. Suggestions for future areas of work are also included.

CHAPTER 2

PHOTOEMISSION THEORY

A new theoretical formulation of one-step photoemission[20] is presented in this chapter that is based on the exact quantum solution for transmission through (excess energy, $\Delta E < 0$) and over ($\Delta E > 0$) a triangular barrier evaluated by R. G. Forbes and J. H. B. Deane. The photoemission analysis, which enforces the transverse momentum conservation in electron emission, employs a bulk electron-like emission band of spherical symmetry with its effective mass m* (i.e., band dispersion) and Fermi energy ε_F as free parameters. It also includes the physical properties of both the emitting state and the vacuum; specifically, the local density of the emitting bulk band states and the recipient vacuum density of states. The effects of the electron effective mass, the Fermi energy of the band, the electron temperature, and the surface acceleration field on the photocathode's spectral emission properties will be examined. For application to the photocathode research presented in this thesis, the new photoemission analysis requires a fundamental knowledge of the electronic properties of the photocathode material such as band structure, work function, effective mass etc. In section 2.6, I describe the Ab initio density functional theory (DFT) calculations employed to provide these parameters using Rhodium as an example.

2.1 The photoelectric effect

In 1905, Albert Einstein correctly postulated that the light is made of little packets, at first called quanta and later called photons. The energy in each quantum of light was equal

to the angular frequency (ω) multiplied by the reduced Planck constant ($\hbar$) [28]. As a result, the photoelectric effect can be observed when a single electron is ejected by a photon above a certain threshold frequency. In 1921, Albert Einstein earned the Nobel prize for this quantum description of the photoelectric effect that may be formulated as

$$\Delta E = KE_{max} = \hbar\omega - \phi_{eff} \qquad 2.1$$

where, KE_{max} the maximum kinetic energy of a photo-emitted electron in the vacuum (and is known as the excess energy (ΔE)), which is independent of the incident light intensity, and the minimum energy required to photo-emit an electron from the surface is the effective work function ϕ_{eff} of the emitting material. In the three-dimensions, maximum kinetic energy is the summation of transverse electron kinetic energy (parallel to the photocathode surface) and longitudinal electron kinetic energy (normal to the photocathode surface);

$$KE_{max} = \frac{\vec{P}_{T0}^2}{2m_0} + \frac{\vec{P}_{Z0}^2}{2m_0} \qquad 2.2$$

where $\overrightarrow{P_{To}}$ and $\overrightarrow{P_{z0}}$ are the electron transverse and longitudinal electron momenta in the vacuum, respectively. When $\overrightarrow{P_{z0}} = 0$, the maximum possible transverse momentum for the photo-emitted electron is therefore given by

$$P_{T,max} = \sqrt{2m_0\Delta E}\,. \qquad 2.3$$

If such photo-emitted electrons are accelerated in, for example, a DC gun to an energy *E* associated with a non-relativistic momentum $p_z = (2m_0E)^{1/2}$, then the maximum divergence

angle of the accelerated electron beam is $p_{T,max}/p_z = \sqrt{\Delta E/E}$. Of course, as in optics, the quality of a beam is related to its divergence at a given spatial size. In accelerator and particle beam physics, the beam quality is usually expressed in terms of its normalized transverse emittance,

$$\epsilon_T = \frac{1}{m_0 c} \Delta x \Delta p_T \ . \qquad 2.4$$

Here Δx is the rms transverse beam size and Δp_T is the rms transverse momentum of the electron beam. This transverse emittance quantity is conserved in a non-aberrating (i.e. 'optically' perfect) propagation system. At the surface of the emitting photocathode, the rms transverse momentum is related to the mean transverse energy (MTE) of the photo-emitted electron distribution by the following equation:

$$MTE = \frac{m_0}{2} \langle V_x^2 + V_y^2 \rangle = \frac{\Delta p_T^2}{m_0} \ . \qquad 2.5$$

where V_x and V_y are velocity along x and y directions respectively. Consequently, a high-quality photo-electron beam is characterized by a low MTE (or low rms transverse momentum) that leads to a low emittance for a given beam size.

2.2 Theoretical explanations for photoemission

Despite the years, the photoelectric effect still continuously experiences new developments in experimental techniques and theoretical explanations to clarify the basic theory of electron emission from photocathodes. Dowell and Schmerge[18] used a three-step photoemission model to derive an equation relating the MTE to only the excess energy, $\Delta E = \hbar\omega - \phi_{eff}$; namely, $MTE = \Delta E/3$. In the three-step model photoemission proceeds as follows;

(i) after photon absorption the electrons are first excited into a higher energy state, (ii) the electrons transfer to the surface with or without scattering, and (iii) finally, the electrons escape into the vacuum[17]. The absorption of a photon in three-step model conserves energy but not momentum. In this theory, Dowell and Schmerge use an electron distribution at zero temperature, include electron-electron scattering, and assume that emission is from the volume of the photocathode. The resulting equation is in good general agreement with the measured MTE from many poly-crystalline photocathode materials, including copper[29].

Subsequently, Vecchione et al. modified the Spicer three-step photoemission model[17] by including the temperature-dependent Fermi-Dirac distribution to develop expressions for the MTE (equation 2.6) and quantum efficiency (QE) (equation 2.7). He employed the Sommerfeld model of a metal where, the electrons are bound by uniform potential and have kinetic energy measured with respect to it. The resulting density of states is constant so that the employed Fermi-Dirac statistics solely dictate the occupied density of states. This gives an exponentially decaying occupational probability to states above the work function ϕ. In the Spicer three-step photoemission model[17], electrons first absorb photons such that their momentum is increased normal to the surface only; in the second step, electrons diffuse to the surface where they escape in the third step based on their momentum[17]. The probabilities associated with steps one and two are assumed to be represented by a constant S_{12} such that $0 \leq S_{12} \leq 1$. The probability associated with step three is given by the charge emitted per unit time per unit area (assuming all electrons are ideally photoexcited) divided by the current density normally incident on the surface[19]. This results in in the following expressions for the MTE and QE as a function of the excess energy ΔE[19].

$$QE = S_{12}\left\{\frac{Li_2\left[-Exp\left(\frac{\Delta E}{k_B T_e}\right)\right]}{Li_2\left[-Exp\left(\frac{E_F}{k_B T_e}\right)\right]}\right\} \qquad 2.7$$

$$MTE = k_B T_e\left\{\frac{Li_3\left[-Exp\left(\frac{\Delta E}{k_B T_e}\right)\right]}{Li_2\left[-Exp\left(\frac{\Delta E}{k_B T_e}\right)\right]}\right\} \qquad 2.6$$

where Li_n is the ploy-logarithm function of order n. A consequence of the inclusion of the Fermi-Dirac distribution is that there is photoemission even when $\hbar\omega < \varphi$ due to the Boltzmann tail of the electron distribution. When $\hbar\omega - \varphi >> k_B T_e$, the QE equation reduces to the Fowler-Dubridge relation[30] [26] , $QE = A(\Delta E)^2$; namely, that the QE increases as the square of the excess photoemission energy.

In a real photoelectron gun, the photocathode surface is also subjected to the acceleration field of the gun the extraction field for the electrons which can also affect the emission properties of the photocathode. The first approximated theory for the extraction of electrons from cold metals by intense electric fields was developed by Schottky[31]. At higher temperatures, thermionic emission begins, and field emission becomes sensitive to temperature and finally blends into thermionic emission. For instance, Fowler and Nordheim (1928)[32] developed a theory to include the effect of an external field using the same methods and the same underlying picture of metals (Sommerfeld's) in Nordheim's "On the theory of thermal emission and the reflection of electrons on metals" paper [33].

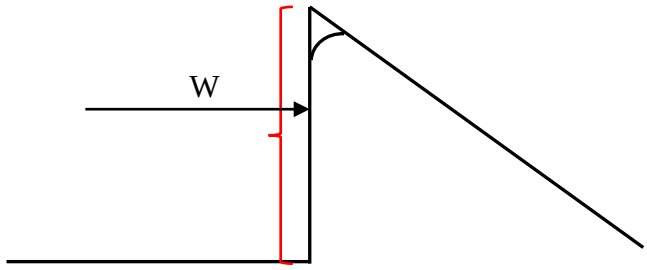

Figure 2.1: The exact triangular barrier created using an external electric field (F) and the top corner is rounded due to image charge effect.

The emission coefficients derived by Fowler and Nordheim are written below for W<C (equation 2.8) and W>C (equation 2.9), respectively. When W~C, both formulas cannot be used as D(W) depends mainly on the exact form of the potential energy curve.

$$D(W) = \frac{4\{W(C-W)\}^{\frac{1}{2}}}{C} e^{-4\pi(C-W)^{\frac{3}{2}}/3F}, \qquad 2.8$$

$$D(W) = \frac{4W^{\frac{1}{2}}(W-C)^{\frac{1}{2}}}{[W^{\frac{1}{2}}+(W-C)^{\frac{1}{2}}]^2+[F/(4\kappa\{W-C\})]^2}. \qquad 2.9$$

Later in 2011, Rokhlenko showed that the approximate Fowler-Nordheim formulae are invalid in strong fields[34]. This work was devoted only to the tunneling probability in the fields of arbitrary strength, and they described the field as a function decaying to zero from a starting point at infinity. A more straightforward theory using the Airy functions [35] Ai and Bi was developed by Gadzuk & Plummer (1973) [36] , which Jensen and Ganguly (1993)[37] also employed to initiate a third-generation treatment.

A single universal formula for the transmission coefficient (D^{ET}) of an exact triangular barrier for both tunneling and flyover was derived by R. G. Forbes and J. H. B. Deane

[38]. For simplicity, they chose a barrier slope downwards to the left (negative coordinate values) and an Airy function approach that uses a reflected barrier and puts the origin of coordinate system at the electron's turning point. This approach has a simpler mathematical formalism than the previous treatments and is readily evaluated by computational techniques.

2.3 The one-step photoemission model

For many photocathode materials, including all the single-crystal metals studied in this work, there are no electronic states into which the electrons can be photo-excited prior to emission into the vacuum. This means that the three-step photoemission models described above, which require a real band state for the transport or diffusion in the second step, are unphysical. The only alternative is the one-step photoemission mechanism proposed by Mahan[16] in which the electron is emitted into the vacuum via an excited virtual state that is a replica of the band state from which the electron originated. The electrons that then have a longitudinal component (z) of their energy greater than the work function can escape into the vacuum, and all other electrons reflect off the potential barrier back into the bulk material. In the UV photon regime, the photon has a negligible momentum[39] compared to electron momentum, $\hbar\omega/_{c} << P_{tot}$, which implies that the electron momentum is essentially unchanged during photon absorption inside the solid; that is, the energetically photo-excited electron maintains the momentum of its initial band state. In the plane of the emission, the transverse electron momentum is conserved, $\overrightarrow{P_T} = \overrightarrow{P_{T0}}$; where P_T and P_{T0} are transverse momentum in solid and outside respectively[10]. However, longitudinal momentum is not conserved due to energy conservation over the work function potential step.

2.4 New photoemission Formalism

The essential features of the one-step photoemission analysis predominantly employed in this thesis are schematically illustrated in Figure 2.2. The triangular barrier is associated with an applied surface acceleration field E_{acc} of the electron gun in the vacuum and the material-vacuum barrier is modeled as step potential; in other words, the details of the crystal potential and associated Schottky effect are not included.

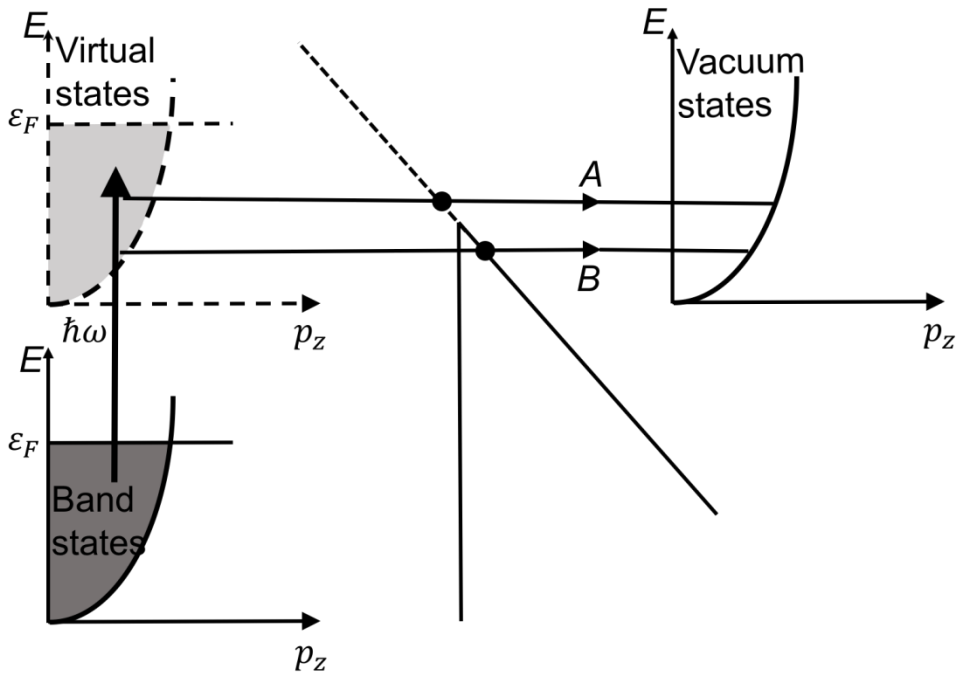

Figure 2.2: Schematic of the simulated one-step photoemission process: Photo-excitation of the bulk band states into a set of identical virtual band states from which electrons transmit (with transverse momentum conservation) into the vacuum states either above (photoemission with $\Delta E > 0$; path A) or below (photo-assisted tunneling with $\Delta E < 0$; path B) the triangular barrier generated by the applied acceleration field in an electron gun: $\mathcal{E}_F$ = Fermi energy.

The electrons from the bulk band states are photo-excited by the incident photon energy $\hbar\omega$ to the vacuum via 'virtual' electronic states, whose energy-momentum dispersion relation is, to a very good approximation, a replica (at the higher energy) of that of the bulk electronic band states[9]. These excited states, if occupied in the bulk, may emit electrons into the vacuum under the necessary energy-momentum conservation by either above barrier

photoemission ($\Delta E < 0$) or photo-assisted tunneling ($\Delta E > 0$); respectively, paths A and B in Figure 2.2 . The employed photoemission model enforces transverse momentum conservation parallel to the planar photocathode surface in the electron emission [10], uses the energy-momentum relationships of both the bulk and vacuum states, and includes their local density of states (LDS). Consequently, at each transverse momentum p_T associated with a bulk band energy E, the one-step photoemission simulation evaluates the product of the emitting bulk band LDS, their occupation (using a Fermi-Dirac population distribution), the transmission coefficient of the triangular barrier, and the local density of the available vacuum state into which the emitting electron is to be received. The inclusion of the latter implies that the 'joint density of states' between the initial occupied and final unoccupied states is evaluated explicitly as is required in any description of band-to-band transitions; for example, optical absorption in semiconductors [40].

For simplicity, in the following initial formulation of one-step photoemission I will assume that the emission is from a positive dispersion bulk electron band in the first Brillouin zone with an effective mass equal to the free electron mass m_0; that is, an energy-momentum relation of the form

$$E(\mathbf{p}) = \frac{p_z^2}{2m_z} + \frac{p_T^2}{2m_T}, \qquad 2.10$$

where p_z is the longitudinal electron momentum in the band. The LDS of such an isotropic band is proportional to $m_0^{3/2}\sqrt{E} = m_0\sqrt{(p_z^2 + p_T^2)/2}$, and the occupation of the band at any energy E is a function of both the Fermi energy $\mathcal{E}_F$ and the electron temperature T_e through the Fermi-Dirac distribution;

$$f(E) = \frac{1}{(1+exp[(E-\varepsilon_F)/k_B T_e])}\,, \qquad 2.11$$

where k_B is Boltzmann's constant. Equation 2.10 defines the longitudinal (kinetic) energy of the electron in the band as $K_z = E(\mathbf{p}) - \frac{p_T^2}{2m_T}$ which then allows the bulk band dispersion to be included in the transmission coefficient (derivation shown in the Appendix) of the triangular barrier for emitted electrons [38];

$$T = \frac{4Cp_z}{\left(2Cp_z + \pi C^2 p_z^2 \left(Ai^2(\xi) + Bi^2(\xi)\right) + \pi((Ai'(\xi))^2 + (Bi'(\xi))^2)\right)}\,, \qquad 2.12$$

where $C = (2m_0 \hbar e E_{acc})^{-1/3}$ with e the free electron charge and ħ Planck's constant divided by 2π, and Ai(ξ) and Bi(ξ) are Airy functions of the first and second kind, respectively, with the prime denoting the first derivative. The Airy function argument is given by

$$\xi = \sqrt[3]{\frac{2m_0}{(\hbar e E_{acc})^2}}(E_{th} - K_z)\,, \qquad 2.13$$

where the bulk band threshold energy for above barrier photoemission $E_{th} = \mathcal{E}_F - \Delta E$. Finally, the density of the recipient vacuum state for the emitted electron at the conserved value of the transverse momentum is proportional to $m_0\sqrt{p_{z0}^2 + p_T^2}$, where p_{z0} is the longitudinal momentum in the vacuum at emission. The exact analytical solution of Forbes and Deane [38] also allows for the evaluation of p_{z0}, the longitudinal momentum of the electron in the vacuum, for emission above and below the barrier;

$$p_{z0}(above) = \frac{1}{C}\left|\frac{Ai'(\xi) - iBi'(\xi)}{Ai(\xi) - iBi(\xi)}\right| \qquad 2.14$$

and

$$p_{z0}(below) = \frac{1}{C}\left|\frac{Ai'(0) - iBi'(0)}{Ai(0) - iBi(0)}\right|. \qquad 2.15$$

I note here that equation 2.12 is entirely consistent with the expectation that the maximum value of p_{z0} is equal to $\sqrt{2m_0(\hbar\omega - \phi)}$ when $T_e \to 0$. Further, equation 2.15 indicates that p_{z0} below the barrier is small but not equal to zero unless $E_{acc} = 0$, in which case below barrier transmission ceases.

The one-step photoemission simulation I present in this Thesis uses the above to evaluate the relative number of electrons emitted at each value of the transverse momentum by summing over all energy states contributing to emission at that value of p_T. The MTE is then obtained by taking the normalized second order moment of the evaluated transverse momentum distribution of the emitted electrons in the vacuum, $TE = \langle p_T^2 \rangle / m_0$, and the QE (in arbitrary units) is calculated by simply integrating over the distribution.

In Figure 2.3, as a comparative example, I present the result of evaluating both the MTE and QE as a function of excess energy ΔE for a Ag(100) photocathode; for which the work function ϕ = 4.36eV [41], the effective mass m^* of the emitting electrons near the Fermi level in the bulk band is (to a good approximation) equal to m_0 [40], and the Fermi energy $\mathcal{E}_F$ = 5.49eV. Room temperature operation (T_e = 300K) is assumed and I employ a surface acceleration field of 1MV/m typical of a DC electron gun for the simulation. The evaluation of the MTE using the one-step photoemission simulation (black solid line) is compared in Figure 2.3(a) with the results of two prior analyses; the formulation of Dowell and

Schmerge[18] for which MTE = $\Delta E/3$ (dashed red line), and the more recent expressions (equation 2.6) derived by Vecchione et al. [19] (red solid line).

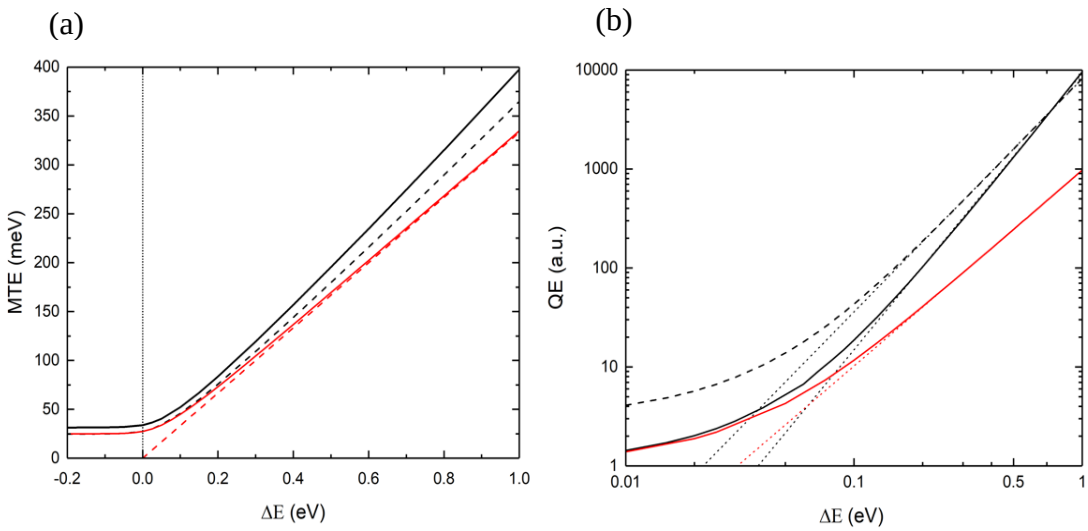

Figure 2.3: Emission properties of a Ag(100) photocathode at 300K (ϕ = 4.36eV, bulk electron mass = m_0, $\mathcal{E}_F$ =5.49eV, and $E_{acc.}$ = 1MV/m): (a) MTE as a function of the excess photoemission energy ΔE; full one-step simulation (black line), one-step simulation without the vacuum states (black dashed line), equation 2.6 (red line) [19], and $\Delta E/3$ (red dashed line)[18]. (b) QE as a function of ΔE; full one-step simulation (black line), one-step simulation without the vacuum states (black dashed line), and equation 2.7 (red line) [19],with corresponding power law fits for ΔE > 0.25eV shown as thin dotted lines.

It is clear that the formulation derived by Vecchione et al.[19], which asymptotically tends to the result of Dowell and Schmerge[18] at high excess energies, underestimates the MTE at all ΔE since it does not include either the bulk band or vacuum states. The expression of equation 2.6 does however agree with the one-step model below the photoemission threshold (ΔE < 0) when the vacuum density of states are omitted in the simulation (black dashed line) both giving a limiting value $k_B T_e \approx$ 25meV for the MTE. This is because the electrons emitting from the population in the thermal Boltzmann tail that extends above the photoemission barrier have a sufficiently small energy spread ~$k_B T_e$ to ensure that they originate from a relatively constant density of states in the bulk band - the approximation employed in obtaining equation 2.6. Consequently, the increase in the MTE to 31.5(±0.5)meV when ΔE < 0 evaluated with the full one-step simulation is entirely due to the increase with

higher electron momenta of the recipient vacuum density of states. As ΔE increases above threshold, both one-step simulations with and without the vacuum states return higher values of the MTE than that predicted by the prior analyses of Dowell[18] and Vecchione[19] due to the inclusion of the bulk band states. For excess energies greater than 0.1eV, the full one-step photoemission model predicts MTE values 15-20% greater than obtained from equation 2.6 for the simulated Ag(100) photocathode. I note that photo-assisted tunneling (below barrier emission) is negligible in this example, contributing less than 1% of the emitted electrons even at $\Delta E = -0.2$eV for the employed 1MV/m acceleration field, and so does not contribute significantly to the presented MTE results.

The simulated spectral dependence of the QE for the Ag(100) photocathode example is shown in Figure 2.3(b) (black line) together with the QE dependence predicted by Vecchione et al. [19] (red line). For the purpose of comparison, both the simulated one-step photoemission data and the dependence described by equation 2.7 are normalized to unity at $\Delta E = 0$. Both the one-step model and equation 2.7 display the expected rapid increase of the QE with ΔE associated with the strongly increasing number of filled bulk band states that can emit electrons into the vacuum as the excess energy increases. However, the log-log plot of Figure 2.3(b) clearly indicates that the one-step simulation predicts a different power law dependence for the QE on ΔE than equation 2.7 for excess energies greater than 0.25eV = $10k_BT_e$. A fit (dotted line) to the one-step simulation for this Ag(100) example indicates that QE = $A(\Delta E)^{2.85}$, where A is a constant, whereas equation 2.7 returns the Fowler-DuBridge relation of a quadratic power law dependence (red dotted line); i.e., QE = $A(\Delta E)^2$ [30] [26]. The difference in these power law dependences is directly related to the inclusion of the bulk band and vacuum states in my one-step simulation, both of which are omitted in the prior analyses [18,19,26,30] . Indeed, removal of the vacuum density of states from the one-step

analysis generates the data set shown by the black dashed line in Figure 2.3(b) for which the dependence on excess energy is of the form QE = $A(\Delta E)^{2.4}$ for $\Delta E > 10k_BT_e$ (dotted line) – a power law dependence between that of equation 2.7 and the full one-step photoemission simulation. This latter data set is normalized by the QE with the vacuum states included at $\Delta E = 0$ to illustrate the roughly factor of three reduction in the QE at low excess energies that is caused by the density of vacuum states at low emitted electron momenta. Further, both my presented photoemission simulation and the analysis of Vecchione et al. [19] clearly show the influence of the 300K Boltzmann tail on the QE at excess energies below 0.25eV, which also provides for a finite QE when $\Delta E < 0$.

Although incorporating a more realistic triangular barrier solution [16] and the physical properties of both the bulk and vacuum states, this one-step model of photoemission does not include a number of factors that can affect photocathode performance. First and foremost, the photoemission simulations do not include the matrix element describing the optical excitation of the electrons into the emitting 'virtual' states. This of course important for an *Ab initio* determination of the QE [42], but it is unlikely to affect the MTE evaluations from the simulated electron emission distributions unless the matrix element has a significant variation in momentum space for the excited virtual state. Second, the employed exact triangular barrier solution of Forbes and Deane [38] does not allow for the inclusion of the Schottky effect [12,18,43] in a formal manner. However, other than the lowering of the work function, the Schottky effect is not expected to alter significantly the presented simulation results, except perhaps at the highest acceleration fields where the exact shape of the potential barrier becomes important for electrons emitted by photo-assisted tunneling. Third, for the sake of brevity, the optical properties of the photocathode material, specifically the surface reflectivity and absorption coefficient for the incident light, are not included in the analysis but

they could be incorporated for each individual photocathode material. The spectral properties of both will of course affect the photocathode QE by determining the total number density of excited electronic states per incident photon, but not the MTE as this is a self-normalized parameter. Fourth, the effects of chemical and surface roughness, which have been treated elsewhere [13,26,44–46], are omitted; that is, the photocathode surface is assumed to be flat and at a uniform potential. Fifth, as the presented one-step photoemission formalism assumes transverse momentum conservation in electron emission [10], the scattering of the excited virtual state electrons by phonons [47] during or just before emission into the vacuum is also not included. The strength of electron-phonon scattering is strongly material dependent and can be expected to result in an increased MTE and likely a reduced QE. Finally, and for the same reason, carrier-carrier scattering [18,48] (e.g., inelastic electron-electron scattering) is not included in the analysis.

2.5 Simulation results

In the following sub-sections, I discuss the effect that the electron temperature, Fermi energy, and the surface acceleration field are expected to have, within one-step photoemission, on the spectral dependence of both the MTE and QE from planar photocathodes. The presented simulation results employ the Ag(100) exemplar of Figure 2.3 as a template, changing a single parameter at a time to illustrate its effect on the photocathode's electron emission properties. As the QE is not explicitly evaluated from first principles, all the QE data is normalized to that at $\Delta E = 0$ for the Ag(100) photocathode in a DC gun ($\phi = 4.36$eV, band electron effective mass $m^* = m_0$, $\mathcal{E}_F = 5.49$eV, $T_e = 300$K, and a surface acceleration field $E_{acc.} = 1$MV/m).

2.5.1 Electron temperature

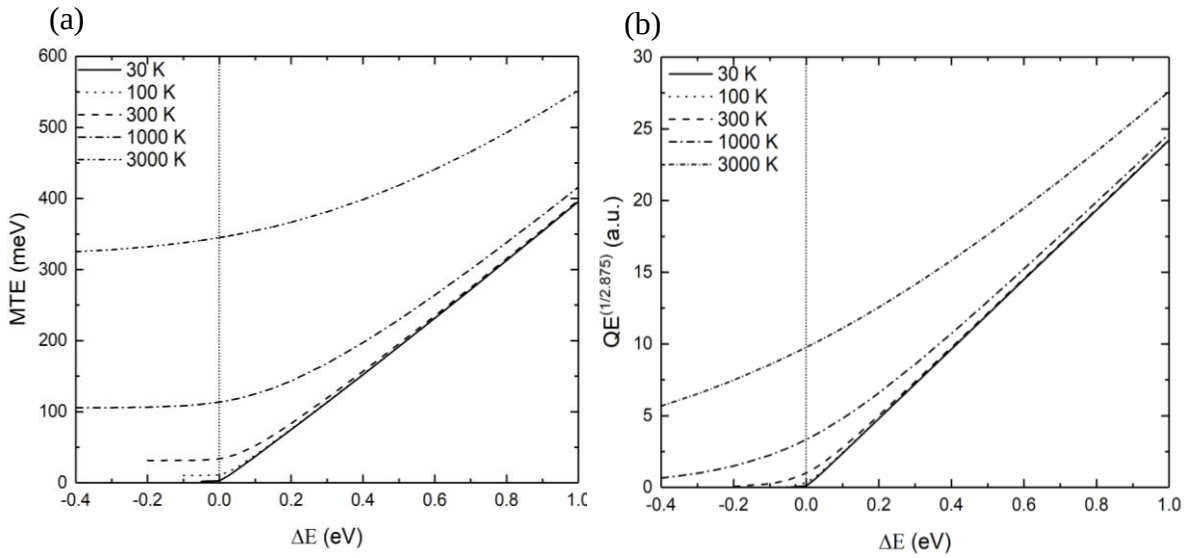

Figure 2.4: Emission characteristics of a Ag(100) photocathode (ϕ = 4.36eV, bulk electron mass = m_0, $\mathcal{E}_F$ =5.49eV, and $E_{acc.}$ = 1MV/m) for electron temperatures T_e of 30, 100, 300, 1000, and 3000K: (a) MTE and (b) $QE^{1/2.875}$ as a function of excess photoemission energy.

The effect of changing the photocathode temperature, or more specifically the temperature T_e of the electron distribution in the simulated isotropic Ag(100) band, is shown in Figure 2.4. As expected, the MTE below the work function ($\Delta E < 0$) is strongly temperature dependent due to over barrier emission from the Boltzmann tail of the electron distribution (Figure 2.4(a)). In this region just below photoemission threshold, the minimum value of the MTE is again ~25% greater than $k_B T_e$, primarily due to the influence of the vacuum density of states. At larger negative excess energies, photo-assisted tunneling starts to dominate the over barrier emission from the thermal tail of the electron distribution and the MTE decreases due to the strong reduction in tunneling probability with transverse momentum p_T – an effect not visible in Figure 2.4(a). At high positive excess energies, when $\Delta E >> k_B T_e$, the spectral dependence of the MTE tends to the low temperature value since the effect of the Boltzmann tail population is diminished with respect to the rest of the occupied emitting states. The low temperature linear dependence of the MTE on the excess photoemission energy is of the form

$\Delta E/2.53$, which is to be compared with $\Delta E/3$ from the prior analyses [18,19] that do not include the combined effects of the bulk and vacuum states.

For electron temperatures T_e < 100K, the presented one-step photoemission simulation predicts that MTE values less than 10meV should be attainable at low or negative excess energies for photocathode materials with similar parabolic band structures and $m^* \approx m_0$; for example, appropriately oriented single-crystals of Cu, Au, and the alkali group metals [49]. We also note that a recent study of cryo-cooled Cs_3Sb photocathodes illuminated at 690nm reported a reduction of the MTE from ~43meV at 300K to ~12meV at 90K [50]. As in this case electron emission is expected to be from the Boltzmann tail of the electron distribution photoexcited into the conduction band states, the fact that both measured MTE values are greater than their corresponding thermal values of 25 and 8meV is consistent with the predicted influence of the vacuum density of states on the MTE of electron emission. For Cs_3Sb, an additional factor is likely be the effective mass m^* and dispersion of the emitting conduction band state.

The spectral dependence of the QE at different electron temperatures T_e (Figure 2.4(b)) also illustrates the strong influence of bulk band population in the Boltzmann tail at low and negative excess photoemission energies. Here we have plotted the normalized QE to the 0.348 (= 1/2.875) power against ΔE as this power law dependence is the best fit to the simulation data at the lowest 30K temperature where the Boltzmann tail population has the smallest effect. As T_e increases much beyond 300K, where $QE^{1/2.85}$ also provides the best linear dependence with ΔE (Figure 2.4(b)), it is clear that a simple power law of the form $QE = A(\Delta E)^n$ is no longer a valid expression for excess energies below 1eV. Nonetheless, for T_e around room temperature and below, a plot of $QE^{1/n}$ against ΔE should allow for the extraction of the

photocathode work function with reasonable accuracy [51], provided that the linear fit employs measurements taken for $\Delta E > 10k_BT_e$. As I will show below, such a power law scaling for the QE only exists if the band Fermi energy ε_F is much greater than the excess photoemission energy ΔE.

2.5.2 Fermi energy

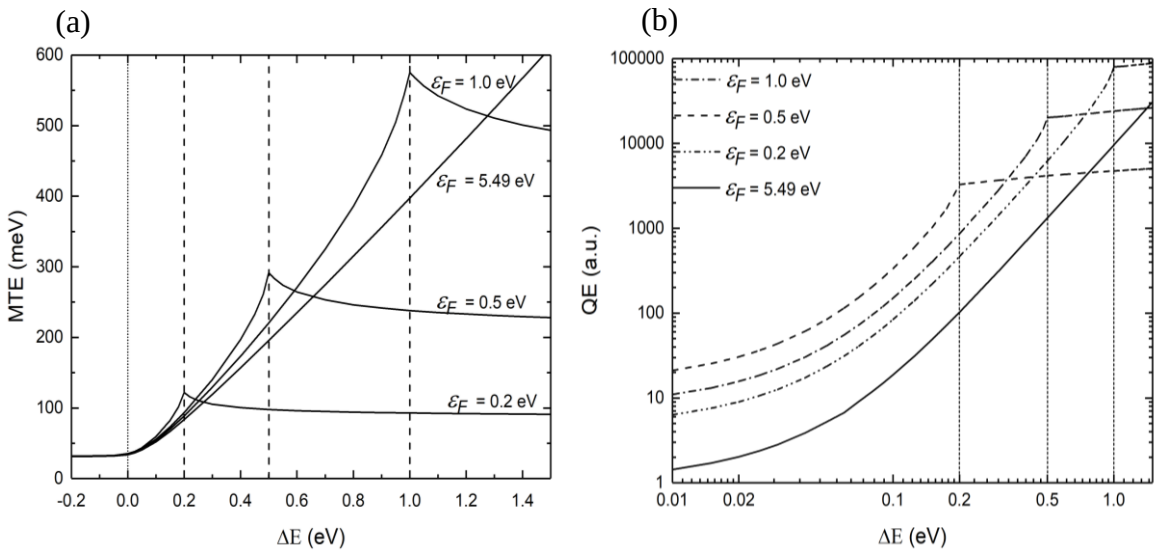

Figure 2.5: Simulated dependence of (a) the MTE and (b) the QE on the excess photoemission energy for Fermi energies of 0.2, 0.5, and 1.0eV (ϕ = 4.36eV, bulk electron mass = m_0, T_e = 300K, and $E_{acc.}$ = 1MV/m. The vertical dashed lines indicate were $\Delta E = \mathcal{E}_F$ for the three cases and the dot-dashed line are the results for the Ag(100) photocathode ($\mathcal{E}_F$ = 5.49eV) .

As the Fermi energy defines the energy of the last electron in the bulk band as $T_e \rightarrow 0$, the emission properties of a solid-state photocathode are expected to be affected when ΔE is of the order of or greater than $\mathcal{E}_F$. The results of a one-step photoemission simulation for Fermi energy values of 0.2, 0.5 and 1eV, depicted in Figure 2.5, show that this is indeed the case. In all cases, the dependence of the MTE on ΔE (Figure 2.5(a)) is similar to that in Fig. 2.3(a) for $\mathcal{E}_F$ = 5.49eV at low excess energies but displays a distinct 'cusp' when $\Delta E = \mathcal{E}_F$ (vertical dashed lines). At this critical value of the excess energy, all the excited bulk band

electronic states with positive p_z (in the direction of emission) are 'resonantly' matched in momentum and energy to the vacuum states leading to an increased transmission through the barrier at all p_T and hence a larger MTE. As ΔE increases beyond $\mathcal{E}_F$, the MTE levels off to a slightly lower and relatively constant value as the barrier transmission for the electrons excited from the bulk band moves off the $\Delta E = \mathcal{E}_F$ resonance and becomes less dependent on ΔE. This interpretation is supported by the spectral dependence of the QE displayed in Fig. 2.5(b) which shows a clear trend discontinuity at $\Delta E = \mathcal{E}_F$, just when all the band states with positive p_z can emit. At higher ΔE, the barrier transmission does increase [38], but no new states are available leading to a slower increase in QE with ΔE.

Also evident from the log-log plot in Fig. 2.5(b) is that the QE no longer follows a simple power law dependence with excess energy, QE = $A(\Delta E)^n$ for $\Delta E > 10k_BT_e$, when one-step photoemission is from a bulk band with a low Fermi energy. This must be the case since significant changes in the number density of available photo-emitting states occur as ΔE increases for excess energies less than, but of the order of, the Fermi energy. As a result, extraction of a value for the work function using measured QE data may prove difficult without a functional photoemission model in cases where $\mathcal{E}_F$ is in the range of $10 - 100k_BT_e$. In addition, I note that the one-step photoemission QE from the bulk band near threshold increases as the Fermi energy decreases – all the QE data being normalized to that at $\Delta E = 0$ for $\mathcal{E}_F = 5.49$eV and $T_e = 300$K (Fig. 2.3(b)). This is a direct result of increased barrier transmission when the longitudinal momentum p_z of an excited emitting state is closer to the momentum of the emitted electron p_{z0} from that bulk state.

2.5.3 Surface acceleration field

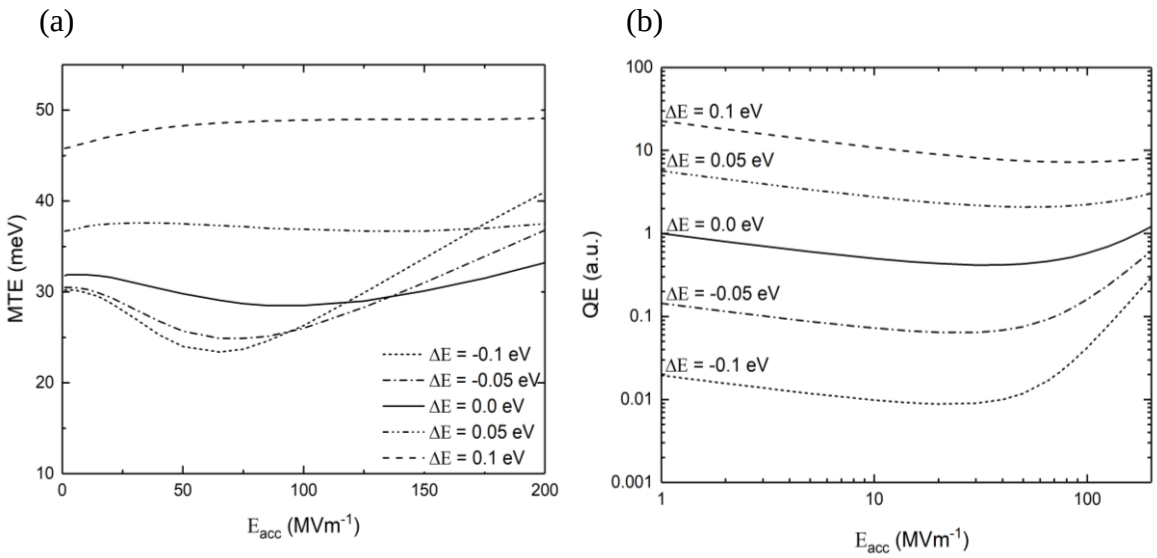

Figure 2.6: Simulated emission properties of a Ag(100) photocathode (ϕ = 4.36eV, bulk electron mass = m_0, =5.49eV, and T_e = 300K) as a function of applied surface acceleration field for near threshold excess photoemission energies of –0.1, –0.05, 0. 0.05, and 0.1eV: (a) MTE and (b) normalized QE.

Although the Schottky effect is not included in the one-step photoemission simulation, it is nonetheless informative to examine the predicted effect of the surface acceleration field E_{acc} on both the MTE and QE within the exact triangular barrier solution [38]. Figure 2.6(a) shows the dependence of the MTE on the acceleration field for selected near threshold excess photoemission energies of –0.1, –0.05, 0. 0.05, and 0.1eV. At positive values of ΔE, the MTE is fairly independent of E_{acc} as above barrier photoemission dominates. Closer to photoemission threshold there are more significant effects. Most notably, the MTE is reduced for $\Delta E < 0$ as the applied field is increased, reaching a minimum value below the $k_B T_e$ = 25meV thermal energy for surface fields between 40 and 80MV/m when $\Delta E < -0.05$eV. This lower than expected MTE value is caused by the increased contribution at higher E_{acc} of photo-assisted tunneling to the transverse momentum distribution of the emitted electrons.

This contribution has a MTE lower than 25meV for fields less than about 80MV/m due to the rapid drop in barrier tunneling transmission probability as p_T increases for an electron at a given bulk band energy. At higher fields, the triangular barrier becomes sufficiently narrow to increase the tunneling transmission probability at larger p_T so that the MTE again increases somewhat for $\Delta E < 0$. As a result, a minimum in the MTE develops below the photoemission threshold – an effect that may not be observable experimentally since the Schottky effect is not included in this photoemission simulation.

The effect of E_{acc} on the QE follows expected trends and is displayed in Fig. 2.6(b) for the same selected near threshold excess photoemission energies of –0.1, –0.05, 0. 0.05, and 0.1eV. At low surface field strengths, where above barrier photoemission dominates, the QE slowly decreases with increasing E_{acc} due to the initial $E_{acc}^{-1/3}$ dependence of the transmission coefficient for the triangular barrier (equation 2.12). At field strengths greater than 20MV/m, the contribution from photo-assisted tunneling increases and this eventually reverses the initial trend the point of reversal being at lower values of E_{acc} for lower values of ΔE since the QE of above barrier photoemission (due to the photo-excited Boltzmann tail of the electron distribution) falls rapidly with decreasing ΔE below the photoemission threshold. Aside from the increased tunneling probability at higher acceleration fields, I note that a higher density of recipient vacuum states is also available at larger E_{acc} since equation 2.14 states that the longitudinal momentum of the electron emerging into the vacuum from the barrier increases with the cubic root of E_{acc}.

2.5.4 Effective mass

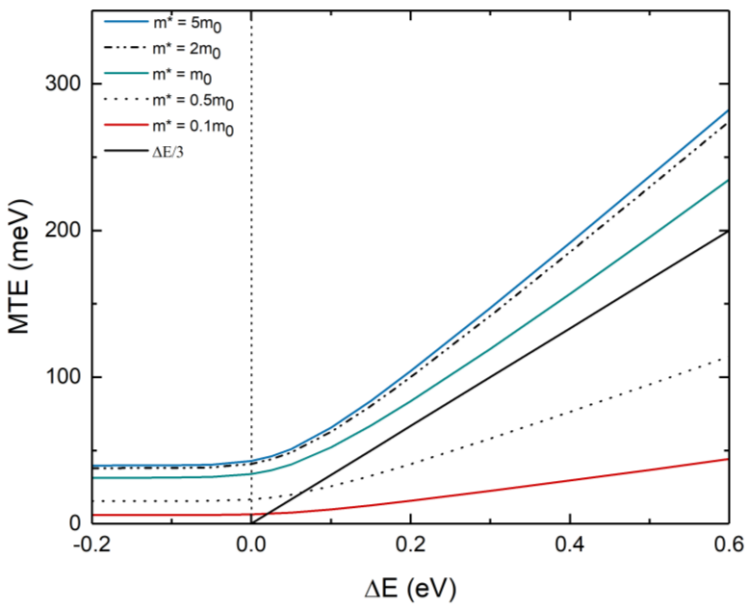

Figure 2.7: Simulated dependence of the MTE on the excess photoemission energy for different effective masses; $m^* = 5m_T, 2m_T, m_T, 0.5m_T, 0.1m_T$ together with MTE = ΔE/3 [18] .

Even though there several theories have been developed to explain photoemission from photocathodes, none of them include the effect that the effective mass of the emitting band state has on the emittance. In the original Forbes and Deane paper[38], an effective mass equal to the vacuum free electron mass m_0 is assumed inside the emitter. For the above barrier case, they extend the triangular barrier to the left (Figure 2.2) and pick the origin as the electron's classical turning point inside the emitter[38]. At this point, the electron has not been emitted into the vacuum as the classical turning point is to the left of the photocathode-vacuum boundary. Consequently, in order to include a longitudinal effective mass m_z for the emitting bulk band, two boundaries and transmission coefficients are employed for electron emission. The first, at the internal classical turning point, employs m_z on both sides; and the second at the photocathode-vacuum interface includes the electron mass change from m_z to m_0 in the

vacuum (Derivation in the Appendix A). These new boundary conditions affect the quantum efficiency more than the MTE but allow for the simulation of parabolic emission bands that are cylindrically symmetric about the emission direction with a longitudinal and transverse effective mass of m_z and m_T.

Figure 2.7 shows the spectral dependence of the MTE on the effective mass for different isotropic band effective masses; $m^* = m_z = m_T = 5\mathrm{m}_0, 2\mathrm{m}_0, \mathrm{m}_0, 0.5\mathrm{m}_0, 0.1\mathrm{m}_0$. Again, all other parameters for the simulation of emission from the 'canonical' Ag (100) photocathode are held constant (ϕ = 4.36eV, band electron effective mass $m^* = m_0$, $\mathcal{E}_F$ =5.49eV, T_e = 300K, and a surface acceleration field $E_{acc.}$ = 1MV/m). It is clear that at all excess energies a larger effective band mass results in an increased MTE. For $m^* > m_0$, the MTE appears to reach a limiting value of ~40% above the $\Delta E/3$ Dowell Schmerge relation[18] for excess energies greater than ~$10k_BT_e$ which is associated with the dispersion of the emitting band states becoming negligible compared to that of the vacuum states ($m^* = m_0$). More interesting is the prediction that the MTE even at 300K can drop well below 25meV just above the photoemission threshold if m^* is significantly less than about $0.2m_0$. This is caused by the absence of available emission states at large p_T for highly dispersive bulk band states[27].

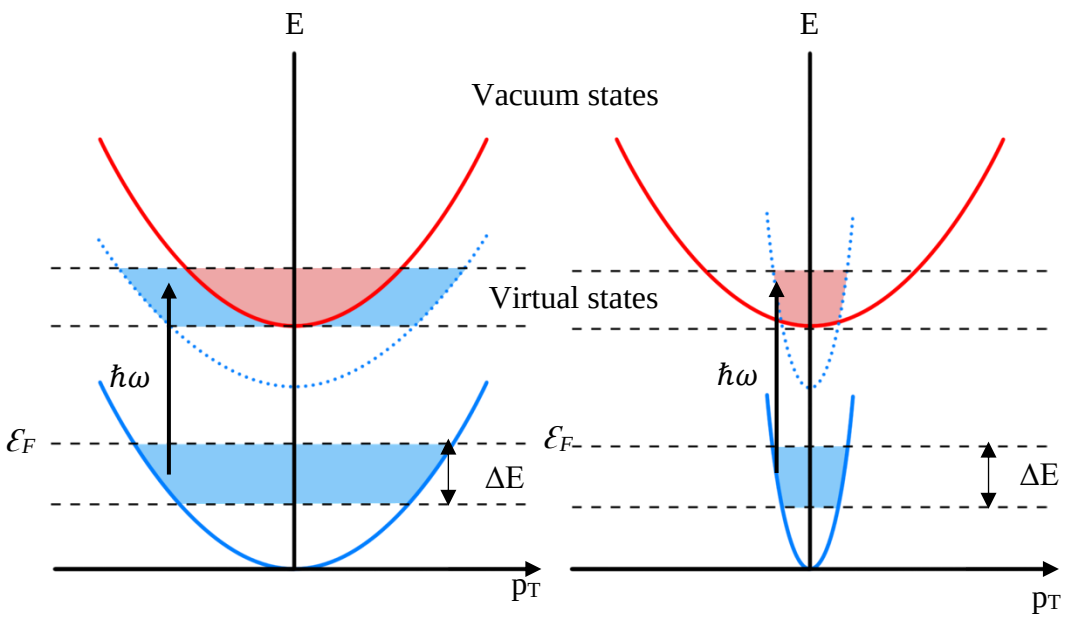

Figure 2.8: Energy vs transverse momentum diagrams illustrating the effect of the effective mass on MTE: Left panel shows a band with dispersion corresponding to free electron mass m_0 resulting in Dowell like behavior[9]; right panel shows a band with a low effective mass. Solid blue lines represent the actual metallic like parabolic ε(k) dispersion relations, where the blue highlighted area indicates states with sufficient excess energy for photoemission. The dotted blue line represents the virtual excited states, and the red highlighted area depicts the final allowed photo-emitting electron states[103].

Figure 2.8 illustrates how band dispersion, particularly in the transverse direction, can restrict the emission of electrons with high p_T values, thus reducing the MTE of electron emission. The left panel represents the one-step photoemission process from bulk band states with a dispersion determined by the rest electron mass m_0 and the right panel to one from states with a small effective mass m^*. In both panels, the shaded blue region indicates the states excited into the virtual states that have sufficient energy to be emitted, but only the shaded red area states can emit electrons into the vacuum states due to the transverse momentum conservation. Although, the density of states at zero transverse momentum is significantly larger for a higher effective mass band, with transverse momentum conservation in photoemission it is clear that a small effective mass for the emitting states can serve to restrict

the transverse momentum, and hence the MTE, of the photo-emitted electrons (right panel). In contrast, the transverse momentum for an electron emitted from a perfect metal photocathode with a free electron mass dispersion is only restricted by the vacuum state dispersion (left panel), resulting in MTE variation in approximate accordance with the Dowell model[18,52].

2.6 Density functional theory

To connect the above one-step photoemission formalism to real materials knowledge of their electronic band structure is required; specifically, the dispersion properties of the band states in the vicinity of the Fermi level that can photo-emit electrons in the crystal direction perpendicular to the photocathode surface. In this work, I employ density functional theory (DFT) based electronic structure property calculations to obtain the band structure of the studied single-crystal metal photocathodes. DFT-based *Ab initio* calculations have become a very common method, and their application has now spread among researchers in condensed matter theory and quantum chemistry, involving a vast community of end-users with very diverse scientific backgrounds and research interests[53]. There are different DFT-based computer codes such as VASP[54], Quantum espresso[53], ABINIT[55], CASTEP[56], and etc. to calculate electronic structure and model materials. Self-consistency in these calculations is achieved using an iteration-based approach in PWscf, employing at each step iterative diagonalization techniques, in the framework of the plane-wave pseudopotential method[53]. It is possible to use LDA (local density approximation) and GGA (generalized gradient approximation) pseudopotentials to include spin-orbit interactions with relativistic effects. The sampling of the Brillouin zone can be done using a Monkhorst-Pack[57] set of special k-points to deal with the discontinuity in k-space between occupied and unoccupied states.

2.6.1 Band structure and effective mass

The convergence tests are performed to achieve the minimum total energy configuration before calculating the real electric properties. For crystal structures, it is advantageous to obtain first the optimal lattice structure and constant to achieve a balance between computational cost and calculation accuracy. In this work, convergence tests were performed for the kinetic energy cut-off for the employed wave functions, the kinetic energy, the charge density for the potential, and the uniform grid of k-points to ensure that the ground state energy is within the energy convergence tolerance of 0.1 meV [58] using the experimental lattice constant as the initial input.

For the band structure calculation, the generated crystal structure was first viewed using Xcrysden software[59] to obtain the desired k-point path. Then a self-consistency calculation (SCF)[60] was performed, using obtained optimized input values, to determine the self-consistent density and potential. Next, the desired k-point path and number of bands is used in a non-SCF calculation to evaluate each chosen k-point's eigenvalues and eigen-vectors[61]. Finally, the GNUplot [62] used to plot band structure and Fermi surface along the high symmetry points and the lines in the first Brillouin zone.

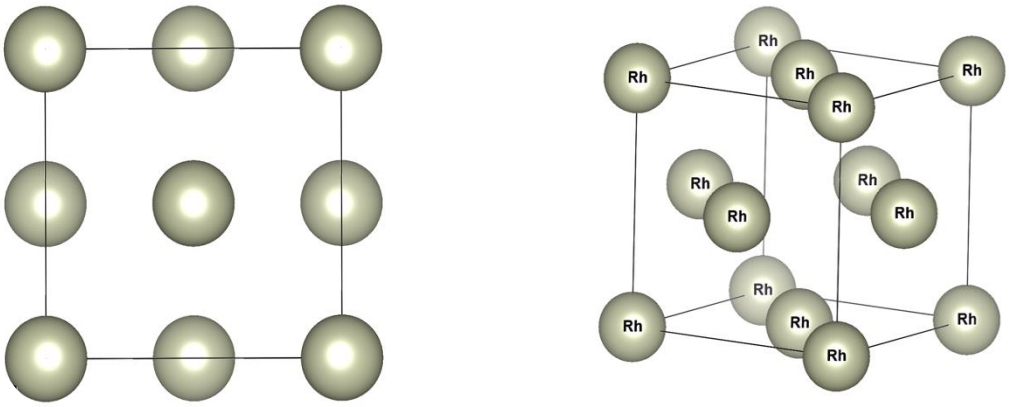

Figure 2.9: Rh crystal structure; FCC structure with optimized lattice constant a = 3.855Å. Right panel is the top view and left panel is the 45^0 rotated view. The unit cell contains 4 atoms. (1/8*8 for corners and 1/2 * 6 for faces)

For example, the DFT calculations for the bulk Rh crystal (one of the studied photocathode materials), include full relativistic effects, with spin-orbit coupling included during the plane wave self-consistency iterations. That is to say, a fully relativistic pseudopotential within the generalized gradient approximation (GGA)[63] was employed, and the electronic wave function is described by a plane-wave basis set with an energy cut-off of 40Ry, the energy cut-off for the charge density is set to 350Ry, a threshold of 10^{-6}Ry for the ground state energy is used, and a Marzari-Vanderbilt smearing[64] with a broadening of 0.01Ry is employed. The resulting DFT calculated face-centered cubic crystal structure for Rh has a lattice constant a = 3.855Å, which is within 2% of the experimental value[65]. The crystal structure obtained using the optimized lattice constant is shown in figure 2.9. The Rh band structure (figure 2.10) is calculated along the k-path $\Gamma \xrightarrow{\Delta} X \xrightarrow{Z} W \xrightarrow{Q} L \xrightarrow{\wedge} \Gamma \xrightarrow{\Sigma} K$ in the first Brillouin zone, where Δ, Z, Q, Λ, and Σ are symmetry lines with the lengths, $\overline{\Gamma X} = 2\pi/a$, $\overline{XW} = \pi/a$, $\overline{WL} = \sqrt{2}\pi/a$, $\overline{L\Gamma} = \sqrt{3}\pi/a$, and $\overline{\Gamma K} = 3\pi/\sqrt{2}a$ respectively. The effective mass at the Fermi level along any longitudinal emission direction is calculated using the curvature

of the relevant band; $m_z^* = \hbar^2\left(d^2E/dk^2\,|_{k=k_F}\right)^{-1}$, where k_F is the Fermi wave vector in the emission direction. The band structure along transverse direction at $k = k_F$ is fit to a parabola to evaluate the transverse effective mass m_T^*.

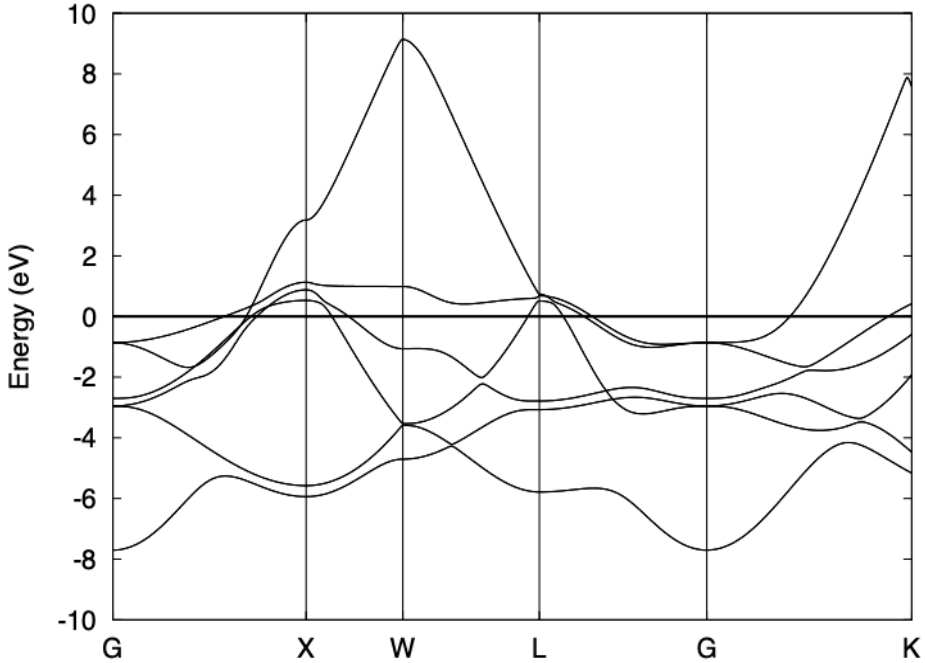

Figure 2.10: Rh band structure along high symmetry points. The horizontal line at 0 eV represents the Fermi level. Γ→X (001), Γ→K (110), Γ→L (111) represent directions.

2.6.2 <u>Work function</u>

The minimum energy required to extract an electron from the metal surface as known as work function;

$$\phi = E_{vac} - \varepsilon_F \qquad 2.16$$

where E_{vac} is the vacuum energy level, defined as the electrostatic potential outside the surface, and ε_F is the Fermi energy in the metal. The thin-slab technique used to calculate work function using the energy difference between vacuum level energy and Fermi energy (2.16 equation) [66–68]. For these DFT-based calculations, a thin slab layer along the desired (ijk) crystal direction was designed using the Xcrysden software with vacuum length at both ends of the thin slab chosen to obtain a flat average vacuum potential. The Fermi level for the thin slab is evaluated using a SCF calculation. A relaxation calculation[69] is necessary to obtain equilibrium atomic positions for the terminated surface since they may be different from the atomic positions for the bulk crystal[70]. The average macroscopic potential is calculated using Quantum espresso's input file "average.x" to obtain a vacuum level. Finally, equation 2.16 used to calculate the work function. The same procedure was repeated for different numbers of atomic layers to obtain a convergent value with an error less than 0.05 eV.

For a clean Rh(110) photocathode surface, for example, the evaluation of the work function using the thin-slab technique[11] [58] [68] uses a 0.02Ry Gaussian spreading for the (110) crystal surface and fully relativistic pseudopotentials[63]. To ensure sufficient accuracy in the calculation, a vacuum thickness of 20Å is used and the (1×1) supercell thickness (*n*) is increased from 6 to 10 atomic layers together with the $n \times n \times 1$ Monkhurst-Pack points[57] so that the work function value converges to within ±0.05eV. The value of $\phi_{Rh(110)}$ = 4.70(±0.05)eV extracted from this calculation is within the range of the accepted value of 4.86(±0.21)eV for Rh(110)[41].

CHAPTER 3

EXPERIMENTAL DESIGN

In this chapter, I will describe the experimental system at the University of Illinois at Chicago (UIC) that I employed to determine the spectral dependence of the mean transverse energy and quantum efficiency of photoemission from single-crystal metal photocathodes at 300K using a home-built sub-picosecond laser-based UV radiation source tunable from 3.0-5.3eV (235-410nm). The tunable UV radiation is generated by sum-frequency mixing the second and third harmonics of a front-end, 2W, 28MHz repetition rate, femtosecond Ytterbium-doped potassium gadolinium tungstate (Yb:KGW) laser with the signal and idler radiation from nonlinear-fiber continuum-seeded optical parametric amplifier (OPA). The planar metal photocathodes are illuminated by this laser-based tunable UV radiation source and a solenoid scan technique is used to determine the MTE by fitting the measured photo-electron beam spot size on a Ce: GAGG scintillator screen (1:1 imaged onto a CCD camera) as a function of the focal strength of two counter-wound cylindrical (solenoid) magnetic lenses with an extended analytical Gaussian (AG) model simulation of the electron pulse propagation. For the photoemission QE measurements as a function of photon energy, the scintillation screen is replaced by a 5 mm diameter aperture Faraday Cup connected to a pA meter. In this chapter, I will first discuss the tunable UV laser system design and then the photocathode characterization system along with a description of the AG model. The experimental system used to characterize Cu photocathodes at Lawrence Berkeley National Laboratory (LBNL) will be described in chapter 7 together with the results obtained for these photocathodes.

3.1 Tunable Laser System

3.1.1 The Yb:KGW laser head

In general, solid-state laser host materials must have excellent optical, mechanical, and thermal properties to withstand the severe operating conditions of practical lasers. Hardness, chemical inertness, absence of internal strain and refractive index variation, resistance to radiation-induced color centers, and ease of fabrication are desirable properties[71]. In addition, for the generation of short (sub-picosecond) pulses using mode-locking techniques[21] a sufficiently large emission gain bandwidth is required.

Ytterbium-doped potassium gadolinium tungstate (Yb:KGW) is a widely used solid-state gain medium for ultrafast laser systems. The large spectral linewidths of Yb in crystalline hosts, as compared with Nd, permits solid-state laser operation with sub-picosecond pulses, using direct diode pumping[72]. Even though Yb requires higher intensity pumping than Nd due to its quasi-three-level system, thermal effects in Yb lasers are reduced as a consequence of a smaller quantum defect[73]. The tungstate hosts also have a large optical absorption cross-section for the Yb dopant a desirable property for diode pumping[74]. Yb:KGW has a ~4nm absorption bandwidth that readily facilitates direct diode laser pumping at 980 nm, and its broad emission bandwidth around 1040nm can support ~100fs pulse durations. The reported average power for mode-locked (ML) operation of Yb:KGW lasers using a single element gain medium with a simple pump geometry is about 1 W[75]. In nearly all these laser systems, complex optical geometries (e.g., in thin-disk lasers) or dichroic mirrors (or polarization coupling methods) are used to direct the diode pump radiation into the gain medium to improve laser efficiency and generate higher power ML operation.

The Yb:KGW laser oscillator used as the front-end radiation source for the spectral photocathode characterization measurements described in this Thesis employs a much simpler diode pumping geometry which incorporates the in-house developed thermal lens shaping (TLS) technology[76] to compensate for astigmatism in the laser resonator while providing for efficient pumping and access to the broadest emission bandwidth of the gain medium. The oscillator employs a non-Brewster Yb:KGW crystal geometry, in which a single 193nm thick SiO_2 anti-reflection coating is applied to both polished 3×10 mm crystal faces to ensure that reflection losses are minimized for both the *p*-polarized 1046nm cavity radiation and the *s*-polarized diode pump radiation. To ensure a high pump-to-output lasing efficiency, the Yb:KGW crystal has 2at.% Yb dopant concentration to absorb more than 90% of the pump radiation[21]. Two 35 W dual-axis collimated and TM-polarized laser diode arrays operating at 980 nm (HLU35C10x5-980 from LIMO GmbH[77]) are used to achieve efficient pumping in a counter-propagating geometry. The 3.7 nm full-width half-maximum (FWHM) 980 nm absorption line of Yb:KGW was well-matched with the ~3nm emission linewidth of the two laser diode arrays[78–80]. With 100 mm focal length lenses, this allows the pump radiation to be focused on to a pump spot diameter of ~400 μm, yielding a maximum pump irradiance of ~28 kW/cm^2 from one laser diode array[21].

3.1.2 <u>The Yb: KGW laser cavity</u>

Although, the basic design of the diode pumped Yb: KGW femtosecond laser used for electron pulse generation was not part of my thesis work, the previous laser resonator configuration was modified to obtain the higher pulse powers required to run an optical parametric amplifier (OPA) and hence generate the tunable UV radiation for the photocathode

studies. Full details of the laser head design can be found elsewhere[21,76]: Here, I will briefly review the changes to the laser resonator design. The primary modification was to increase the length of the asymmetric *z*-fold cavity to 5.35m to reduce the repetition rate by a factor of 2 in order to increase the energy per pulse. As shown in figure 3.1, this was achieved by increasing (i) the radius of curvature of the cavity's focusing mirrors and (ii) the overall length of the resonator to maintain the laser mode size in the gain medium.

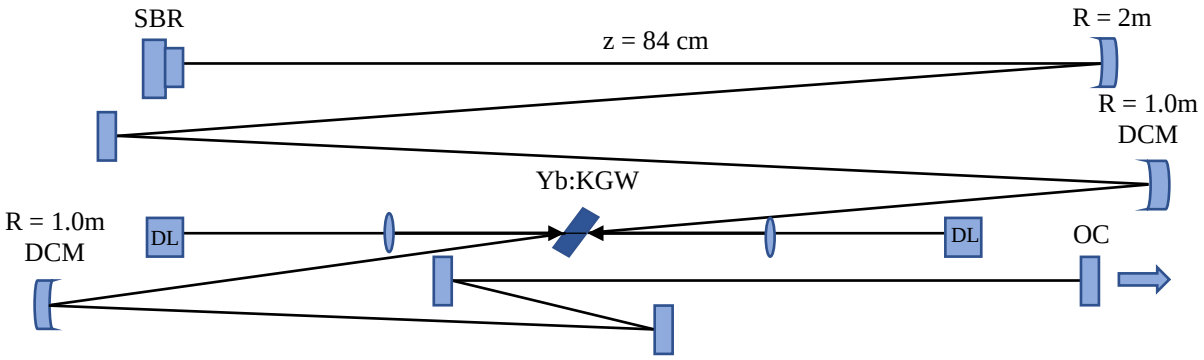

Figure 3.1: Schematic of the femtosecond TLS Yb:KGW laser oscillator.(DL- diode laser, OC- output coupler, SBR- saturable Bragg reflector, DCM- dispersion compensating mirror).

The two dispersion compensating and focusing (DCM) mirrors either side of the Yb:KGW gain medium were replaced by mirrors with a radius of curvature of 1m and a with group velocity dispersion (GVD) of –550(±50) fs^2 [81] at 1040nm. These mirrors are positioned 55 cm from the gain medium to maintain resonator stability while compensating for the pump-induced thermal lens effect in gain medium. The laser diode pump geometry is retained as the required TLS astigmatism compensation for the longer laser resonator is unchanged. The shorter arm of the resonator terminated by the 7% output coupler is increased in length to ~1.5m using an additional *z*-fold section of two flat DCM mirrors with a GVD of –550(±50) fs^2. The longer arm of the resonator terminated by the saturable Bragg reflector

(SBR) was also lengthened by a factor of two to ~2.5m using a flat folding mirror and a 2m radius of curvature mirror to focus the intracavity radiation onto the SBR. The SBR has a 1% reflectivity modulation depth at the 1046nm laser wavelength and is positioned at z = 84cm from its intracavity focusing mirror in order to compensate for its absorption-induced thermal bowing[82]. This cavity configuration allows the mode-locked Yb:KGW laser to maintain its 250fs pulse duration and 2W output power, but now a 28MHz repetition rate which boosts the output pulse energy to ~70nJ – a 280kW peak pulse power.

3.1.3 Optical parametric amplification and tunable UV generation

(a)

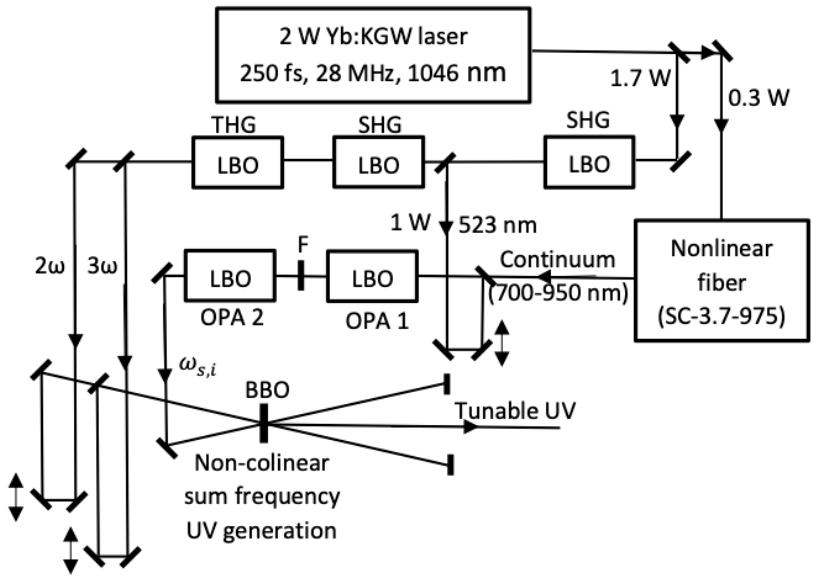

(b)

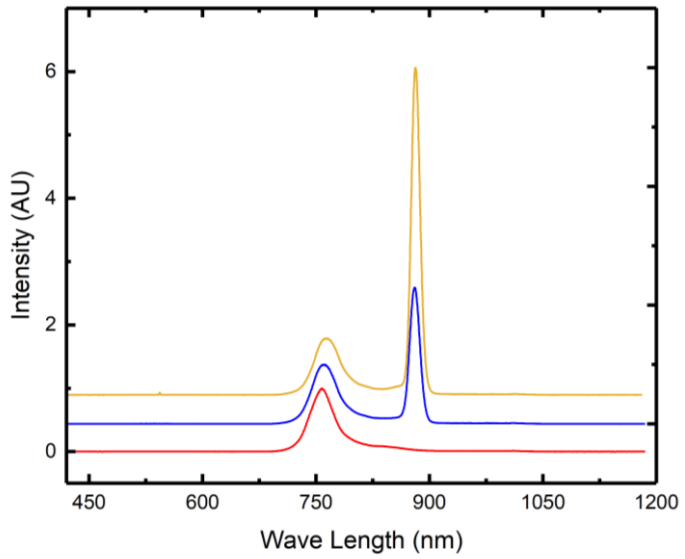

Figure 3.2: (a) Schematic of 28 MHz tunable UV laser radiation source: LBO= Lithium triborate, OPA= Optical parametric amplifier for amplification of signal and idler frequencies $\omega_{i,s}$, BBO = β-Barium borate, SHG= second harmonic generation of frequency 3ω and F = filter suppressing idler wave. (b) Optical parametric amplification at 870nm; continuum seed radiation (lower spectrum), spectrum after OPA1 (middle spectrum), and spectrum after OPA 1and OPA2 (top spectrum).

The ultra-short pulse radiation from the 2W mode-locked Yb:KGW laser oscillator is split into two to generate the continuum seed and green pump radiation for the OPA (Figure 3.2). the main 1.7W portion is frequency doubled in a 5mm non-critically phase matched (NCPM) Lithium triborate (LBO) crystal to produce ~1W at 523nm. The spatial mode size of this pump radiation is matched to that of the continuum radiation in the OPA stages and optical delay stages are used to ensure proper temporal overlap of the pump and continuum pulses. The residual 0.3W of the laser output power is coupled into a 50cm-long nonlinear fiber (SC-3.7-975, NKT Photonics) with a mode field diameter of 3.2μm to generate a stable super-continuum that extends to ~650nm on the short wavelength side of the 1046nm input (Fig. 3.2). Silver-coated off-axis parabolic mirrors are used to first collimate and then focus the picosecond pulses of continuum radiation into a 10mm-long, temperature-tuned NCPM LBO crystal that acts as a first stage of optical parametric amplification (OPA) using the temporally and spatially coincident co-linear ~140kW peak power green pulses as the pump radiation. After a 5:3 relay-imaging magnification from the ~40μm-diameter spot size for both the pump radiation and amplified continuum in the first OPA stage, the pulses in both beams are again temporally and spatially overlapped in a second OPA consisting of two back-to-back, critically phase-matched (i.e., angle-tuned), 15mm LBO crystals. A 1.5mm *a*-cut a-barium borate crystal is inserted between the two LBO crystals to compensate for the group velocity difference between the pump and amplified signal frequency pulses. A filter between the two OPA stages blocks the idler radiation generated in the first OPA to provide for a clean parametric amplification for the 700-920nm signal radiation and generation for the 1.2-2.0μm idler radiation in the second OPA stage. Fig. 2(b) shows the typical performance of the 28MHz continuum seeded OPA at a signal wavelength of 870nm; the first OPA stage amplifies the horizontal polarization component of the un-polarized continuum by a factor of ~10, and a further signal wave amplification of ~3 is achieved in the second OPA stage.

To generate the tunable UV radiation, the amplified signal and idler radiation is sum frequency mixed in 2mm-thick β-barium borate (BBO) crystals with either the second or third harmonics of the fundamental 1046nm Yb:KGW laser radiation. The latter are produced from the residual ~0.7W of fundamental radiation after the initial frequency doubling using a sequence of two critically phase-matched 1cm LBO crystals. Optical delay stages and relay imaging optics are employed to ensure optimal spatial-temporal overlap for the sum frequency generation which is performed in a non-collinear geometry to allow the generated UV to be readily separated – dichroic optics not being readily available in the UV. The resultant UV radiation is tunable from 4.2 to 5.3eV using sum frequency generation with the third harmonic at 356nm and from 3.0 to 4.1eV using the second harmonic at 523nm. It has a pulse duration of ~1ps and a power of ~10μW over the entire UV tuning range. A 2:1 magnification telescope is used to relay image the UV radiation onto the photocathode face. Together with the 3.56eV and 4.75eV third and fourth harmonics, the laser system provides almost continuous UV tunability from 3.0 to 5.3eV (i.e., 234-413nm).

3.2 The photocathode characterization system

Like the laser-based tunable UV radiation source, the photocathode characterization vacuum system was built from the ground up with many of the components being designed and built in house. The design and construction of the electron gun and electron beam measurement system is not a part of my thesis, and a full description can be found somewhere else[83]. Briefly, the electron gun design is a truncated version of the Butler gun design[84,85]; specifically, it is a Butler gun of three-quarter length with its anode and cathode shaped to generate a parabolic shape to the longitudinal acceleration field so that, in the non-relativistic

limit, the net transverse electro-static lensing in the gun is zero[83]; i.e., the beam divergence caused by the spatially convergent acceleration field at the gun anode (the 'anode lens') is significantly reduced. The output of this 20kV DC photoelectron gun, which can accommodate planar photocathodes with diameters of 8-10mm, is directed through two counter-wound cylindrical (solenoid) magnetic lenses that form part of a solenoid scan technique[86] to determine the MTE of the photo-emitted electrons. The electron beam spot size is measured using a Ce:GAGG[22] scintillator screen (1:1 imaged onto a CCD camera) as a function of the focal strength of the magnetic lenses, and the initial MTE of the electrons photo-emitted from the photocathode is extracted by comparison to an extended analytical Gaussian (AG) model[11,23] simulation of the electron pulse propagation through the experimental system. To ensure accuracy in the beam propagation simulations, the focal strength of the magnetic lenses as a function of the solenoid current is carefully characterized and a finite element analysis is used to determine the exact shape of the near parabolic axial acceleration field in the gun – both being a required input data for the AG model.

In these studies, conducted at 300K, the 8 to 10mm diameter planar single-crystal photocathode is co-axially inserted in the cathode and irradiated at a 60° angle of incidence by the UV radiation. The spatial dimensions of the incident Gaussian UV laser beams, which is also an input parameter for the AG model simulation, are determined by translating a 10 or 25μm pin hole across the beam and monitoring the throughput using a GaP photodiode. Accounting for the factor of 2 increase due to the 60° angle of incidence in the horizontal (x) direction, the measured Gaussian half-width 1/e maximum (x, y) irradiance spot sizes at the photocathode surface are; (240, 80)±5μm for the tunable UV radiation generated using third harmonic (4.2-5.3eV), (240, 110)±5μm for the tunable UV radiation generated using the second harmonic (3.0-4.1eV), (330, 150)±5μm for the fourth harmonic at 4.75eV, and (240, 120)±5μm for the third harmonic at 3.56eV. For all the measurements, the intensity of the UV radiation

incident on the studied single-crystal metal photocathodes was kept below 100kWcm^{-2} to ensure that nonlinear (e.g. two-photon) photoemission mechanisms did not play a role.

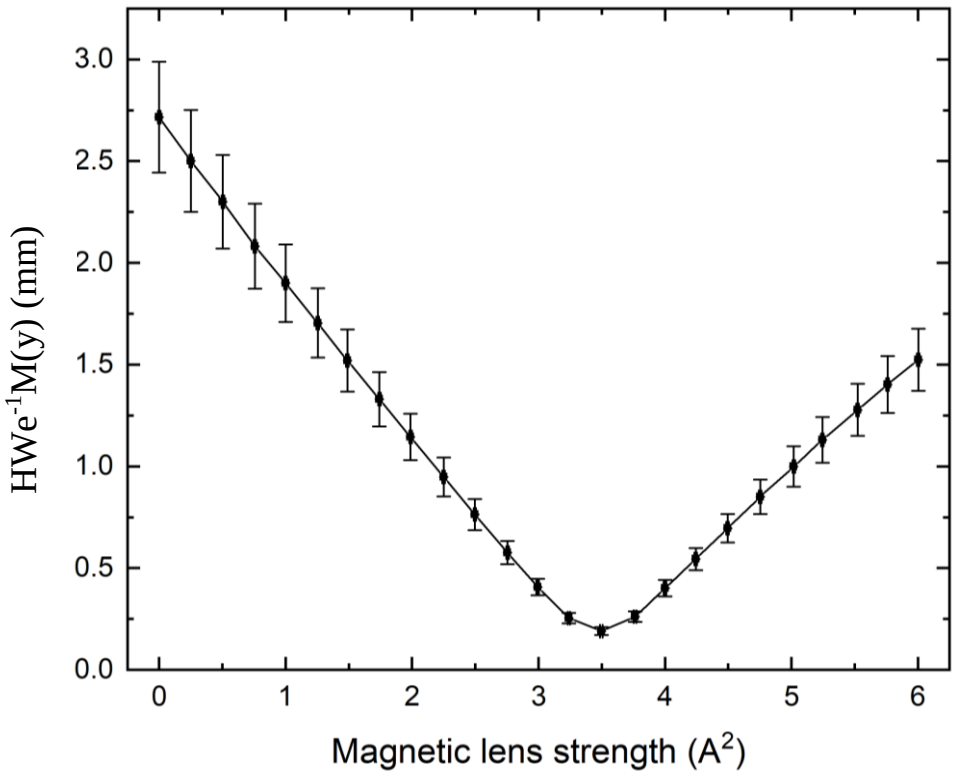

Figure 3.3: Full solenoid scan; measured half-width 1/e maximum vs magnetic lens strength (solenoid current^2) for Mo(001) at 4.75 eV photon energy.

Figure 3.3 shows a representative example of a solenoid scan used to obtain a value for the MTE of the photo-emitted electrons, in this case for Mo(001) at ħω = 4.75eV. The value for the plotted electron beam spot size (in either the *x* or *y* directions) at each solenoid current is extracted from the pixelated CCD image of the beam using a Gaussian fit function in a Matlab code. For convenience, the square of the solenoid current is plotted, because the double action of a solenoid lens ensures that its focal strength is proportional to the square of its magnetic field and, hence, the square of the current through its coils[83]. The solid line shows the electron beam size on the Ce:GAGG scintillator screen as a function of solenoid current

simulated by the extended AG model for electron propagation through the photocathode characterization system when the initial MTE is 325meV. The electron beam spot size at zero solenoid current (i.e. unfocused or free beam propagation), which increases with increasing MTE, and the solenoid current at the focus (~1.8A), where the laser-beam-dependent photocathode emission area is effectively imaged onto the scintillator, benchmark the solenoid scan technique. In general, the AG model fit to the experimental solenoid scan data allows for the extraction of the MTE with an error of around ±10%, although this is dependent on the signal-to-noise in the Gaussian fits to the electron beam images. For weak signals from photocathodes with low QE, the initial linear rate of change of the beam spot size with the square of the solenoid current (from 0 to 1A) is also used to extract an MTE value at a particular incident photon energy as this allows for an averaging over ~5 spot size measurements.

For the photoemission QE measurements as a function of photon energy, the scintillation screen is replaced by a 5mm-diameter aperture Faraday cup connected to a pA meter. The current in the solenoid scan lenses is set so that the electron beam is focused at the Faraday cup to ensure all emitted electrons are collected. The incident laser power is monitored before the last Al turning mirror (directing the UV light onto the photocathode) and the UV-grade fused silica vacuum system window using a calibrated photodiode power meter with sensitivity into the 10nW range. The known reflectivity of the Al mirror and transmission of the fused silica window as a function of UV wavelength is included in the QE evaluation.

CHAPTER 4

SINGLE CRYSTAL Rh(110) PHOTOCATHODE

In chapters 2 and 3, respectively, the one-step photoemission formalism and the experimental setup have been introduced. This chapter deals with, to my knowledge, the first verification of the direct connection between the electronic band structure of a solid-state photocathode material and its experimentally determined spectral photoemission properties; specifically, the mean transverse energy (MTE) and quantum efficiency (QE). This connection is verified for a single crystal Rh(110) photocathode using fully relativistic (including spin-orbit coupling) *Ab initio* band structure calculations to determine with sufficient accuracy the energy-momentum dispersion(s) of the emitting electronic states and an exact quantum solution for transmission over and through a triangular barrier[38] that is extended into the transverse dimension and includes the physics of the vacuum states[20] (Chapter 2). The predicted spectral dependence of the MTE and QE of the Rh(110) photocathode is in very good agreement with experimental data obtained using the solenoid scan technique and Faraday cup measurements that employ an ultraviolet radiation source tunable from 3.0 to 5.3eV (235-410nm) (Chapter 3). Further, in the last section of this chapter, I will compare the presented theoretical and experimental work on the Rh(110) photocathode with prior photoemission analyses to demonstrate the veracity of the approach presented in this thesis. The resultant benchmarking for the evaluation of photocathode emission properties using *Ab initio* methods is expected to allow for the development of screening tools to select promising high brightness solid-state photocathodes.

4.1 Rh Band structure along Γ – K

The band structure calculation for Rh was outlined in chapter 2, and figure 4.1 shows the relevant portions of the band structure of Rh for photoemission in the (110) crystal direction (the Γ − K direction in the Brillouin zone) and the relevant dispersions of the emitting bands in the transverse directions calculated using the DFT evaluated crystal parameters. For convenience, the Fermi level depicted by the horizontal line is set to zero energy. Our electronic band structure is almost identical to that of N. E. Christensen [87] and indicates that only two electron bands are expected to contribute strongly to photoemission from Rh(110) when $\Delta E < 1eV$; the Σ_1 and Σ_2 bands labeled Band 1 and Band 2, respectively, in the reduced zone scheme of Fig. 4.1(a). These two photo-emitting bands reside in the first and second Brillouin zones, respectively, as shown in the unfolded zone representation of Fig. 4.1(b) [88]. Also evident from the band structure is that there are no other bulk electronic states around the vacuum level (dashed line in Fig. 4.1(a)) that can affect the photoemission mechanism; that is, photoemission from Rh (110) can only be a one-step process.

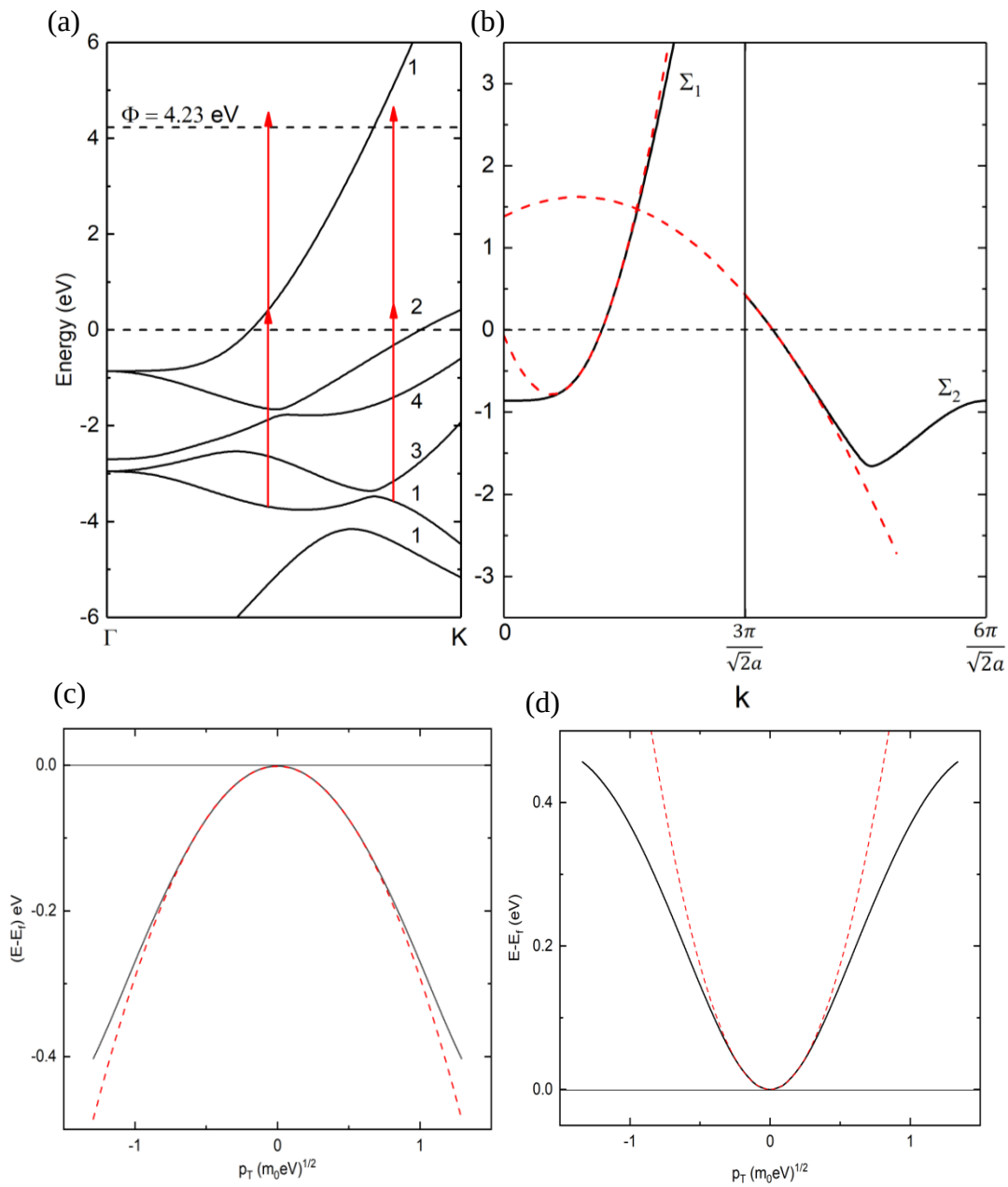

Figure 4.1: Band structure of Rh along the $\Gamma - K$ direction with the Fermi energy set to zero. (a): Reduced zone scheme with the Brillouin zones of each band numerically labeled and the vacuum level associated with the measured 4.23eV work function (dashed line). Two possible resonant two-photon photoemission schemes at $\hbar\omega \approx 4.1$eV are also shown. (b): Unfolded zone scheme for the first two Brillouin zones with the longitudinal parabolic dispersion fits (dashed red lines) to the emitting Σ_1 and Σ_2 bands that cross the Fermi level. (c), (d): The transverse band structure calculated at the Fermi level for the band 1 (Σ_1) and band 2 (Σ_2) with a parabolic dispersion fit (red-dashed line).

For excess photoemission energies less than 1eV, the Σ_1 and Σ_2 emitting band states in the vicinity of and just below the Fermi level may both be well approximated by a cylindrical parabolic dispersion of the form

$$E(p) = E_0 + \frac{(p_z - p_0)^2}{2m_z} + \frac{p_T^2}{2m_T}, \tag{4.1}$$

where m_z is the longitudinal electron effective mass in the $\Gamma - K$ emission direction with momentum p_z, m_T is the electron effective mass in the transverse direction with momentum p_T, p_0 defines the longitudinal momentum of the minimum or maximum of the parabolic band in this approximation, and E_0 is the energy of the latter momentum point with respect to the zero-energy Fermi level (Fig. 4.1). The longitudinal components and of the parabolic dispersion approximations are shown by the red-dashed curves in Fig 4.1(b), and the parabolic dispersion relationships for the transverse directions are shown by the red-dashed curves in Fig 4.1(c) and (d). The extracted parameters m_z, m_T, p_0, and E_0 for the Σ_1 and Σ_2 bands are listed in Table I using units of electron volts (eV) and the free electron mass m_0. These parameters are employed in the comparison of the experimental measurements of the spectral dependence of the MTE and QE with our one-step photoemission model.

Table I: Parabolic dispersion band parameters- Rh(110)

	Band 1 (Σ_1)	Band 2 (Σ_2)
m_z	$0.7m_0$	$-5.0m_0$
m_T	$-1.7m_0$	$0.72m_0$
p_0 ($\sqrt{m_0 . eV}$)	1.0	1.1
E_0 (eV)	–0.8	1.6

4.2 Mean transverse energy- Rh(110)

The spectral dependence of the measured MTE for the Rh(110) photocathode is shown in Fig. 4.2 together with the results of a one-step parabolic band photoemission simulation[20] (solid and dashed lines) employing a work function of 4.23eV (see Section 3.1.3). The simulation is an extension of the exact triangular barrier transmission solution of R.G. Forbes and J.H.B. Deane[38] for photoemission from a parabolic band with its dispersion described by longitudinal (m_z) and transverse (m_T) effective masses (equation 4.1); that is, it employs the parameters listed in Table I to simulate the emitting Σ_1 and Σ_2 electronic bands for Rh(110).

The two dashed lines in Fig. 4.2 shows the MTE of electron emission predicted by the one-step simulation for the Σ_1 and Σ_2 electronic bands. The simulated relative QE from each band as a function of excess photoemission energy is then used as a weighting to evaluate the theoretically expected MTE from Rh(110) as a function of incident photon energy; that is, the emission from each band is assumed to be independent. The resulting spectral trend predicted by the one-step parabolic band photoemission simulation, shown by the solid line in Fig. 4.2 is clearly in very good agreement with the experimental data. We note that the Σ_2 band dominates photoemission from Rh(110) since its density of states at zero transverse momentum ($p_T = 0$) is significantly larger than that of the Σ_1 band at all investigated excess energies; specifically, the magnitude of m_z is 7× greater for Band 2 than Band 1 (Table I).

The experimental data also indicates a small increase in MTE at negative excess energies of around –0.15eV when the incident photon energy is about 4.1eV (300nm). This may be due to either (or both) of the two resonantly enhanced two-photon photoemission processes depicted Figure. 4.1(a): Two photons could excite electrons from a lower band in the

same first Brillouin zone via either a one- or two-photon resonance with the Σ_1 band using ~4.1eV photons to produce electrons with a small 0.1-0.2eV excess energy, thus increasing the measured MTE. This emission process has not been included in our one-step photoemission simulation.

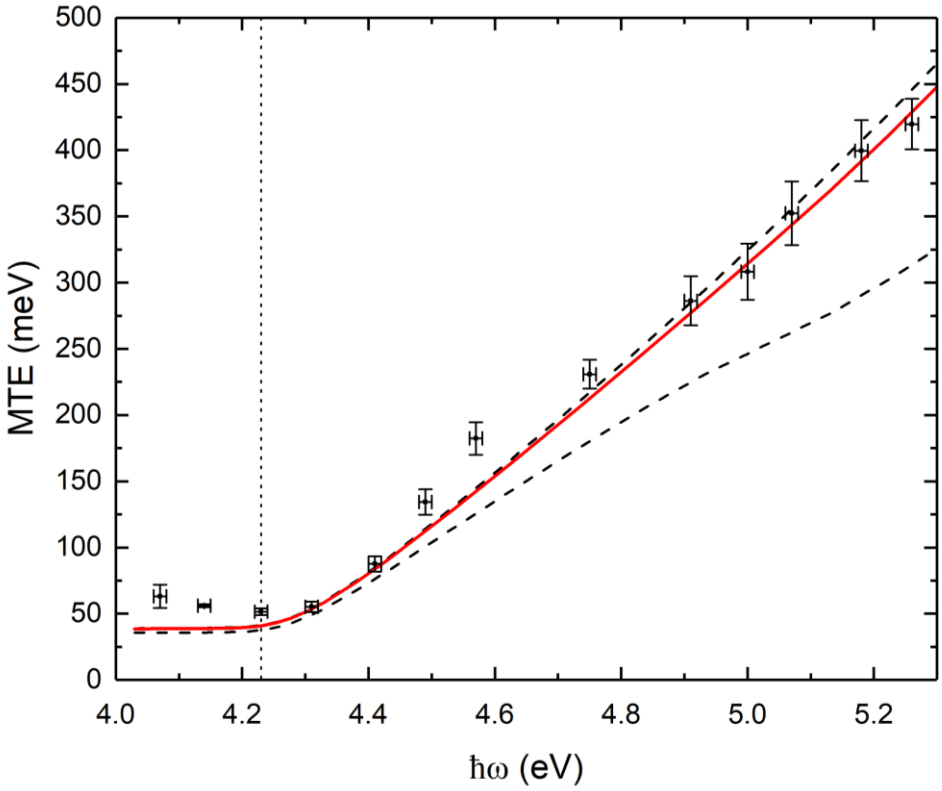

Figure 4.2: Mean transverse energy of emitted electrons from Rh(110) and a function of incident UV photon energy (ħω): Experimental solenoid scan measurements (data points); theoretical MTE evaluated from the one-step photoemission simulation for Band 1 (lower dashed line) and Band 2 (upper dashed line); total simulated MTE for Rh(110) emission (solid red line). The vertical dotted line indicates the measured 4.23eV work function.

Also notable is that the one-step photoemission simulation predicts that the MTE will level off to a constant value of 39meV for incident photon energies below the 4.23eV work function. This value is 56% larger than the 300K limiting value of $k_B T_e$ = 25meV predicted by the polylogarithmic formulation developed by Vecchione et al.[19]. Roughly 70% of this difference is accounted for by the use, in their analysis, of an effective electron mass equal to the free electron mass m_0 in the photocathode material and the omission of both the parabolic

emission bands and the vacuum state physics[20]. The rest is due to the 'abnormal' nature of the emission bands; specifically, the fact that both bands have opposite signs for the longitudinal and transverse effective masses. This dispersion difference provides for electronic states at higher transverse momenta that may emit in the Boltzmann tail of the photo-excited electron distribution extending above the vacuum level. Nonetheless, our one-step photoemission analysis predicts that sub-10meV MTE values can be attained using Rh(110) at photoemission threshold ($\Delta E = 0$) provided the photocathode is cooled to below 70K and laser-induced heating[89] does not increase T_e (temperature dependence of MTE explained in 2.5.1 section).

For excess photoemission energies greater than ~0.7eV, our band structure calculation (Fig. 4.1) indicates that emission from other filled states below the Fermi level is possible; first from the Σ_4 band in the fourth Brillouin zone just above $k = 9\pi/(\sqrt{2}a)$ and then from the extension of the Σ_2 band just below $k = 6\pi/(\sqrt{2}a)$. However, the contribution to the electron emission from these states is expected to be only a few percent of that from two simulated bands that cross the Fermi level as their effective excess photoemission energies are 0.7-0.8eV lower. In previous theories [30], a quadratic dependence of the excess energy (ΔE^2) was assumed for QE; that is, even under this dependence, at ~0.1eV excess energies for these bands they would contribute about $(0.85/0.1)^2 = 72$ times less to photoemission than the two bands used in the simulation.

4.3 Quantum efficiency and work function- Rh(110)

Figure 4.3 displays the measured spectral dependence of the QE for Rh(110), expressed as emitted electrons per absorbed photon using the 45-56% surface reflectivity evaluated from

the known complex refractive index Rh[90] over the measured 236-288nm spectral range. The QE increases by three orders of magnitude from ~10^{-8} electrons/photon (the detection limit for the measurement) at $\hbar\omega = 4.31$eV to over 3×10^{-5} electrons/photon at $\hbar\omega = 5.26$eV where $\Delta E \approx 1$eV. The optical properties of Rh[90] indicate that the high optical surface reflectivity for the *p*-polarized UV light incident at 60° is due to total internal reflection since the real part of the photocathode's refractive index is less than unity over the measured wavelength range. However, at near normal incidence, the surface reflectivity of Rh increases to over 60%. We also note that nonlinear (e.g. multi-photon) photoemission was not observed in our QE measurements as they were all performed (i) at incident peak pulse laser intensities less than ~100kW/cm^2 and (ii) at photon energies above the photoemission threshold which excludes the possible two-photon transitions at $\hbar\omega \approx 4.1$eV. In addition, these QE results place an upper limit of ~100 electrons/pulse for the solenoid scan measurements with the tunable UV radiation source – a pulse charge for which the AG electron pulse propagation simulation indicates that intra-pulse space-charge effects are negligible and so will not affect the extraction of the MTE values presented in Section 4.2[23].

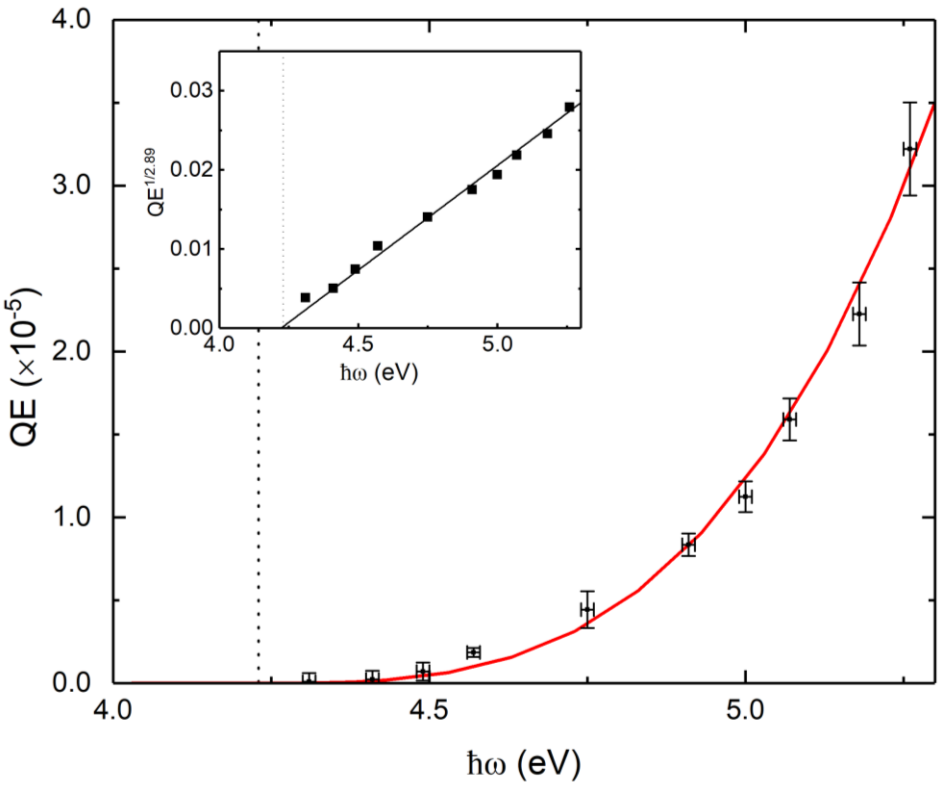

Figure 4.3: Quantum efficiency (QE) per absorbed photon of Rh(110) as a function of incident UV photon energy (ħω): Experimental measurements (data points) and linearly-scaled fit of the simulated QE for Rh(110) emission (solid red line). Inset: Extraction of the 4.23eV work function (vertical dotted line) using $(QE)^{1/2.89}$ vs. ħω.

The theoretical spectral dependence of the QE obtained from our one-step photoemission simulation, using the same two bands employed for the MTE calculation (Fig. 4.2), is plotted as the solid line in Fig. 4.3. As the matrix element associated with the photo-excitation is not directly included in the photoemission simulation, the total summed two-band QE evaluated from the photoemission model is scaled linearly to fit the experimental data. Clearly, the theoretical simulation is in very good agreement with the spectral dependence of the QE measurements. It also indicates that the QE does not follow the Fowler-DuBridge quadratic scaling of the QE with excess photoemission energy[26,30]; that is, $QE \neq A.(\Delta E)^2$, where A is a constant. Instead, it predicts a ΔE power law scaling with an exponent of around

2.89(±0.05), which is a direct result of the inclusion of bulk band and vacuum states in our photoemission analysis[20]. Armed with this knowledge, one can employ the analysis method of Gobeli and Allen[51] to extract the work function for our Rh(110) photocathode: Namely, a plot of $QE^{1/2.89}$ against photon energy provides a linear dependence the abscissa intercept of which gives a value for the work function[51,91]. The inset of Fig. 4.3 shows that such an analysis gives a work function of 4.23(±0.05) eV – the value that is employed in our one-step photoemission simulations shown in Figs. 4.2 and 4.3. In contrast, the work function calculated using the thin-slab technique[11,58,68] (see chapter 2, section 2.6.2) gives a value of $\phi_{Rh(110)}$ = 4.70(±0.05)eV, which is ~0.5eV above our extracted experimental value. Although Rhodium is not known to react strongly with oxygen, this discrepancy is likely due to a dipole induced by a thin (~1 mono-layer) surface oxide. Certainly, the (110) face of face centered cubic metals is generally more reactive than other low-index crystal faces[92].

4.4 Comparison to prior photoemission theories

For completeness, in figure 4.4 I compare the prior photoemission theories (presented in chapter 2) to the spectral measurements of the MTE and QE for the single-crystal Rh(110) photocathode. Figure 4.4 (a) compares the experimental MTE data to the theoretical formulation of Dowell and Schmerge[18] for which MTE = $\Delta E/3$ (dashed black line), and the more recent poly-logarithmic expression derived by Vecchione et al.[19] (equation 2.6) (solid black line). These theoretically predicted values, which use the extracted work function value of 4.23eV (figure 4.3), are below experimental data for all incident photon energies due, primarily, to the fact that they do not consider the bulk band and vacuum density of states. The unusual nature of the dispersion of the two emitting bands for Rh(110) clearly also plays a role.

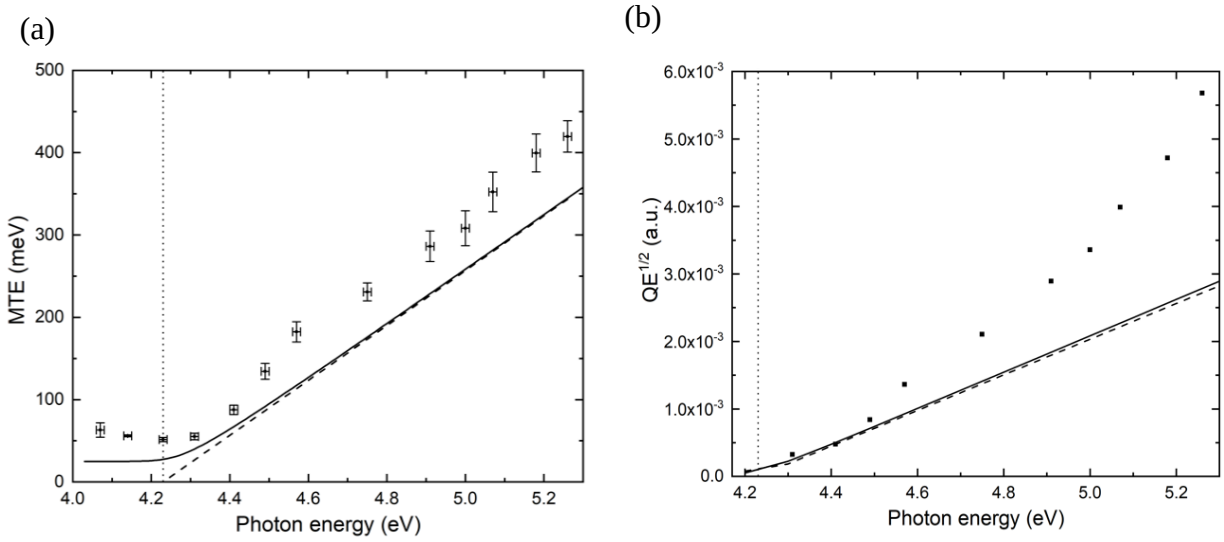

Figure 4.4: Mean transverse energy of emitted electrons from Rh(110) as a function of incident UV photon energy (ħω): (a) represents the experimental solenoid scan data with error bars (data points); MTE calculated using Vecchione's analysis (equation 2.6) (solid black line); MTE calculated using Dowell-Schemrge theory (MTE = $\Delta E/3$) (dashed black line). (b) $QE^{1/2}$ as a function of photon energy(ħω): the experimental Faraday Cup QE (data points); QE calculated using Vecchione theory (equation 2.7) (solid black line); QE calculated using Fowler-DuBridge relation (dashed black line). The vertical dotted line indicates the measured 4.23eV work function.

In the figure 4.4 (b), the QE values measured using the Faraday cup are again compared to the expression derived by Vecchione et.al. (equation 2.7)[19] (solid black line) and also to the Fowler-DuBridge relation[26,30] of a quadratic power-law dependence (black dashed line); i.e., $QE = A(\Delta E)^2$. To highlight the power-law dependence, I have plotted $(QE)^{0.5}$ against ħω, which linearizes both prior theoretical expressions over the experimental data range (again using the extracted 4.23eV work function (figure 4.3)), and fitted both theoretical dependences to the measured QE at ħω = 4.41eV through the S_{12} and A parameters respectively. It is evident that neither theoretical formulation agrees with the measured trend. Again, this is due to the omission of the physics of the emitting band and recipient vacuum states in both prior photoemission theories.

Together, both (a) and (b) in figure 4.4 indicate the need for a new theoretical explanation for photoemission from solid-state photocathodes that is more consistent with experimental data. The one-step photoemission analysis presented in this thesis is certainly in better agreement with the measured spectral dependences of the MTE and QE for the Rh(110) photocathode as it includes a direct connection between the electronic band structure of the solid-state photocathode material and its spectral photoemission properties.

CHAPTER 5

BODY-CENTERED CUBIC METAL PHOTOCATHODES

In chapter 4, the experimental data obtained using the solenoid scan technique and Faraday cup measurements was compared to the predicted spectral dependence of the MTE and QE using the face-centered cubic (fcc) Rh(110) photocathode as an example. The purpose of this chapter is to investigate the experimental emission properties for two single-crystal body-centered cubic (bcc) metal photocathodes; Mo(001) and W(001). The group VIb elements Molybdenum and Tungsten are attractive photocathode materials due to hardness, high melting points, and relative chemical inertness[93,94]. The presented results will show that the predicted theoretical dependence of the MTE is consistent with, but not in complete agreement with, the experimental data, even though full relativistic effects and spin-orbit coupling are included in my *Ab initio* band structure calculations. As was the case for Rh(110), for both bcc metal photocathodes I will include the DFT-based thin-slab evaluations of the work function and the fit functions in the cylindrical approximations to the band structure that are employed to predict the MTE and QE using the one-step photoemission formalism. The latter are, in general, not as exact as for Rh(110) and so, together with the need to model multi-band emission for both Mo(001) and W(001), likely contribute to the discrepancy between the spectral measurements and the one-step photoemission simulation.

5.1 Molybdenum

5.1.1 Mo Band Structure

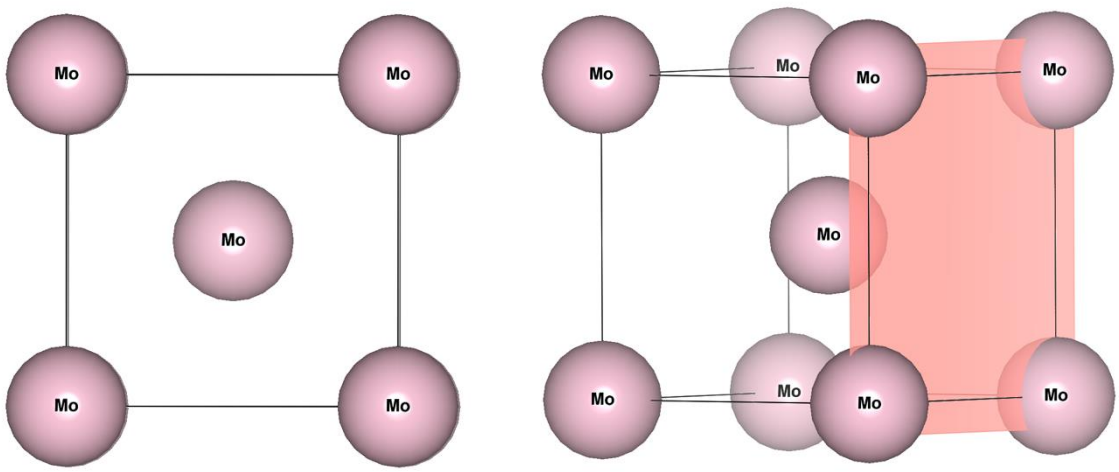

Figure 5.1: Mo crystal structure; Body-centered cubic structure with optimized lattice constant a = 3.069 Å. Right panel is the top view and left panel is the 45^0 rotated view with (001) plane. The unit cell contains 2 atoms. (1/8*8 for corners and 1 at the center)

The DFT calculations for the bulk Mo crystal again include full relativistic effects, with spin-orbit coupling included during the plane wave self-consistency iterations. In other words, a fully relativistic pseudopotential within the generalized gradient approximation (GGA)[63] was employed, and the electronic wave function is described by a plane-wave basis set with an energy cut-off of 50 Ry, the energy cut-off for the charge density is set to 325 Ry, a threshold of 10^{-6} Ry for the ground state energy is used, and a Marzari-Vanderbilt smearing[64] with a broadening of 0.05 Ry is employed. The resulting DFT calculated body-centered cubic crystal structure for Mo has a lattice constant a = 3.069 Å, which is within 2% of the experimental value[95]. The crystal structure obtained using the optimized lattice constant is shown in figure 5.1. The Mo band structure (figure 5.2) is calculated along the k-path $\Gamma \xrightarrow{\Delta} H \xrightarrow{G} N \xrightarrow{\Sigma} \Gamma \xrightarrow{\wedge} P \xrightarrow{F} H$

in the first Brillouin zone, where Δ, G, Σ, Λ, and F are symmetry lines and their lengths are $\overline{\Gamma\mathrm{N}} = \sqrt{2}\pi/a$, $\overline{\Gamma\mathrm{P}} = \sqrt{3}\pi/a$, and $\overline{\Gamma\mathrm{H}} = 2\pi/a$. For convenience, the Fermi level depicted by the horizontal line is set to zero energy. My electronic band structure is identical to that of C. L. Fu[95]. The effective mass along longitudinal direction at the Fermi level ($k = k_f$) is calculated using the curvature of the relevant band, $m_z^* = \hbar^2 \left(d^2E/dk^2 \,|_{k=k_f}\right)^{-1}$, and the band structure along transverse direction at $k = k_f$ is evaluated to obtain the transverse effective mass m_T^* using a parabolic fit.

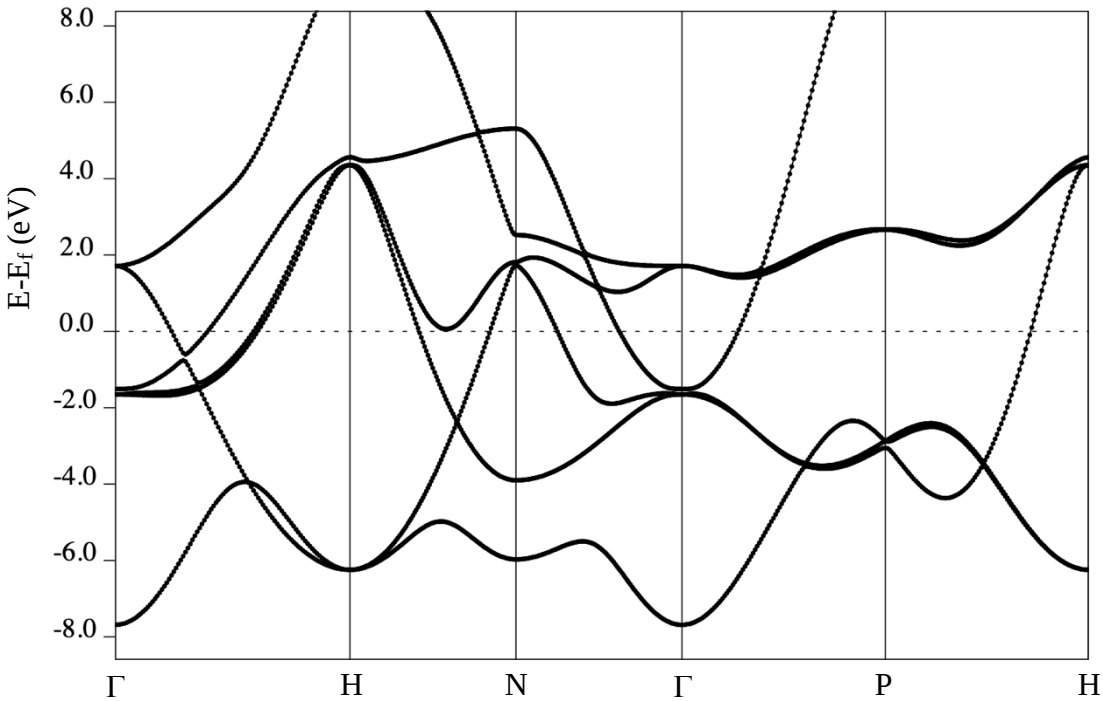

Figure 5.2: Mo band structure along high symmetry points. The horizontal line at 0 eV represents the Fermi level. Γ→ H (001), Γ→P (111), Γ→N (110) represent directions.

Figure 5.3 shows the Fermi surface for Mo calculated using a plane-wave basis set with 15×15×15 uniform k-grid points sampling the irreducible Brillouin-zone. The Γ − H direction is marked on the Brillouin zone using an arrow to show the Δ-symmetry line along with a clear

view of ‘lens’ feature in the band structure[95,96]. The relativistic band structure indicates that there are four electron bands that contribute to the photoemission for Mo(001).

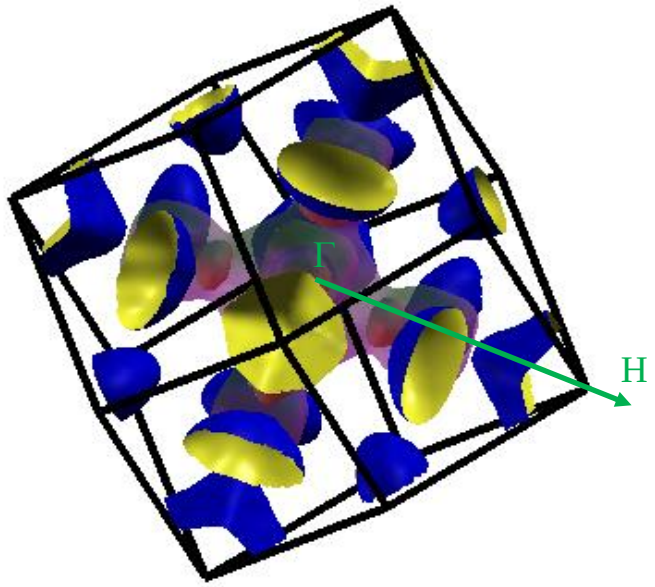

Figure 5.3: Mo Fermi surface calculated using DFT. The arrow indicates the $\Gamma - H$ direction in the first Brillouin zone. The figure clearly visualizes the “jack”, “electron lens” and “octahedron” along the Δ-symmetry line.

Emission from the (001) crystal face (the Γ→ H direction in the Brillouin zone) was selected for Mo due to the presence of several emission bands with a low transverse effective mass m_T that the photoemission analysis in chapter 2 indicates is required to achieve a low MTE. Figure 5.4 shows the relevant longitudinal portions of the band structure of Mo for photoemission in the (001) crystal direction. If one ignores the spin-orbit splitting (avoided crossings) at 0.7 and 1.4eV below the Fermi level, each of the four bands that cross the Fermi level can be well fit by parabolic functions (red dashed lines); Band 1 as a hole-like band and Bands 2, 3, and 4 with electron-like dispersion in the longitudinal direction. Bands 1 and 2 generate the well-known ‘lens’ features in the Mo band structure on the ends of the central ‘jack’ around the Γ point. Bands 3 and 4 produce the octahedral features centered at the H

points on the Fermi surface (figure 5.3). The spin-orbit interaction in Mo produces separations between these pairs of surfaces[96].

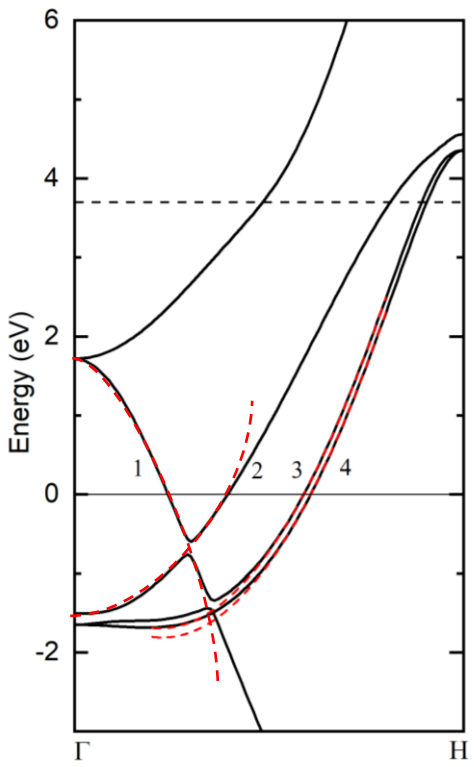

Figure 5.4: Band structure of Mo along the $\Gamma - H$ direction with the Fermi energy set to zero and the vacuum level associated with the measured 3.70eV work function (dashed line). The band structure includes parabolic dispersion fits (red dashed lines) to the emitting Bands 1, 2, 3 and 4 that cross the fermi level.

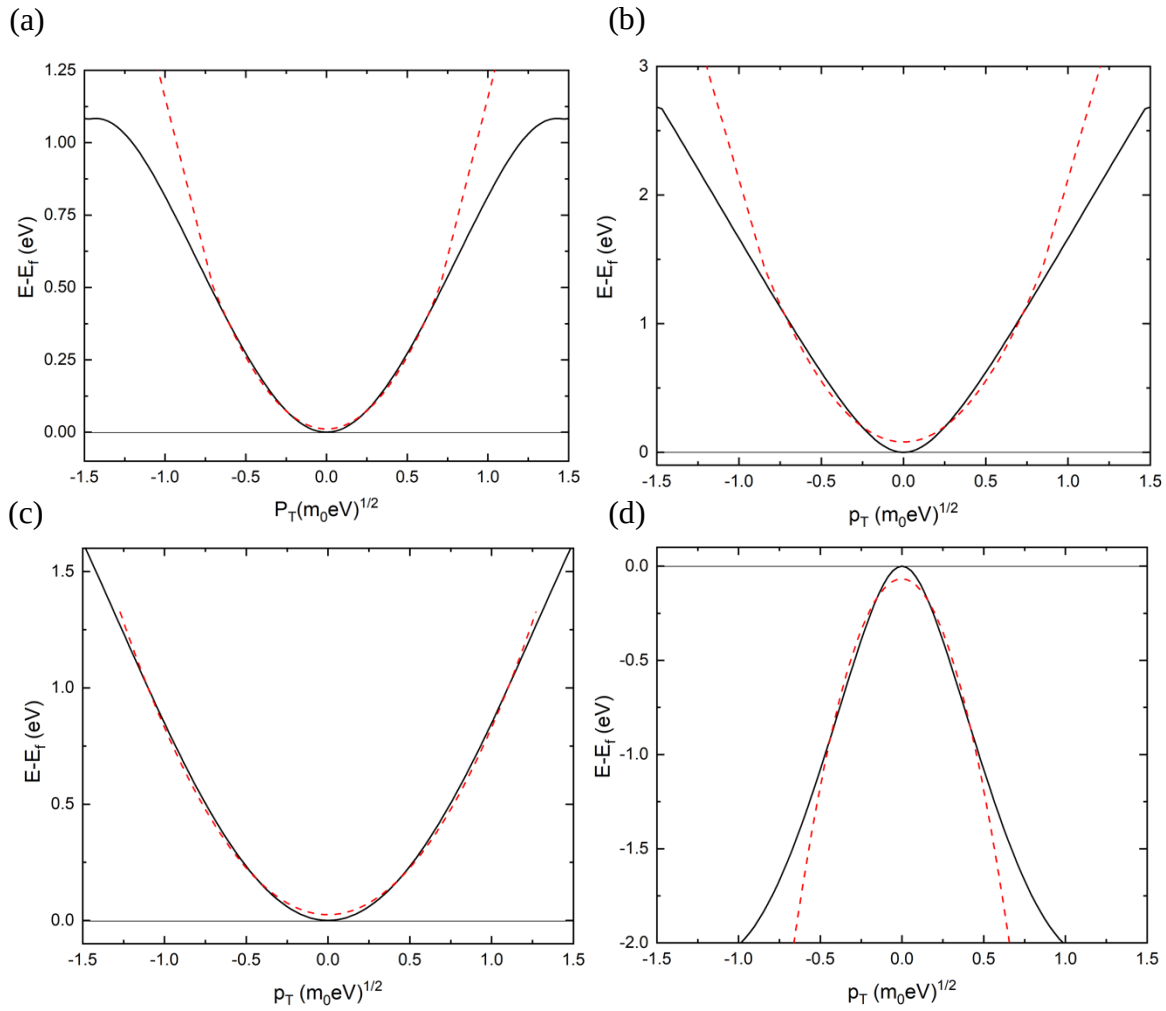

Figure 5.5: Transverse dispersion (black lines) and parabolic fits (dashed red lines) near the Fermi level for the four emitting bands labeled in figure 5.4: (a) Band 1, (b) Band 2, (c) Band 3, and (d) Band 4.

In the transverse direction, I have also evaluated a parabolic fit at the Fermi level for all four bands to allow the cylindrical parabolic dispersion relation of equation 4.1 to be used as the approximated fit functions in the one-step photoemission simulation for the emitting bands in the vicinity of and just below the Fermi level. These four transverse fits to the DFT-evaluated band dispersions are shown by the dashed red lines in figure 5.5 (a-d). Clearly, in contrast to the longitudinal direction (figure 5.4), in general all the emitting bands are not well approximated by a parabolic transverse dispersion over momenta of ±1.0 $(m_0.eV)^{1/2}$ which

corresponds to an excess energy of 0.5eV. In fact, the dispersion of Band 2 changes significantly as a function of energy (or longitudinal momentum p_z). Nonetheless, I will employ the obtained m_T values near the Fermi level in the cylindrical parabolic dispersion approximation of the four emitting bands as the input to the one-step photoemission simulation for Mo(001). Table II list the values of the parameters m_z, m_T, p_0, and E_0 in this approximation for the four bands in units of electron volts (eV) and the free electron mass m_0.

Table II: Parabolic dispersion band parameters – Mo(001)

	Band 1	Band 2	Band 3	Band 4
m_z	-0.863m_0	1.386m_0	1.27m_0	1.261m_0
m_T	0.45m_0	0.17m_0	1.67m_0	-0.225m_0
p_0 ($\sqrt{m_0 . eV}$)	-0.394	0.138	1.235	1.292
E_0 (eV)	1.71	-1.5	-1.6	-1.69

5.1.2 Quantum efficiency and work function- Mo(001)

As outlined in chapter 3 for Rh(110), the work function for a clean Mo(100) photocathode surface is calculated using the thin-slab technique[68]. The DFT-based work function calculation uses a 0.05 Ry Gaussian-spreading, fully relativistic pseudopotentials, and n×n×1 Monkhurst-Pack[57] k points to obtain convergence within 0.05eV. The value of 4.6(±0.2)eV extracted from this calculation is within the range of the accepted value of 4.46(±0.21)eV for $\phi_{Mo(001)}$[41].

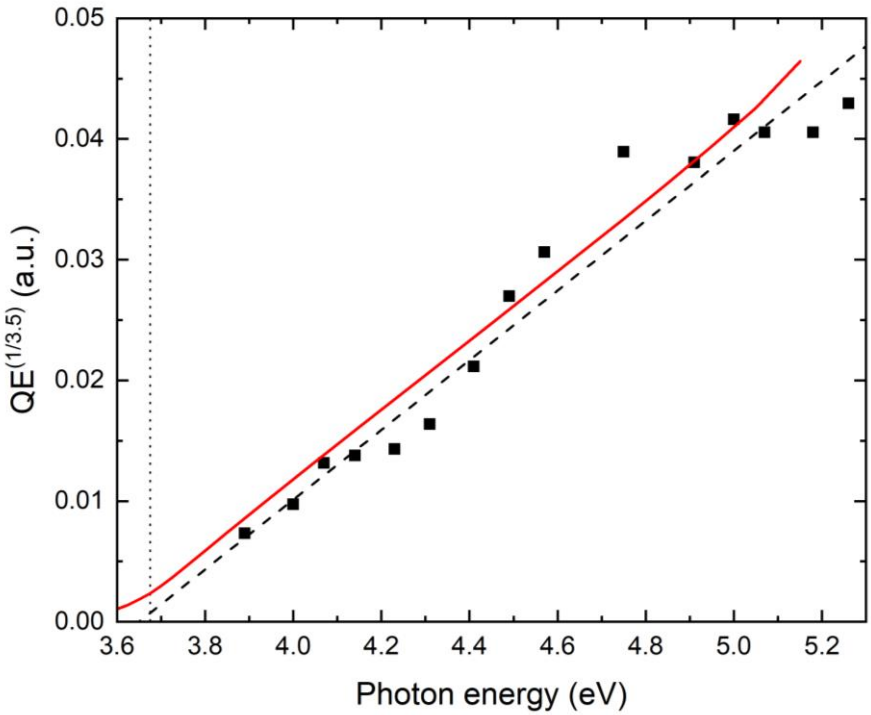

Figure 5.6: Quantum efficiency (QE) per absorbed photon of Mo (001) to the power (1/3.5) as a function of incident UV photon energy (ħω): Experimental measurements (data points) and linearly scaled fit of the simulated QE for Mo (001) emission (solid red line). Linear fit (dashed black line) used to extract the 3.675eV work function (vertical dotted line).

The method employed by Gobeli and Allen[51], which assumes that the QE is proportional to $(\Delta E)^n$ for small ΔE that is significantly greater than $k_B T_e$ (to avoid Boltzmann tail emission effects), is again used to determine the work function for Mo(001) photocathode from the spectral QE measurements. As shown in figure 5.6, a value of n = 3.5(±0.05) generates a linear dependence for $(QE)^{1/n}$ as a function of the incident photon energy ħω (dashed line), especially for low ΔE values, that allows a value of $\phi_{Mo(001)}$ = 3.675±0.05 eV to be extracted. This ΔE power-law scaling is also in agreement with the theoretical spectral dependence of the total scaled QE evaluated from the four emitting bands using the one-step photoemission simulation (solid red line). As for Rh(110) in chapter 4, the total summed QE evaluated from the photoemission model is scaled linearly to fit the experimental data as the transition matrix elements are not included in the analysis. I note that in this case the theoretical

QE prediction is overall somewhat greater than the spectral dependence of the QE measurements, but there is still good consistency between experiment and theory. Most importantly, like Rh(110), the QE clearly does not follow the Fowler-DuBridge[32] quadratic scaling of the QE with excess photoemission energy; that is, QE $=A.(\Delta E)^2$, where A is a constant again a direct result of the inclusion of bulk band and vacuum states in our photoemission analysis

The ~1eV discrepancy between the experimental value for $\phi_{Mo(001)}$ and the DFT evaluated value for a clean Mo(001) surface is also again likely due to the dipole induced by a surface oxide layer. Molybdenum is known to react with oxygen, forming a 1(±0.5) monolayer of MoO_2 [97] on the at room temperature. The potential difference due to such a Mo surface oxide layer has been measured to be as large as ~1.7 eV[98] at 25 °C – an indication that the work function discrepancy is due to an oxide layer.

For completeness, in Figure 5.7 I show the spectral dependence of the absolute QE for Mo(001) expressed as emitted electrons per absorbed photon using the 59-74% surface reflectivity[99] evaluated from the known complex refractive index Mo over the measured 236-288nm spectral range for 60° incident angle and for the p-polarized UV light. The measured QE (data points) increases from ~10^{-9} electrons/photons (the detection limit for the measurement) at $\hbar\omega$ = 3.89eV to 2.9 $\times 10^{-6}$ electrons/photon at $\hbar\omega$ = 5.26eV where ΔE >>1eV. The solid red line in figure 5.7 displays the same total four-band QE predicted from the one-step photoemission simulation shown in figure 5.4. The photoemission simulation indicates that Band 3 dominates the QE for ΔE greater than ~0.3eV due to the larger local density of occupied states that result primarily from its large transverse effective mass m_T

(Table II). There are also no resonant photoemission processes evident in the QE measurements. This is consistent with the DFT evaluated band structure (figure 5.4) which indicates that resonant one-photon transitions from occupied states below the Fermi energy to unoccupied bands above the vacuum level are not possible for emission in the Γ - H direction. Moreover, no two-photon photoemission was observed in the measurements which is consistent with the less than ~100kW/cm^2 incident UV pulse intensities used in the experiments.

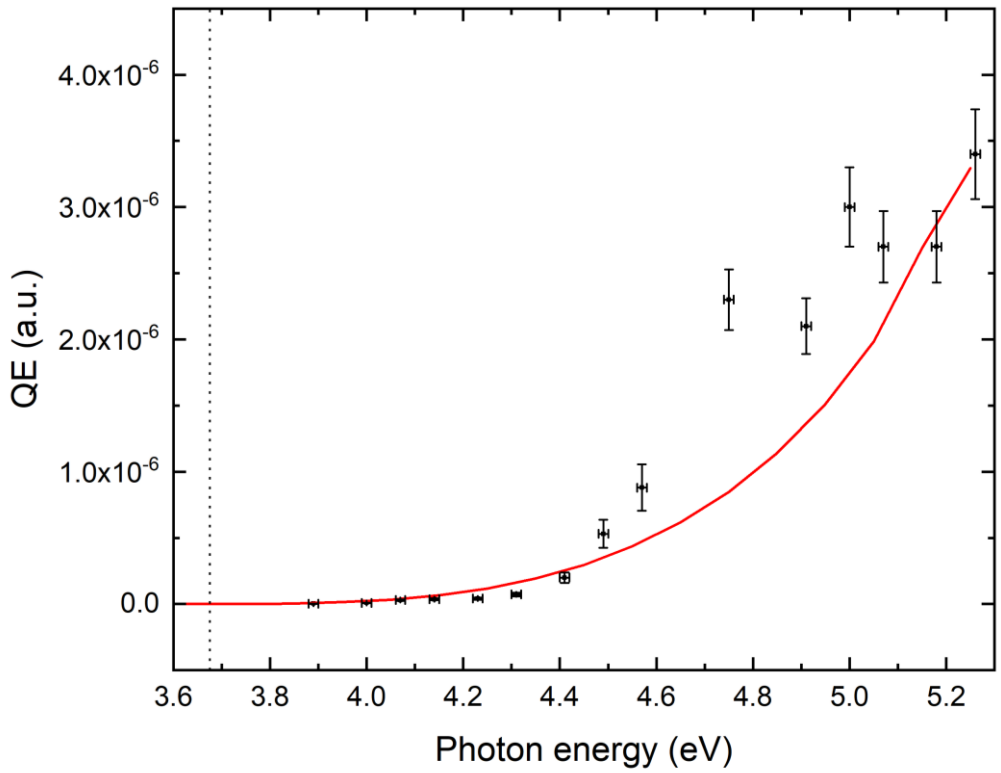

Figure 5.7: Quantum efficiency (QE) per absorbed photon of Mo(001) as a function of incident UV photon energy (ħω): Experimental measurements (data points) and linearly-scaled fit of the simulated QE for Mo(001) emission (solid red line).

5.1.3 Mean transverse energy- Mo(001)

The spectral MTE measurements for the Mo(001) photocathode, obtained using the solenoid scan technique and the 3.0-5.3eV tunable UV radiation source, also display features that are inconsistent with prior photoemission analyses. In figure 5.8, I contrast the obtained experimental MTE data with the formulation of Dowell and Schmerge[18] for which MTE = $\Delta E/3$ (dashed black line), and the more recent expression derived by Vecchione et al.[19] (solid black line) (equation 2.6). Although the Dowell-Schmerge theory and the Vecchione theory agree with the experimental data for $\Delta E < 0.8$eV ($\hbar\omega < 4.5$eV), the measured MTE values are less than predicted by these prior theories at higher photon energies. This is likely a fundamental effect caused by the band structure of Mo; specifically, the fact that the three electron-like bands emitting in the (001) crystal direction have minima 1.5 – 1.7eV below the Fermi energy (see figure 5.4 and Table II). The one-step photoemission simulations shown in section 2.5.2 of chapter 2 indicate that the MTE becomes constant for such bands when the photon energy exceeds the difference between the Fermi energy and the energy of the bottom of the band. For the case of Mo(001), the three bands all have different E_0, m_z, and m_T values (Table II) which will tend to smooth out the strong MTE variations displayed in figure 2.6.

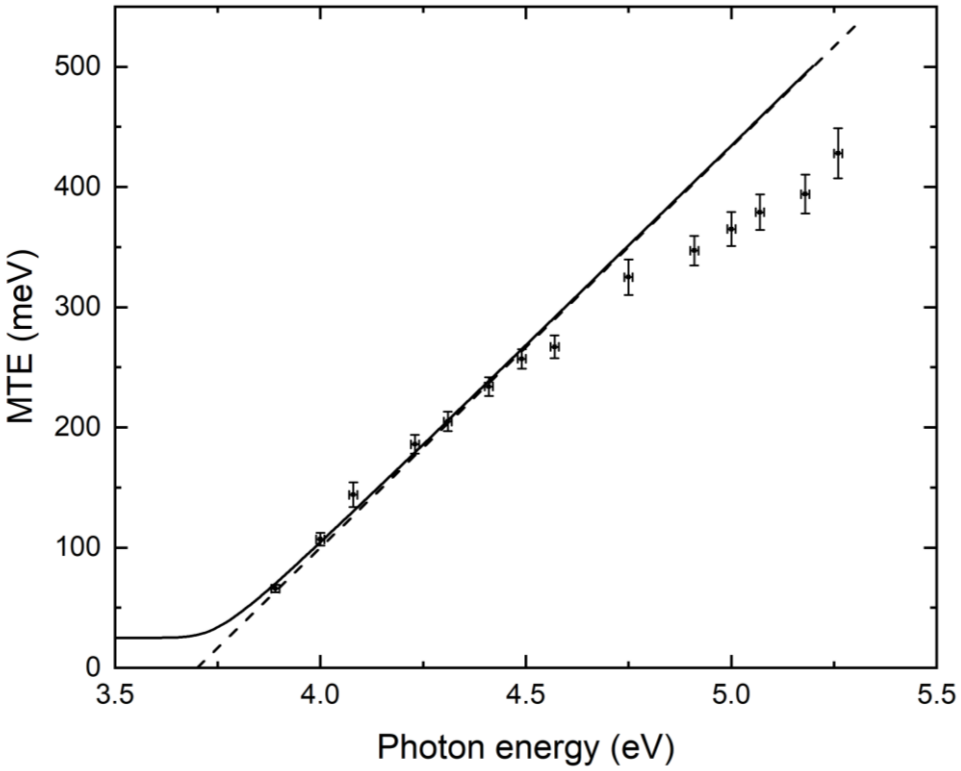

Figure 5.8: Mean transverse energy of emitted electrons from Mo(001) and a function of incident UV photon energy (ħω): Experimental solenoid scan data with error bars (data points); MTE calculated using Vecchione theory using E_f=7.37 eV[100] (equation 2.6) (solid black line); MTE calculated using Dowell theory (MTE = $\Delta E/3$) (dashed black line).

The results of the full one-step photoemission simulation of the MTE for the Mo(001) photocathode using the cylindrical parabolic band dispersion parameters listed in Table II are shown in figure 5.9 together with the experimental measurements (data points). The dashed black line, blue solid line, dashed dot line, and solid black line show the MTE predicted by the one-step simulation for the emission Bands 1, 2, 3, and 4 respectively. The simulated relative QE from each band as a function of excess photoemission energy is then used as a weighting to evaluate the theoretically expected MTE from Mo (001) as a function of incident photon energy; that is, the emission from each band is assumed to be independent. Not surprisingly, the emission from Band 3 generates the largest MTE since it has the largest transverse effective mass $m_T = 1.67m_0$ (Table I), whereas the other three bands with comparable values of m_T have significantly lower MTEs of electron emission. As Band 3 also approximately has the same

QE of emission as the other three bands combined, the total simulated MTE of emission (solid red line) lands roughly halfway between the two.

The spectral dependence of the four-band MTE calculated using the one-step photoemission analysis in the cylindrical band dispersion approximation is not quite in agreement with the experimental data – its predicted MTE value is about 30-50meV too low. This discrepancy is likely due to the fact that the transverse dispersion of the four emission bands are not well described by a simple parabolic form, as shown in figures 5.5. Indeed, the transverse dispersion of Band 3, which clearly greatly influences the MTE of the Mo(001) photocathode, is known to be highly energy dependent. A more sophisticated analysis technique that takes into account such non-parabolic dispersion may produce better agreement, but they will likely first need to be tested on photocathode materials that do not have multi-band emission like Mo(001).

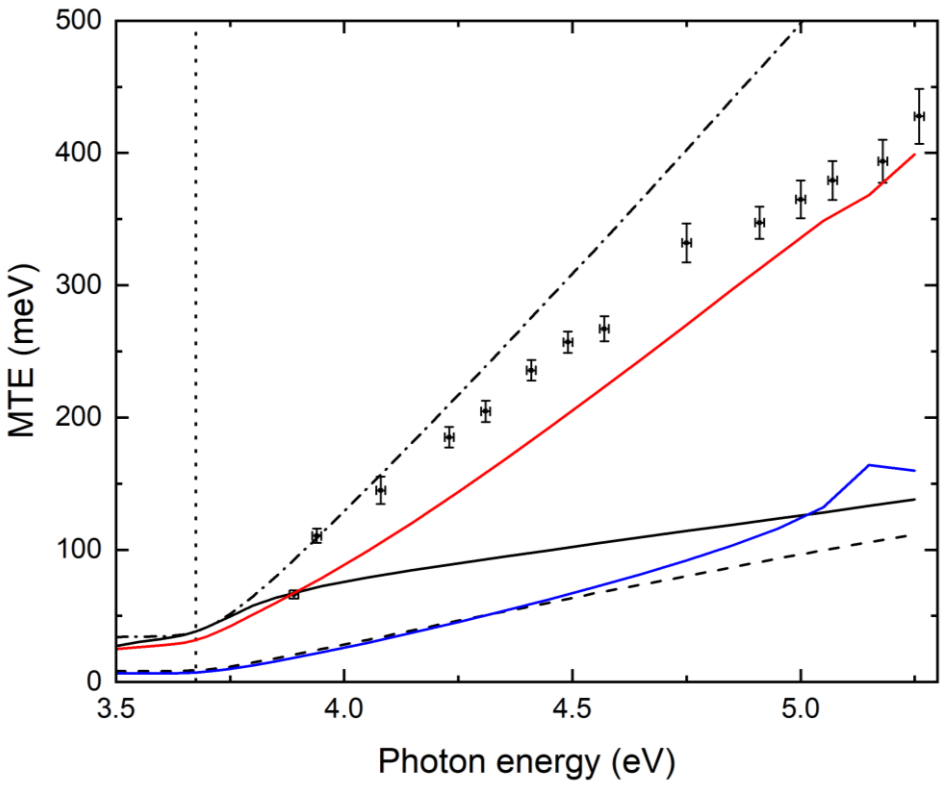

Figure 5.9: Mean transverse energy of emitted electrons from Mo(001) as a function of incident UV photon energy (ħω): Experimental solenoid scan measurements (data points); theoretical MTE evaluated from the one-step photoemission simulation for Band 1 (dashed line), Band 2 (blue solid line) Band 3 (dashed dot line) and Band 4 (black solid line); total simulated MTE for Mo(001) emission (solid red line). The vertical dotted line indicates the measured 3.7eV work function.

5.2 Tungsten

5.2.1 W Band structure

Figure 5.10 shows the band structure for W calculated using DFT with full relativistic effects and spin-orbit coupling. The W band structure is evaluated along the k-path $\Gamma \xrightarrow{\Delta} \mathrm{H} \xrightarrow{G} \mathrm{N} \xrightarrow{\Sigma} \Gamma \xrightarrow{\Lambda} \mathrm{P} \xrightarrow{\mathrm{F}} \mathrm{H}$ in the first Brillouin zone, where Δ, G, Σ, Λ, and F are symmetry lines and their lengths are $\overline{\Gamma\mathrm{N}} = \sqrt{2}\pi/a$, $\overline{\Gamma\mathrm{P}} = \sqrt{3}\pi/a$, and $\overline{\Gamma\mathrm{H}} = 2\pi/a$ for the bcc lattice constant a. For convenience, the Fermi level depicted by the horizontal line is set to zero energy. For my DFT

calculation of the bulk W crystal, the electronic wave function is described by a plane-wave basis set with an energy cut-off of 70 Ry, and the energy cut-off for the charge density is set to 400 Ry. A threshold of 10^{-6} Ry for the ground state energy is used, and a sampling of 200 Monkhorst-Pack special *k*-points along the primary crystallographic directions[57] and a Marzari-Vanderbilt smearing[64] with a broadening of 0.07 Ry is employed. The resulting DFT calculated body-centered cubic crystal structure for W has a lattice constant a = 3.2348 Å, which is within 2% of the experimental value[100].

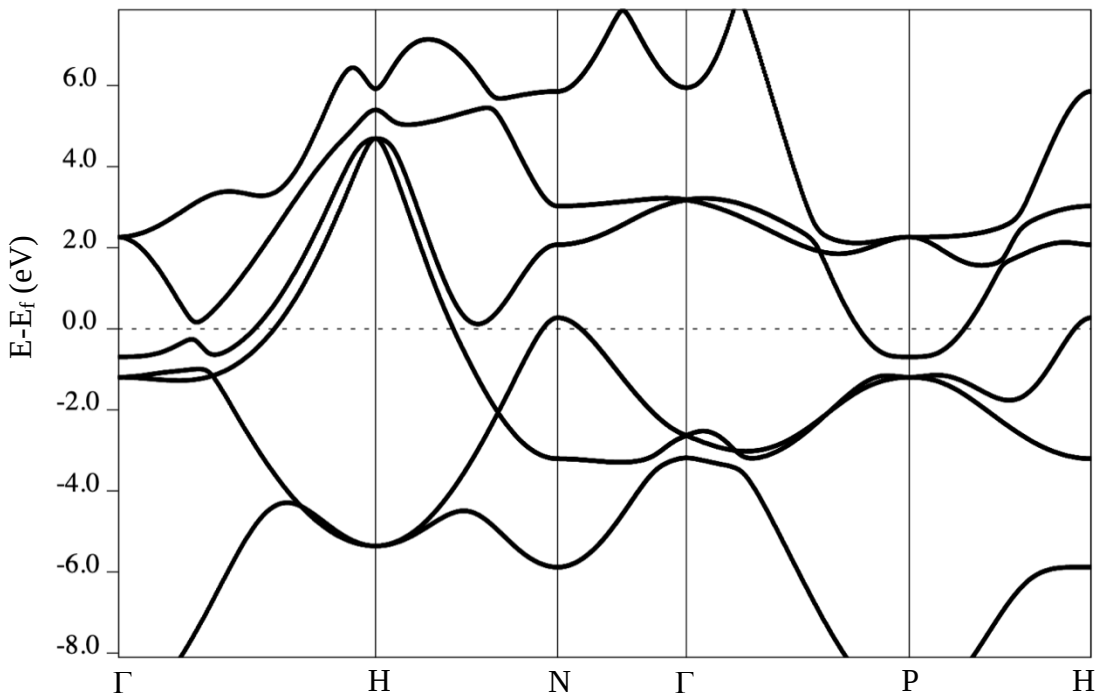

Figure 5.10: W band structure along high symmetry points. The horizontal line at 0 eV represents the Fermi level. Γ→ H (001), Γ→P (111), Γ→N (110) represent directions.

The Fermi surface for W calculated using a plane-wave basis set with 15×15×15 uniform k-grid points sampling the irreducible Brillouin-zone is shown in figure 5.11. The Γ − H photoemission direction for W(001) is marked on the Brillouin zone using an arrow along the Δ-symmetry line. The 'lens' feature present in the Mo band structure (figure 5.3) is not present for W as stronger relativistic / spin-orbit coupling effects generate a larger band

splitting forcing the minimum of the 'lens' feature above the Fermi level (figure 5.5). My relativistic band structure calculation, which is in good agreement with that of Christensen and Feuerbacher[101], indicates that two bands will contribute to photoemission for excess energies less than about 1.2eV – a simplification from Mo(001) due to the increased relativistic / spin-orbit coupling effects for the higher *Z* Tungsten atom.

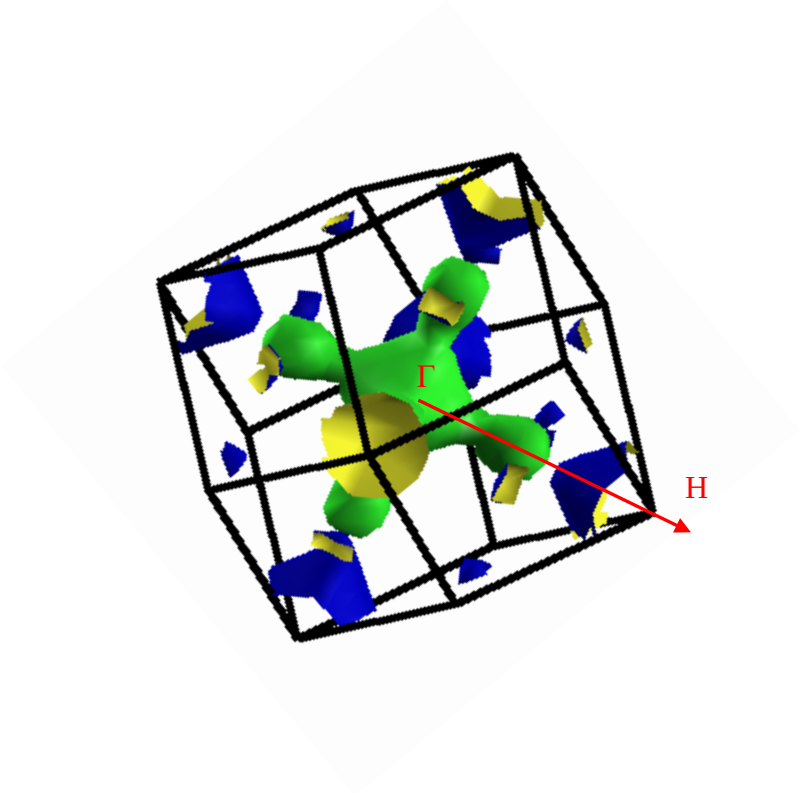

Figure 5.11: W Fermi surface calculated using DFT. The arrow indicates the $\Gamma - H$ direction in the first Brillouin zone. The figure clearly visualizes the "jack", "electron lens" and "octahedron" along the Δ-symmetry line.

Figure 5.12 shows the relevant portions of the band structure of W for photoemission along (001) crystal direction (the $\Gamma - H$ direction in the Brillouin zone) calculated using the DFT evaluated crystal lattice constant. In this case, in order to ensure a reasonable accurate representation of the possible emitting states in the employed cylindrical parabolic band dispersion approximation, I will use three band portions to approximate the W band structure in the longitudinal direction. These are shown by the dashed red lines in figure 5.12(a). The

first band crossing the Fermi level is split into two portions; one, labeled Band 0, from the Γ point to about 0.27 of the Γ - H distance (i.e. to an energy of ~0.5eV below the Fermi energy) and the second, labeled Band 1, from 0.37 of the Γ - H distance to just above the Fermi level. The second band crossing the Fermi level, labeled Band 2, is fit in the same manner as Band 4 for Mo(001) (figure 5.4) – it is, of course, the same band. All three band portions are electron-like in this longitudinal emission direction.

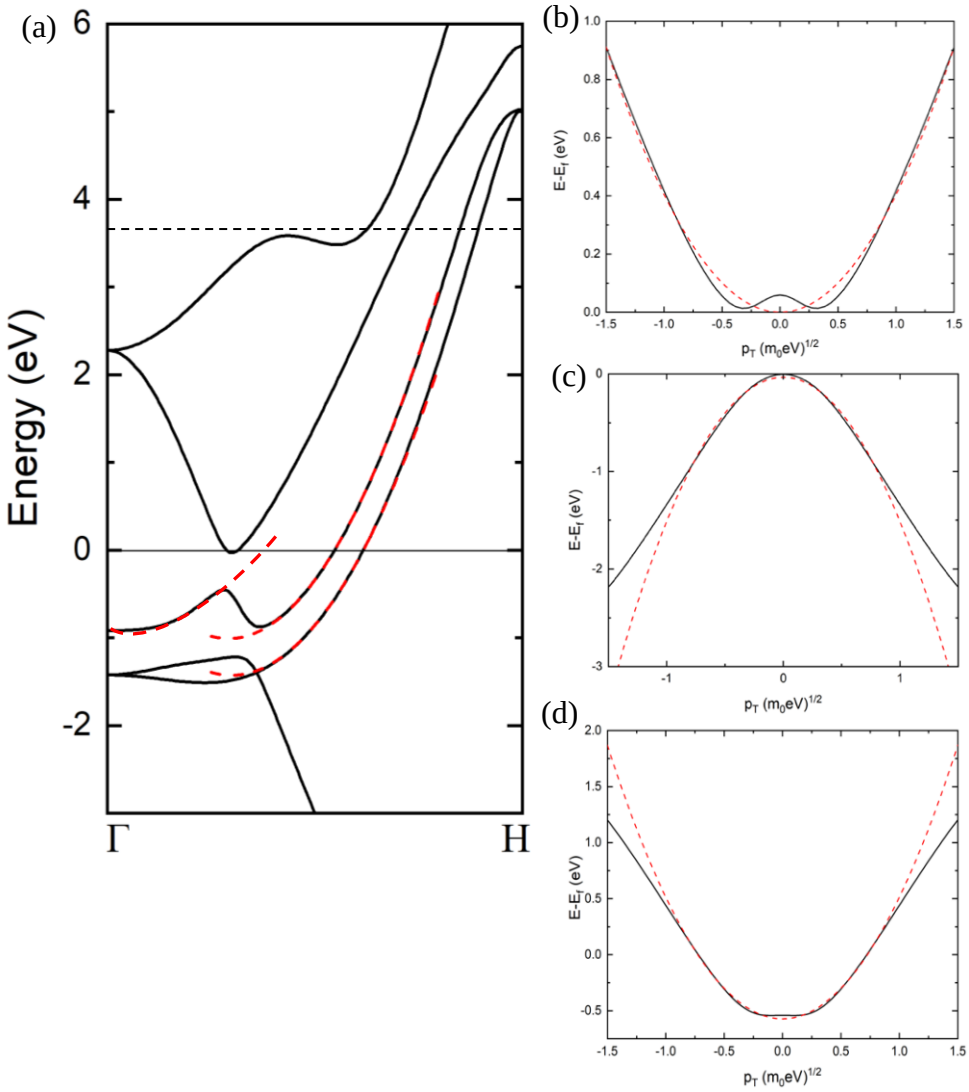

Figure 5.12: (a) Band structure of W along the Γ − *H* direction with the Fermi energy set to zero and the vacuum level associated with the measured 3.78eV work function (dashed line). The band structure includes parabolic dispersion fits (red dashed lines) to the emitting Bands 1 and 2, that cross Fermi level and Band 0 below the Fermi level. (b)-(d) Band structure for W along transverse direction for Bands 1, 2 and 0 respectively. The red dashed lines indicate the parabolic fits used in effective mass calculation along transverse direction near the Fermi level for Band 0 at 0.27 of the Γ - H distance (near the first maximum of the band).

The corresponding transverse fits to the three bands are shown in figure 5.12(b-d); for Bands 1 and 2 in the vicinity of the Fermi level and for Band 0 at about 0.27 of the Γ - H distance (near the first maximum of the band). In this case, the transverse dispersions are somewhat better approximated by parabolic dispersions (dashed red lines) than was the case for Mo (figure 5.5), mainly because the larger relativistic / spin-orbit coupling effects in W ensure that the bands are further apart energetically and so do not influence each other as strongly. The longitudinal and transverse band parameters m_z, m_T, p_0, and E_0 extracted for the three emitting band portions in the cylindrical parabolic dispersion approximation are listed in Table III using units of electron volts (eV) and the free electron mass m_0. These parameters are employed in the comparison of the experimental measurements of the spectral dependence of the MTE and QE with the one-step photoemission model.

Table III: Parabolic dispersion band parameters – W(001)

	Band 0	Band 1	Band 2
m_z	$1.64m_0$	$1.0m_0$	$1.0m_0$
m_T	$0.59m_0$	$0.91m_0$	$-0.32m_0$
p_0 ($\sqrt{m_0 . eV}$)	0.057	1.65	1.82
E_0 (eV)	-0.8	–0.86	-1.25

5.2.2 Quantum efficiency and work function- W(001)

The work function for a clean W(100) photocathode surface is calculated to be 4.6(±0.2)eV using the thin-slab technique. For this evaluation, I used a 0.05 Ry Gaussian-spreading, fully relativistic pseudopotentials, and n×n×1 Monkhurst-Pack[57] k points to

ensure that the DFT-based calculation converged to within 0.2eV. The obtained value for $\phi_{W(001)}$ is within the range of the accepted value of 4.70(±0.21)eV for W(001)[41].

As for Rh(110) and Mo(001), the method employed by Gobeli and Allen[51], which assumes QE = $A.(\Delta E)^n$ with A constant, is used to determine the work function for the W(001) photocathode from the spectral dependence of the QE well above the work function. In this case, the one-step photoemission simulation predicts a ΔE power-law scaling with an exponent of around 3.0 as a result of the inclusion of bulk band and vacuum states in the analysis. However, as shown in figure 5.13, a plot of the cubic root of the theoretical QE against the incident photon energy $\hbar\omega$ does not generate a clear linear dependence. This is due to the onset of emission from Band 0 when ΔE exceeds ~0.5eV. Nonetheless, the scaled QE obtained from the one-step photoemission model is a very good fit to the experimental QE data which is expressed as emitted electrons per absorbed photon using the 51-61% surface reflectivity[99] evaluated from the known complex refractive index W over the measured 236-288nm spectral range for 60° incident angle and the p-polarized UV light. The only outlier is the data point at 4.75eV (the fourth harmonic of the Yb:KGW laser system[25]) which may be the result of measurement error or laser power fluctuations. An approximate linear fit through the lower photon energy data points (dashed line in figure 5.12) allows a value of 3.78±0.05 eV for the work function of W(001) to be determined. This value is ~0.82eV below the extracted thin-slab value of ~4.6eV. The discrepancy is again likely due to a 1 (±0.5) monolayer WO_2 oxide layer on the photocathode surface at room temperature [97] a potential difference due to the tungsten surface oxide layer is estimated to be around 1.6-1.9 eV at 25 °C [98].

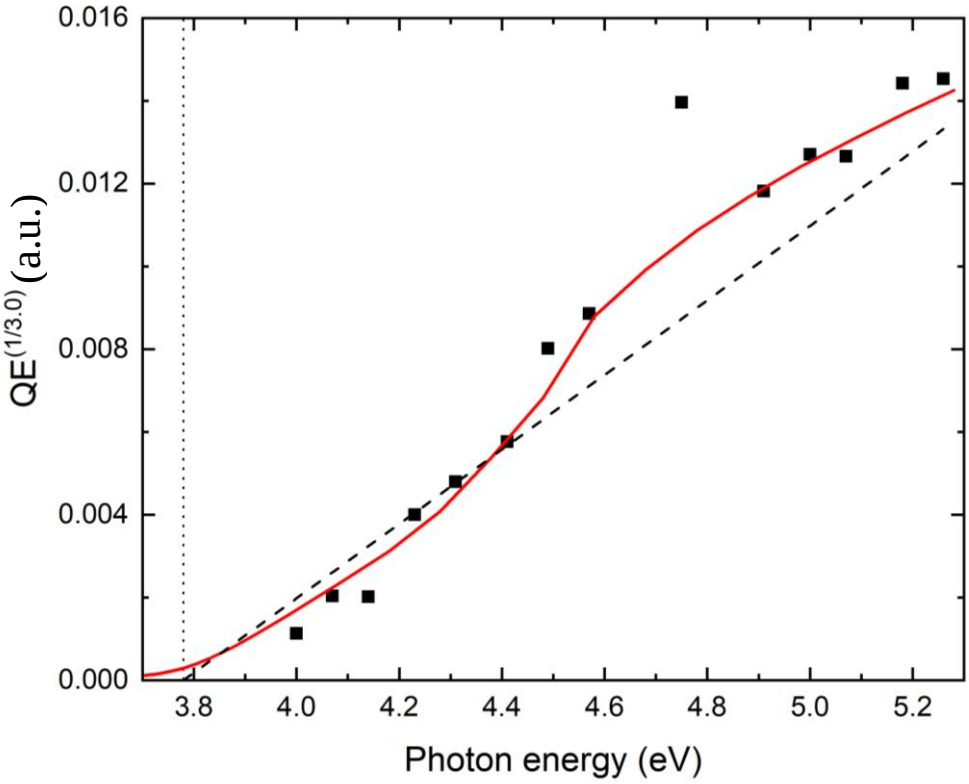

Figure 5.13: Quantum efficiency (QE) per absorbed photon of W (001) to the power (1/3) as a function of incident UV photon energy (ħω): Experimental measurements (data points) and linear fit (dashed black line) used to extract the 3.78 eV work function (vertical dotted line). The red solid line indicates the theoretical simulation calculated QE values.

Figure 5.14 shows the spectral dependence of the measured absolute QE for W(001) expressed as emitted electrons per absorbed photon (data points) and the equivalent theoretical dependence from the one-step simulation (red line) scaled as in figure 5.13. The QE increases from ~10^{-9} electrons/photons (the detection limit for the measurement) at ħω = 4.00 eV to 3.7 $\times 10^{-6}$ electrons/photon at ħω = 5.26 eV where ΔE ~ 1.45eV. The good agreement between the experiment and theory in the spectral trend of the QE is a strong indication that emission from W(001) is a one-step process. Indeed, the band structure in the Γ - H emission direction (figure 5.12) indicates that there is little likelihood of resonant one-photon photoemission processes and two-photon photoemission is equally as unlikely due to the low (<100kWcm^{-2}) laser intensities employed in the measurements.

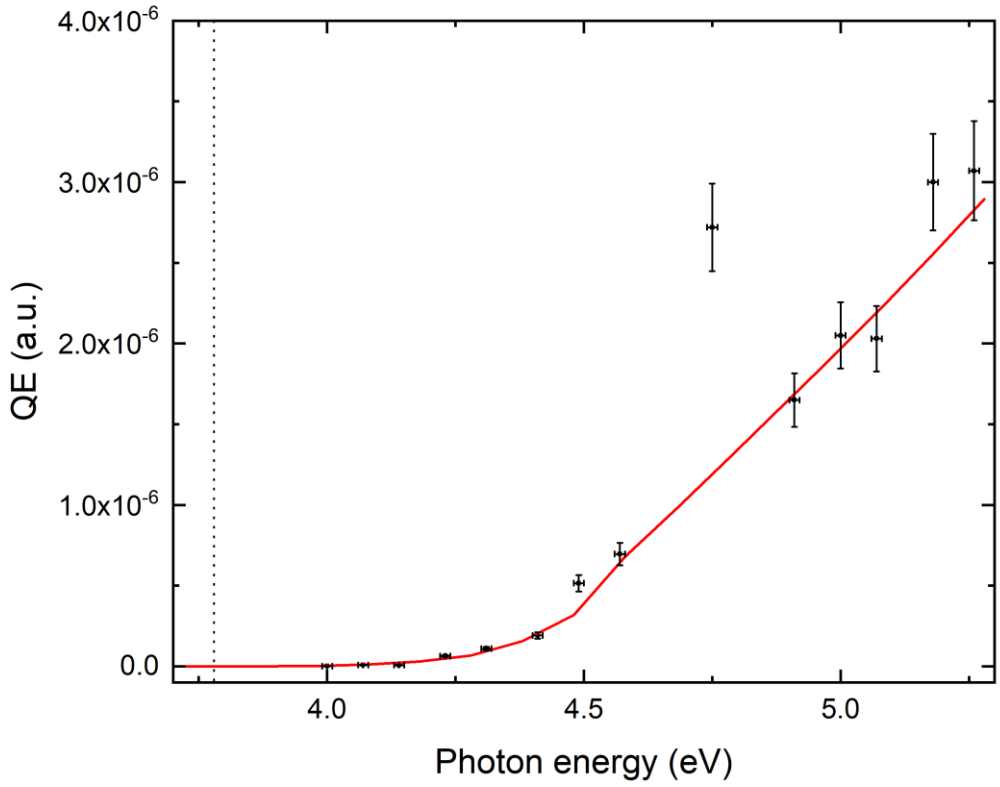

Figure 5.14: Quantum efficiency (QE) per absorbed photon of W(001) as a function of incident UV photon energy (ħω): Experimental measurements (data points) and linearly-scaled fit of the simulated QE for W(001) emission (solid red line).

5.2.3 Mean transverse energy- W(001)

Despite the clear observation above that the QE does not follow the Fowler-DuBridge[32] quadratic scaling of the QE with excess photoemission energy, the spectral MTE measurements for the W(001) photocathode, obtained using the solenoid scan technique and the 3.0-5.3eV tunable UV radiation source, display features that are more consistent with prior photoemission analyses. In figure 5.15, I compare the obtained experimental MTE data with the formulation of Dowell and Schmerge[18] for which MTE = ΔE/3 (dashed black line), and the more recent expression derived by Vecchione et al.[19] (solid black line) (equation 2.6).

Below an excess energy of ~1.0 eV, the prior theories are agreeing quite well with our experimental data. This is in large part due to the fact that Band 1 with its larger density of states dominates the photoemission in the (001) crystal direction and its transverse effective mass m_T is close to the free electron mass m_0 (Table III). Nonetheless, as for Mo(001), there is a suppression of the rate of increase of the MTE at higher excess energies which is again due primarily to the minima in the electron-like Bands 0 and 1 around 0.8-0.9eV (Figure 5.12).

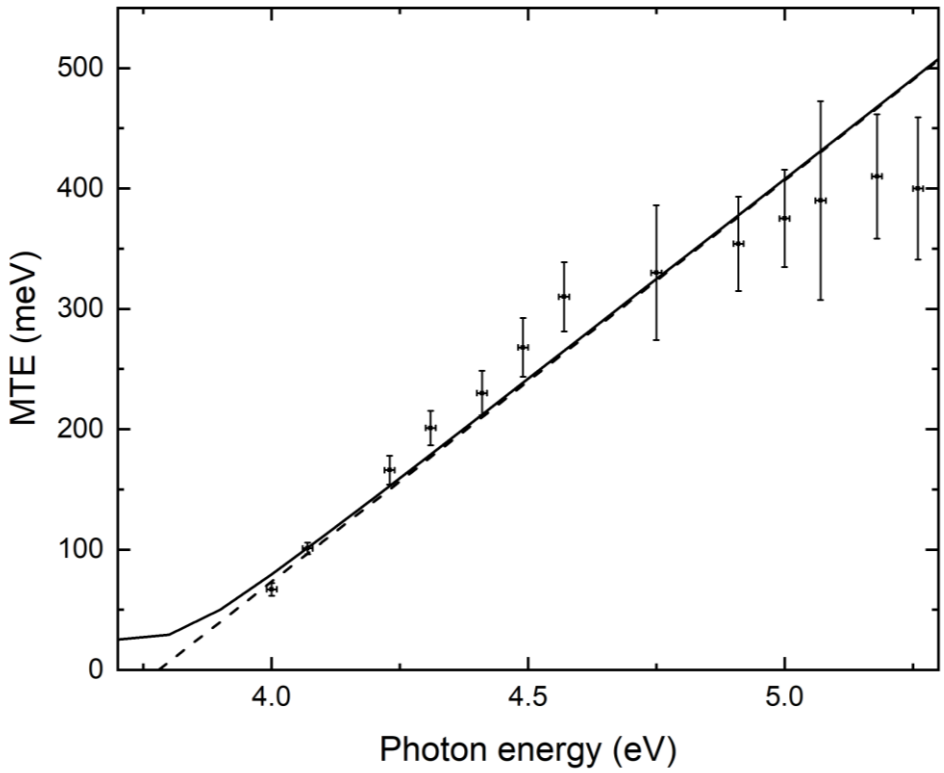

Figure 5.15: Mean transverse energy of emitted electrons from W(001) as a function of incident UV photon energy (ħω): Experimental solenoid scan data with error bars (data points); MTE calculated using Vecchione theory using E_f=7.45 eV[100] (equation 2.6) (solid black line); MTE calculated using Dowell theory (MTE = $\Delta E/3$) (dashed black line).

In Figure 5.16: Mean transverse energy of emitted electrons from W(001) as a function of incident UV photon energy (ħω): Experimental solenoid scan measurements (data points); theoretical MTE evaluated from the one-step photoemission simulation for Band 1 (solid black line) and Band 2 (black dot-dashed line) and Band 0 (black dot-dot-dashed line); total simulated

MTE for W(001) emission (solid red line). The vertical dotted line indicates the measured 3.78eV work function., I display the spectral dependence of the MTE predicted by the one-step photoemission model, using the extracted value of 3.78eV for the work function (Figure 5.13), shown in Figure 5.16 together with the experimental measurements (data points). The solid black and double-dot dashed black lines show the MTE of electron emission predicted by the one-step simulation for Bands 1 and 0 respectively, while the lower dot-dashed black line shows the predicted MTE for Band 2. All the emissions are evaluated in the cylindrical parabolic band approximation (i.e. using the parameters in Table III) for states from the band minimum at $p_z = p_0$ to about $20k_bT_e$ above the Fermi level to ensure all photo-emitted electrons in the Boltzmann tail of the distribution are counted. The exception is Band 0 where the evaluation is from $p_z = p_0$ to $p_z = 1.128\ (m_0eV)^{1/2}$ which corresponds to a point about 0.45eV below the Fermi level just before the small energy maximum (Figure 5.12). The part of the band just after the energy maximum has a negative gradient, implying that the group velocity dE/dp_z is negative in the direction of emission, meaning that electrons from these states likely have a significantly reduced photoemission efficiency. The simulated relative QE from each band as a function of excess photoemission energy is then used as a weighting to evaluate the theoretically expected MTE from W(001) as a function of incident photon energy; that is, the emission from each band is assumed to be independent. The predicted MTE by the one-step parabolic band photoemission simulation is shown by the solid red line in Figure 5.16, which is clearly in very good agreement with the experimental data for excess energies less than ~1.0 eV ($\hbar\omega < 4.8$ eV).

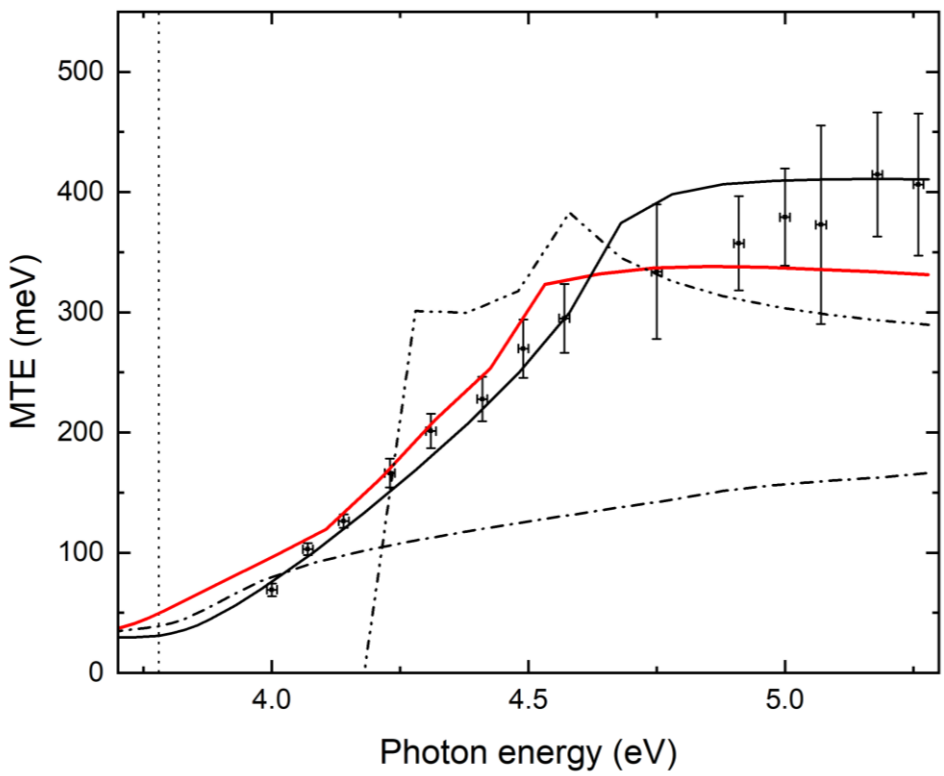

Figure 5.16: Mean transverse energy of emitted electrons from W(001) as a function of incident UV photon energy (ħω): Experimental solenoid scan measurements (data points); theoretical MTE evaluated from the one-step photoemission simulation for Band 1 (solid black line) and Band 2 (black dot-dashed line) and Band 0 (black dot-dot-dashed line); total simulated MTE for W(001) emission (solid red line). The vertical dotted line indicates the measured 3.78eV work function.

For excess energies higher than 1.0 eV (ħω > 4.8eV), the one-step photoemission simulation also clearly captures the observed suppression of the linear trend of the MTE with ΔE. This is to be expected since Bands 0 and 1, with their minima 0.8-0.9eV below the Fermi level, dominate the photoemission due to the fact that their combined density of states is at least an order of magnitude larger than that of Band 2 which has a significantly lower transverse effective mass. As a result, and in agreement with the one-step photoemission simulations shown in section 2.5.2 of chapter 2, the MTE trend with excess photoemission energy is flattened. The theoretically predicted MTE suppression is however somewhat stronger than that measured. This is likely due to the fact that a transverse parabolic dispersion is not a

perfect fit for the emitting bands (Figure 5.12). Nonetheless, the agreement between the simulation and the experiment is quite respectable.

Although the one-step photoemission simulation employing the cylindrical parabolic band approximation is in better agreement with experiment for W(001) than Mo(001), it is clear that better representations for the E(**p**) band dispersions are needed. In chapters 6 and 7, I will introduce an alternative analytical fit function to describe the emitting band dispersions. I also note that for completeness I have included in appendix C the measured spectral dependence of the MTE and QE for other bcc single-crystal metal photocathodes (W(111) and Ta(001)) for which a full analysis using the one-step photoemission simulation has not been completed.

CHAPTER 6

Hf(0001)/HfO_2 PHOTOCATHODE

In this chapter, I will present a spectral analysis of the photoemission characteristics of a single-crystal Hafnium (Hf) photocathode oriented for photoemission perpendicular to the basal plane of its hexagonal close-packed (hcp) crystal structure. *Ab initio* density functional theory (DFT) calculations indicate that Hf(0001) should be a low emittance [102] photocathode material due to the low transverse effective mass of the emitting electronic band restricting the transverse momentum of the photo-emitted electrons [103] and thereby their MTE. This expectation is borne out by my experimental studies which indicate an asymptotic linear dependence of the MTE on the excess photoemission energy ΔE that is significantly lower than the $\Delta E/3$ trend predicted by Dowell and Schmerge [11,18,27] provided that oxide layer native to Hf is removed. In the presence of the Hafnia surface layer, the Hf(0001)/HfO_2 photocathode also exhibits emission from known defect states (mainly oxygen vacancies [104,105]) in the ~10Å oxide layer. The spectral dependences of the MTE due to electron emission from both the bulk metal band states and the oxide defect states are consistent with a one-step photoemission simulation that includes the physical properties (density of states and dispersion) of both the emitting and vacuum recipient states [20,25]. For the oxygen vacancy defect states in HfO_2, the local density of the emitting bulk band states employed for the single-crystal Rh(110) (chapter 4), Mo(001) and W(001) (chapter 5) metal photocathodes is replaced in the one-step photoemission simulation by the momentum-space probability density of hydrogen-like 1*s* electronic states used to model the defect states, as detailed in the Appendix D.

6.1 Ab initio calculations for Hf

6.1.1 Band structure

As was the case for Rh (chapter 4) and Mo and W (chapter 5), the DFT evaluations for Hf again include full relativistic effects, with spin-orbit coupling incorporated during the plane wave self-consistency iterations; that is to say, a fully relativistic pseudopotential within the generalized gradient approximation (GGA) [63] is employed. For the DFT calculation of the bulk Hf crystal, the electronic wave function is described by a plane-wave basis set with an energy cut-off of 55 Ry, and the energy cut-off for the charge density is set to 400 Ry. A threshold of 10^{-2} Ry for the ground state energy is used, and a sampling of 200 Monkhorst-Pack special *k*-points along the primary crystallographic directions [57] and a Marzari-Vanderbilt smearing [64] with a broadening of 0.01 Ry is employed. The resulting DFT evaluated hexagonal crystal structure for Hf (at effectively 0K) has lattice constants a = 3.1452 Å, and c = 5.075 Å, which is within 2% of the measured value at 300 K [106,107]. Figure 6.1 shows the relevant portions of the band structure of Hf for photoemission in the (0001) crystal direction ($\Gamma - A$) and perpendicular directions ($\Gamma - K$ and $\Gamma - M$) calculated using the DFT evaluated crystal parameters. For convenience, the Fermi level depicted by the horizontal line is set to zero energy.

6.1.2 Work function of Hf(0001)

The work function for clean Hf(0001) photocathode surface was evaluated using the thin-slab technique [11,68] in which the (0001) crystal surface is simulated with 0.01 Ry Gaussian spreading and fully relativistic pseudopotentials [63]. To ensure sufficient accuracy

in the calculation, the vacuum thickness is enlarged from 10 to 20 Å and the (1×1) supercell thickness (*n*) is increased from 6 to 10 atomic layers together with the *n*×*n*×1 Monkhurst-Pack points [57] so that the work function value converges to within ±50 meV. The value of $\phi_{Hf(0001)}$ = 4.36(±0.05) eV extracted from this calculation, which is indicated by the dashed horizontal line in Figs. 6.1(a) and (b), is consistent with our prior evaluated value of 4.51(±0.21) eV for Hf(0001).

6.1.3 Emission band characteristics

The first step in a first-principles analysis of photoemission from crystalline photocathodes within the one-step model [16] is the identification and characterization of the occupied states below the Fermi level from which photo-emitted electrons can originate [11]. Prior DFT calculations of the band structure of Hf [107,108] have indicated that the primary electron source for one-step bulk photoemission from this hcp metal will be from a low effective mass hole-like band that crosses the Fermi level and is centered at the Γ point of the Brillouin zone. My *Ab initio* band structure calculations of crystalline Hf agrees with this assessment. The band structure evaluation indicates that only one band (the lowest band in Figs. 6.1(a) and (b)) is expected to contribute strongly to photoemission from Hf(0001) for excess photoemission energies ΔE less than ~1 eV. For such ΔE values, this emitting band state centered on the Γ point of the Brillouin zone may be well approximated (in the vicinity of and just below the Fermi level) by a dispersion of the form

$$E(\mathbf{p}) = E_0 + a_Z cos[b_z(p_z - p_0)] + \sum_n c_n p_T^{2n}, \qquad 6.1$$

where p_z and p_T are the longitudinal ($\Gamma - A$) and transverse ($\Gamma - K$ and $\Gamma - M$) momentum directions respectively, and E_0, a_z, b_z, p_0, and the transverse power series coefficients c_n are fitting parameters.

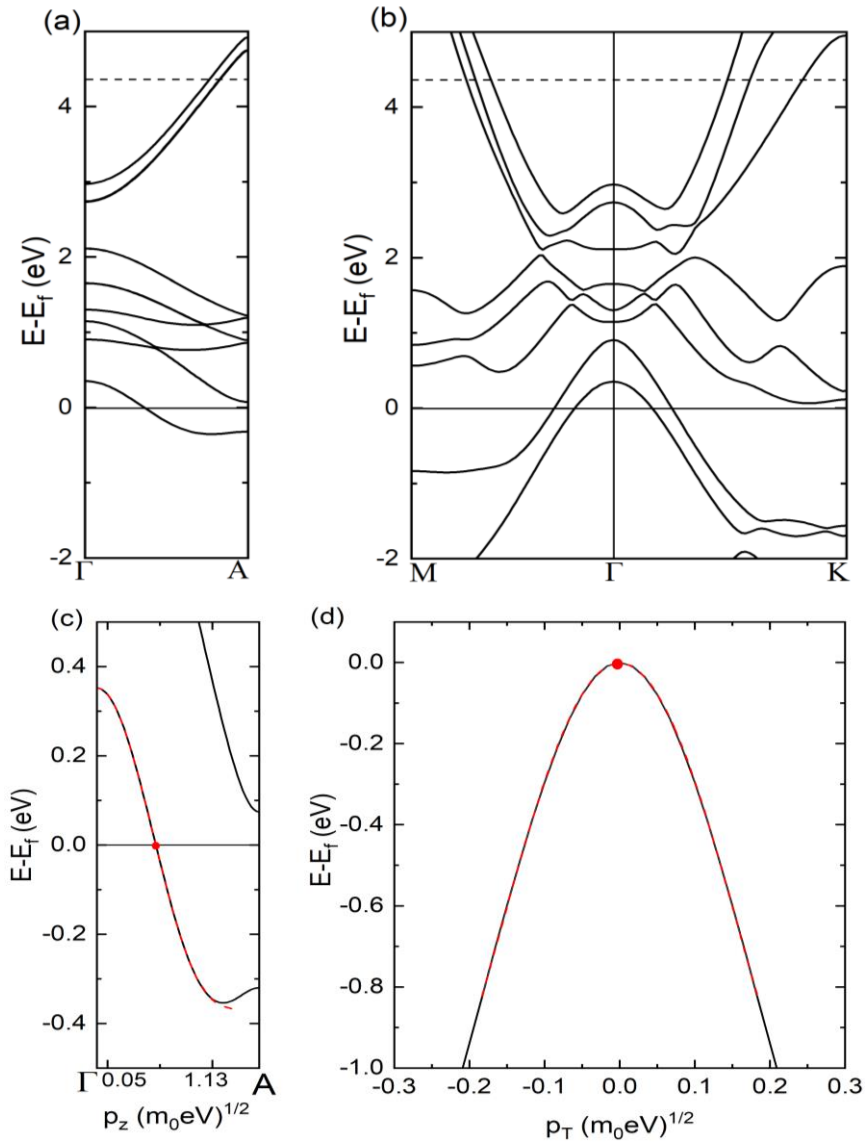

Figure 6.1: The relevant band structure of Hf, evaluated including relativistic effects and spin-orbit coupling, for photoemission in the (0001) crystal direction ($\Gamma - A$) with the Fermi energy set to zero (horizontal line): (a) Overview of the band structure in the reduced zone scheme for the $\Gamma - A$ emission direction and (b) the perpendicular directions ($\Gamma - K$ and $\Gamma - M$) with the *Ab initio* evaluated 4.36 eV work function (i.e. the vacuum level) indicated (horizontal dashed line). (c) The primary $\Gamma - A$ emission band with the employed longitudinal sinusoidal fit shown (dashed red line). (d) Transverse dispersion of the primary emission band at the Fermi level (red dot) in the $\Gamma - A$ direction with the employed $(p_T)^2$ series fit (dashed red line).

In the longitudinal $\Gamma - A$ emission direction with momentum p_z, the sinusoidal fit to the DFT evaluated band dispersion is quite accurate (dashed red line in Figure 6.1(c)) and indicates a longitudinal effective mass for this band in the vicinity of the Γ point of $m_z = -(a_z b_z^2)^{-1} \approx$ $-0.47m_0$. Figure 6.1(d) also shows the good fit (red lines) to the band dispersion in the transverse (Γ – *K* and Γ – *M*) directions with momentum p_T, using a power series up to $n = 3$. The displayed fit originates at the Fermi level at $p_T = 0$ (red dot in Figure 6.1(c) and (d)) and extends to $p_T = 1.4(m_0.eV)^{1/2}$ which, due to the hole-like transverse dispersion, corresponds to a band state that would require an excess photoemission energy of about 2.3 eV for emission – a transverse energy of 1.0 eV plus 1.3 eV to lift the electron to the Fermi level. Around the Fermi level, the first term in the power series fit indicates a transverse effective mass roughly a factor of two less than the free electron mass; that is $m_T = (2c_1)^{-1} \approx -0.46m_0$. The parameters employed for the band dispersion fit of equation (1) are listed in Table IV using units of electron volts (eV) and the free electron mass m_0.

The band structure for Hf displayed in Figure 6.1 indicates that the next highest bulk band, which remains above the Fermi level in the Γ – *A* direction, but also has transverse hole-like dispersion, could contribute to photoemission at excess photoemission energies of greater than about 0.4eV – corresponding to emission from states at the Fermi level and near the *A* point of the Brillouin zone with transverse momenta of greater than $0.8(m_0.eV)^{1/2}$. However, the quantum efficiency of emission from these states is expected to be much less than that of the main emission band that does cross the Fermi level in the Γ – *A* direction (i.e. has emitting states with zero transverse momentum), implying that this next highest bulk band will not contribute significantly to the total MTE or QE of electron emission. This band alignment for Hf is in contrast to that in both hcp Ti and Zr (the other two elements of IUPAC Group 4)

where this second band will contribute to photoemission from (0001)-oriented crystals as it crosses the Fermi level in the Γ – *A* direction [109].

Table IV: Band dispersion parameters for the primary bulk emission band of Hf(0001)

Fit parameter	
E_0	0.0088 eV
a_z	0.3566 eV
b_z	2.444 $(m_0.\text{eV})^{-1/2}$
p_0	–0.0411 $(m_0.\text{eV})^{1/2}$
c_1	–1.078
c_2	0.2655
c_3	–0.03154

Photoemission from the primary bulk electron band state crossing the Fermi level in the Γ – *A* direction is therefore expected to be a one-step process since the evaluated Hf band structure in Figure 6.1 shows that there are no (intermediate) electronic band states 4-5 eV above the Fermi level around the Γ point of the Brillouin zone. Accordingly, in this chapter, the experimental measurements of the spectral dependence of the MTE are compared with the one-step photoemission model outlined in W. A. Schroeder and G. Adhikari, *New J. Phys.* **21**, 033040 (2019), employing the cylindrical band dispersion approximation of equation 6.1 with the parameters listed in Table IV. As discussed in chapter 3, this photoemission simulation includes the local density of states of both the emitting band states and the recipient vacuum states, sets the occupation of the initial band states at an electron temperature T_e = 300 K using the Fermi-Dirac distribution, and employs transverse momentum conservation in the electron emission [10].

6.2 Spectral MTE measurements for Hf(0001)

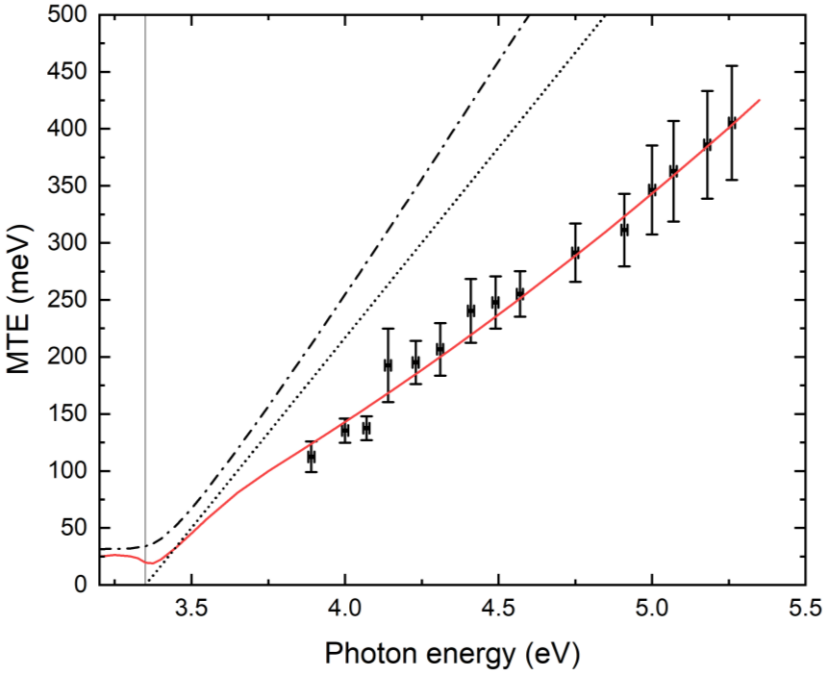

Figure 6.2: Mean transverse energy (MTE) of emitted electrons from polished Hf(0001) as a function of incident photon energy for an effective work function of 3.35 eV (thin vertical line): Experimental solenoid scan measurements (black data points); theoretical MTE evaluated from a one-step photoemission simulation for Hf(0001) at 300 K (red line); MTE = $\Delta E/3$ [18] (dotted line); and the MTE evaluated from a one-step photoemission simulation for an electron-like bulk emission band with $m_T = m_z = m_0$ [20] (dot dashed line).

The spectral dependence of the experimentally extracted MTE for the single-crystal Hf(0001) photocathode polished to remove the surface oxide layer is shown in Figure 6.2. The measured MTE clearly exhibits the increasing linear dependence of the MTE on excess photoemission energy ΔE expected for a bare metal photocathode (black data points), except that the dependence is inconsistent with the $\frac{1}{3}\Delta E$ variation derived by Dowell and Schmerge (dotted line) [18]. Instead, the MTE increases more slowly with excess photoemission energy, approximately as $0.2\Delta E$. This is a direct consequence of the dispersion of the primary bulk emission band (Figure 6.1); specifically, the fact that the magnitude of the transverse effective mass of the hole-like emission band is significantly less than the free electron mass m_0 restricts

the available bulk band states in the transverse momentum direction that may photo-emit for a given excess energy ΔE [9]. In fact, our one-step photoemission model [20] employing the band dispersion parameters listed in Table IV (solid red line in Figure 6.2) closely follows the measured trend of the MTE with ΔE. Thus, this MTE measurement and its theoretical verification provide direct evidence supporting the assertion that a reduction of the transverse effective mass of the bulk emission band below m_0 can result in lower intrinsic emittance (i.e. MTE) photoelectron sources. In this case, the MTE reduction is approximately by a factor of two for incident photon energies above 4.0 eV – the difference, in Figure 6.2, between the solid red line of the Hf(0001) emission simulation and the black dot-dashed line representing one-step photoemission from an electron-like bulk band with $m_T = m_z = m_0$ into the vacuum states [20].

The displayed theoretical fit to the experimental data for the polished Hf(0001) photocathode in Figure 6.2 has only one free parameter, the work function $\phi_{Hf(0001)}$. It suggests $\phi_{Hf(0001)}$ = 3.35 eV (thin vertical line), which is 1 eV lower than our evaluated value of 4.36(±0.05) eV for a clean Hf(0001) surface, indicating that a thin 1-2 ML of oxide is likely to have quickly formed on the photocathode surface after the polishing and prior to being placed under vacuum. It is interesting to note that this reduction due to ML oxide formation is somewhat larger than the ~0.5 eV experienced with main line transition metals (e.g. Mo [97] [98]), but is consistent with the larger difference in electronegativity between Hf and O [110,111] which is expected to result in a larger surface dipole induced reduction in the work function.

The strong band dispersion in the longitudinal direction (associated with a longitudinal effective mass m_z less than m_0) implies that the local density of states of the emitting bulk band for Hf(0001) is relatively low, which results in a reduced QE for the photoemission process.

As a result, MTE measurements could not be performed for photon energies below $\hbar\omega \approx 3.8$ eV where the QE falls below the ~10^{-9} detection limit of our solenoid scan experiment.

6.3 Spectral MTE measurements for Hf(0001)/HfO2

The measured spectral dependence of the MTE for the 'as delivered' (oxidized) Hf(0001)/HfO_2 photocathode (data points in Figure 6.3) is clearly quite different; evidently, the ~10 Å thick surface oxide layer affects the photoemission properties of the single-crystal metal photocathode. In particular, at low photon energies the MTE is relatively constant at 200 meV and only starts increasing for $\hbar\omega > 4.4$ eV – roughly the photon energy at which the MTE from the polished Hf(0001) photocathode also reaches 200 meV (Figure 6.2). This suggests that there are two contributions to photoemission from Hf(0001)/HfO_2; one from the oxide layer dominating at low photon energies and the second from the underlying metal prevailing at high photon energies. Such an interpretation is consistent with the known UV absorption of Hafnia [105], which would allow significant penetration of 3.0-5.3 eV light through a ~10 Å oxide layer to the metal, and the known defect states in HfO_2, mostly oxygen vacancies [104]. The latter reside approximately between 1 and 1.5 eV below the conduction band of Hafnia [104] which has an electron affinity of ~2 eV [112], and so are expected to emit (if even partially populated) for photon energies above their 3 to 3.5 eV effective work function – in agreement with the experimental observations (Figure 6.3).

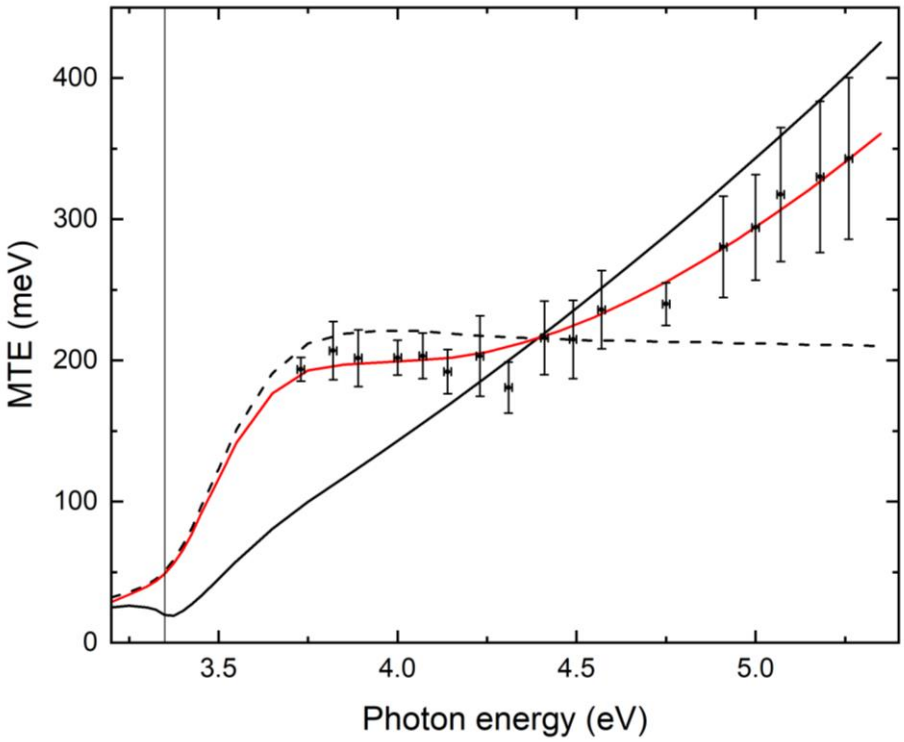

Figure 6.3: Mean transverse energy (MTE) of emitted electrons from the 'as delivered' Hf(0001)/HfO_2 as a function of incident photon energy for an effective work function of 3.35eV (thin vertical line): Experimental solenoid scan measurements (black data points); theoretical MTE evaluated from a one-step photoemission simulation for Hf(0001) at 300K (thin black line from Fig. 6.2); the MTE evaluated for a 1*s* hydrogen-like defect state with a characteristic width $\Delta p = 0.54(m_0.eV)^{1/2}$ (black dashed line); and the theoretical QE-weighted summed MTE for dual metal (Hf(0001)) and oxide layer (HfO_2) photoemission (solid red line).

To illustrate the proposed dual photoemission contributions from a Hf(0001)/HfO_2 photocathode, in Figure 6.3 the theoretical spectral dependence of the MTE for Hf(0001) (thin black line, from Figure 6.2) plotted and that evaluated for a 1*s*-like hydrogenic defect state in HfO_2 (dashed black line), both for the same 3.35 eV work function. The emission model for the defect state, outlined in the Appendix D, is a modification of the existing band-based one-step photoemission simulation that replaces the band states (and their dispersion) by a single state with (i) an energy width of 0.1 eV (half-width e^{-1} maximum) to simulate the known energy distribution of oxygen defect states in HfO_2 [105], (ii) a characteristic momentum width of $\Delta p = 0.54\ (m_0.eV)^{1/2}$ (see Appendix) for the 1*s* state momentum distribution (the modulus square

of the momentum-space wave function), and (iii) a 300 K Fermi-Dirac function centered on the defect state energy (with a Fermi energy at the 3.35 eV work function below the vacuum level) to simulate the population distribution amongst the oxygen vacancy states. As shown by the dashed line in Figure 6.3, these defect state properties generate a relatively constant 215(±5) meV MTE value for the emitted electrons at incident photon energies greater than 3.7 eV (ΔE > 0.35 eV), where the excess photoemission energy is sufficient to emit almost the entire energy-momentum distribution of the 1*s* defect state. More importantly, this choice of parameters for the oxygen vacancy states in HfO_2 is consistent with the observed spectral dependence of the MTE for the Hf(0001)/HfO_2 photocathode when their emission is combined with that from the underlying metal. Specifically, since the two one-step photoemission simulations for emission from the Hf band states and the HfO_2 defect states also provide a relative (but not absolute) QE as a function of the excess energy, a QE-weighted total MTE from the two independent electron emission sources can be constructed:

$$MTE_{total} = \frac{QE_{Hf}MTE_{Hf} + xQE_{HfO_2}MTE_{HfO_2}}{QE_{Hf} + xQE_{HfO_2}}, \qquad 6.2$$

where x is the fraction of emission from the oxide relative to the metal when the QE from both emission sources is set to unity at zero excess energy (i.e. $\Delta E = 0$). The red curve in Figure 6.3 is a fit to the Hf(0001)/HfO_2 photocathode MTE data (black data points) using a constant value of $x = 0.07$ for all incident photon energies. The normalized theoretical quantum efficiencies employed in Equation 6.2 for the metal (QE_{Hf}) and defect states in the oxide (QE_{HfO_2}) are shown on a log-log plot in Figure 6.4 as a function of the excess photoemission energy, ΔE. For ΔE > 0.1eV ($\approx 4k_BT$ where k_B is Boltzmann's constant and T = 300K is the photocathode temperature), the QE of Hf(0001) (black circles) can be accurately fitted to the equation $QE_{Hf} = A.(\Delta E)^{2.2}$, where A is a constant (solid line). This is to be contrasted to the $(\Delta E)^2$ dependence

derived by Fowler [30] and DuBridge [26] (dashed line) – analyses that do not include the local density of states of either the emission (metal) or recipient (vacuum) states. The slight deviation of QE_{Hf} from the $(\Delta E)^{2.2}$ dependence observed for ΔE greater than about 0.7 eV is due to dispersion (i.e., minimum) of the emission band in the $\Gamma \rightarrow A$ direction (see Figure 6.1). In contrast, the evaluated spectral dependence of the QE of the modeled 1*s* defect state in HfO_2 (open circles) effectively saturates for $\Delta E > 1$ eV, allowing the electrons emitted from the Hf metal to dominate the total MTE at high photon energies (Figure 6.3). At lower excess energies, the rate of increase of the QE with ΔE are comparable for Hf(0001) and the defect state in HfO_2, so that the higher MTE from electrons emitted from the oxide layer dominates. The value of x has no real physical meaning in the displayed fit to the experimental MTE measurements as the number density of populated defect states in the native oxide layer on the single-crystal Hf(0001) photocathode is unknown; as a result, the density of emitting defect states cannot be directly compared to the local density of states of the emitting metal band states.

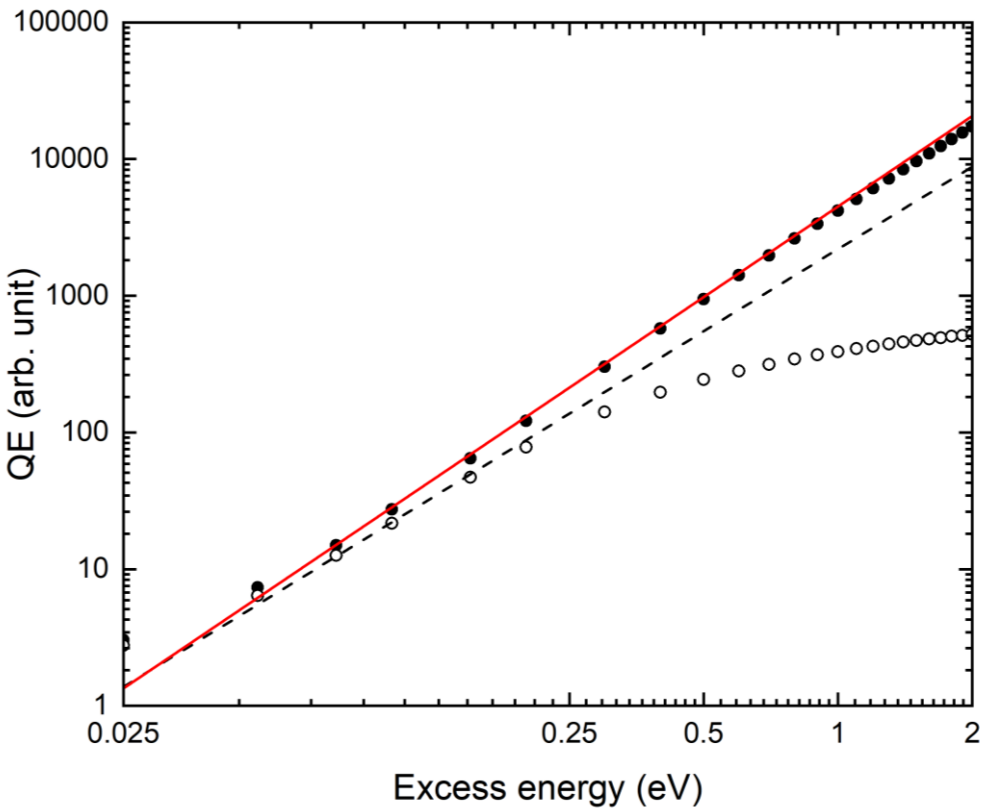

Figure 6.4: The quantum efficiency (QE) as a function of excess photoemission energy (ΔE) evaluated using our one-step photoemission simulation for Hf(0001) (black points) and a hydrogenic 1*s*-like defect state in HfO_2 (open circles). Both sets of data are normalized to unity at $\Delta E = 0$. The Hf(0001) QE closely follows a $(\Delta E)^{2.2}$ dependence (red line), but is not consistent with the $(\Delta E)^2$ trend predicted by Fowler [30] and Dubridge [26] (dashed line).

The good agreement between the experimental data and the described two-component theoretical fit illustrated in Figure 6.3 implies two important conclusions. First, as a constant fitting value of *x* is sufficient, the wavelength-dependent complex refractive index of both the oxide and the metal do not appear to strongly influence the MTE of the emitted electrons. This is to be expected since the ~10 Å thickness of the HfO_2 oxide layer is much smaller than both the UV absorption depth [104] (for the 3.2-5.3 eV experimental spectral range) and all the incident UV wavelengths, implying that there should no significant change in the incident UV radiation intensity (e.g. due to interferometric effects) over the oxide layer thickness. Second, the MTE of the electrons emitted into the vacuum from the underlying Hf metal is not affected

by the intermediate oxide layer; that is, ~10 Å of HfO_2 is too thin to allow for significant scattering effects or energy-dependent recombination during the time-of-flight of the photo-emitted electrons in the oxide layer. In other words, the employed one-step photoemission model [20] is appears to be valid even though it effectively requires the virtual excited electronic state in the metal to couple coherently through the oxide layer to a vacuum state for all excess photoemission energies. This view is consistent with recent results obtained for negative electron affinity (NEA) GaAs-based spin-polarized photocathodes where the employed ~2nm Cs_2Te surface coating to attain NEA performance did not affect the fidelity of the spin-polarized electron output [113].

It is interesting to note that the characteristic momentum width Δp used to simulate the oxygen defect states in the HfO_2 layer corresponds to an effective Bohr radius of the 1*s* state of 5.1 Å, which is significantly larger than the ~2 Å Hf-O bond length in any isomorph of HfO_2 [114]. As a result, the electric field experienced by the electron in the 1*s* state bound to the positively charged center of the oxygen vacancy will be the Lorentz local field, from which a value of 27 extracted for the relative dielectric constant of HfO_2 – a value that is consistent with prior measurements [27]. The effective diameter of the 1*s* defect state is also comparable to the expected ~12 Å thickness of the oxide layer on the 'as delivered' polished Hf(0001) photocathode, implying that quantum confinement effects perpendicular to the Hf(0001)/HfO_2 photocathode surface may play a role. This possibility has not been included in the photoemission analysis, which assumes a spherically symmetric bulk 1*s* state wave function, and it should not have a significant effect since it is the transverse momentum distribution of the defect state wave function that primarily determines the MTE.

6.4 Summary

The presented analysis of the spectral MTE measurements for both the Hf(0001) and Hf(0001)/HfO_2 photocathodes support two definite conclusions. First and foremost, the agreement between our band-based one-step photoemission simulation and the spectral dependence of the MTE data obtained for the polished Hf(0001) photocathode clearly indicates that emission from bulk electronic states with dispersions characterized by transverse effective masses with a magnitude less than the free electron mass m_0 results in MTE values significantly less than the $\frac{1}{3}\Delta E$ variation of Dowell and Schmerge [18] (Figure 6.2). This result is therefore consistent with expectations that bulk emission bands with dispersions, transverse to the emission direction, stronger than that of the vacuum states will restrict the possible transverse momenta of the photo-emitted electrons and thereby reduce a photocathode's intrinsic emittance (i.e., MTE) [9,20]. Further, the result then provides criteria for the discovery of (or search for) solid-state photocathodes with (ultra-)low emittance using *Ab initio* techniques. Ideally, to improve the QE over that of Hf(0001), the effective density of emitting states should be increased by employing either a band state with a large longitudinal effective mass or multiple low effective mass emission bands.

Second, the comparison and corresponding analysis of the spectral MTE measurements of the in-house polished Hf(0001) and as-delivered Hf(0001)/HfO_2 photocathodes strongly suggests that thin (~10 Å or less) oxide layers will not necessarily deleteriously affect the emission properties of the oriented single-crystal photocathodes selected to provide low intrinsic emittance. Surface oxide layers with a thickness of the order of a mono-layer may not have a sufficient density of populated states to overcome the stronger photoemission from the bulk band states – as appears to be the case for Rh (110) [25] (chapter 4) and likely also for the

polished Hf(0001) photocathode studied here. As the oxide thickness increases, emission from occupied electronic states in the oxide layer becomes more prominent and will likely dominate the MTE at low excess photoemission energies due to their quantum properties, such as the size in momentum space of the wave function associated with the oxygen vacancy defect states in HfO_2. Perhaps more importantly, the dipole generated at the metal-oxide interface reduces the effective work function of metal photocathodes, potentially simplifying the requirements for the UV laser radiation source. For Hf(0001) at 300 K the work function is reduced by ~1 eV to 3.35 eV, thus allowing the ~3.5 eV third harmonic of ~1 μm laser radiation sources (e.g. Nd:YAG and Yb:fiber) to be used – our analysis indicating that the MTE of the resultant electron source to be 50-120 meV depending on relative emission strengths of Hf(0001) and the HfO_2 layer on the photocathode.

The theoretical portion of the analysis has also presented a means by which the employed one-step photoemission simulation from electronic band states can be amended to handle fixed energy states; in particular, hydrogenic 1*s*-like states associated with defects and dopants, etc. (Appendix D). In general, and in keeping with the modeled oxygen defect state in HfO_2, photoemission from such populated electronic states is shown to produce a relatively constant MTE when the excess energy is sufficient to allow for the emission of most of the transverse momentum distribution of its quantum state. This constant MTE at $\Delta E > 0.5$ eV is shown to be consistent with the high dielectric constant of HfO_2.

CHAPTER 7

SINGLE CRYSTAL Cu PHOTOCATHODE

In this chapter, I will present the data obtained during a short-term research project at the Lawrence Berkeley National Laboratory (LBNL) that has contributed significantly to our overall understanding and practical implementation of metal photocathodes. In this case, the spectral characterization of single-crystal Cu photocathode in a UHV (Ultra High Vacuum) (~10^{-10}torr) vacuum chamber with a 250-280nm (4.43-4.96eV) UV radiation source based on a Ti: Sapphire laser system. These experimental studies required UHV conditions and the surface cleaning processes available with the LBNL photocathode characterization system due to the high chemical reactivity of Cu[115]; specifically, to avoid photoemission from electronic states in copper oxide surface layers. Amongst the primary crystal faces of Cu, only Cu (100) is found to be a good single-crystal photocathode material in the 260-270nm wavelength range, which includes the fourth harmonic of Nd:YAG lasers. In the first section of the chapter, I briefly explain the experimental setup and the experimental method used to measure both the MTE and QE, and then I compare experimental data with theoretically obtained values using the same photoemission simulation method employed in chapters 4 and 6.

As the photocathode characterization system at LBNL also has the capability to cool the photocathode samples to cryogenic temperatures, two sets of measurements will be presented: one at room temperature (300K) and another at 35K after cooling using liquid helium. Lowering the temperature of a metal photocathode will curtail emission from the Boltzmann tail of the electron distribution and thereby offers a means to reduce the MTE of

emission near the photoemission threshold (i.e. $\Delta E \approx 0$), albeit at the likely expense of a significantly reduced QE.

7.1 Experimental Setup

7.1.1 Experimental chamber and Laser system

The experimental chamber at LBNL has two parts; the sample preparation chamber and the characterization instrumentation. A full description of the experimental system can be found in Corin Greaves's thesis[116]. As the LBNL photocathode characterization system detects low kinetic energy electrons emitted from the photocathode surface, the vacuum quality and residual electric and magnetic characterize fields present in the experimental chamber are important factors to consider. The UHV chamber is built using a custom three-level Mu-Metal[116]. A Load Lock Transfer Port is used to introduce samples into the analysis chamber on the sample preparation level, and an axially mounted 3-axis sample manipulation is used to capture the sample[116]. At the sample preparation level, sample cleaning by Ar+ ion sputtering and sample annealing (i.e. heating), and surface analysis via Low Energy Electron Diffraction (LEED) (ErLEED 150, LaB6 Cathode)[116] and Auger spectroscopy are conducted. Thereafter, the sample is transferred vertically down to the characterization chamber. UV transmitting sapphire viewports (Kurt J, Lesker VPZL-275S) are used in the analysis level for optical analysis of the sample as well as in the Time of Flight (ToF) detector head[116]. The pumping level of the chamber houses the Turbo and Ion pumps, non-evaporable getters, roughing valve, nitrogen leak valve, and Ion and Piriani gauges[116]: After a full bake at 120 °C for 72 hours, the chamber is capable of reaching base pressure of 2×10^{-10} Torr.

(a) (b)

Figure 7.1: Photocathode characterization laboratory. The analysis chamber, laser system, control electronics rack, and transfer magnetic arm are visible. (b) Photograph of the experimental chamber from the LEED port side (preparation level). The analysis level is below the LEED port.

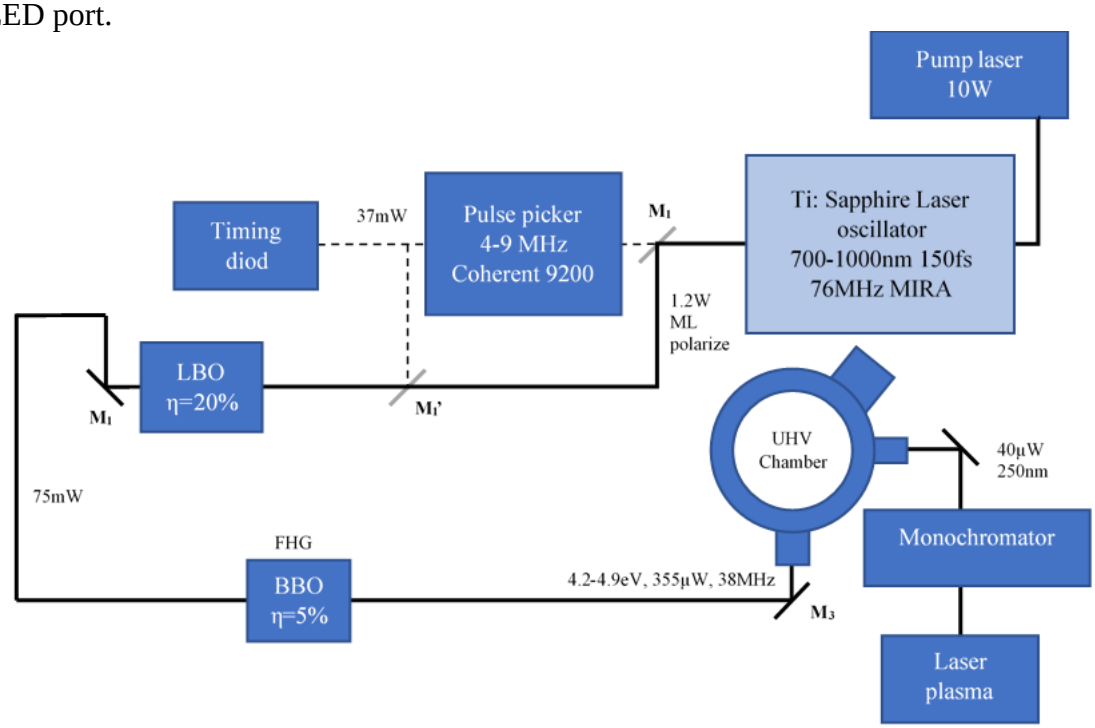

Figure 7.2: Schematic diagram of laser system and the characterization chamber[116].

The 4.2-4.9 eV UV photon energies for the photocathode characterization system[117] are provided by a wavelength-tunable, frequency-tripled, ~150 fs pulse-width, Ti-Sapphire

oscillator (Coherent MIRA) pumped by a 10 W 532nm Coherent Verdi CW laser. An acousto-optic pulse picker (Coherent model 9200) was used to decrease the 76MHz repetition rate of the Ti:sapphire laser to 3.8 MHz in order to stay below the maximum trigger rate of the delay-line-detector. To minimize the effects of the photon energy spread on the measurements, the spectral width of this tunable sub-picosecond UV radiation source was reduced to ~1.5 meV using a diffraction grating-based monochromator. The photon energy could be tuned with an accuracy of 15 meV.

The electron energy and position analyzer comprise of the sample, and a delay-line-based ToF detector arranged in a parallel plate configuration with a separation of ~ 4 cm. The sub-picosecond UV laser pulse is focused onto the sample with an incident energy low enough to ensure that no more than one electron is emitted per pulse. The emitted electron is accelerated towards the detector by an accelerating voltage of a few volts. The ToF detector measures the transverse position of the electron striking the detector and the time of flight of the electron from the sample to the detector. These measurements can be used to infer the transverse and longitudinal momentum of the electron at the time of emission and, consequently, the total energy and transverse momentum distributions. Further details of this setup are given elsewhere[117].

7.1.2 Experimental procedure

For this work, an atomically clean and ordered Cu (100) surface was prepared by performing repeated ion-bombarding and annealing cycles on a commercially purchased (to mirror-like finish), single-crystal Cu (100) sample. 1 keV Ar^+ ions were used for ion-bombarding while annealing was performed at 600°C for 30 minutes in an ultra-high vacuum

(UHV) chamber with a base pressure in the low 10^{-10} torr range. The ion-bombarding and annealing cycles were performed until a sharp low energy electron diffraction (LEED) pattern of the (100) surface was obtained (Figure 7.3), and Auger Electron Spectroscopy (AES) showed the surface to be free of carbon and oxygen contaminants.

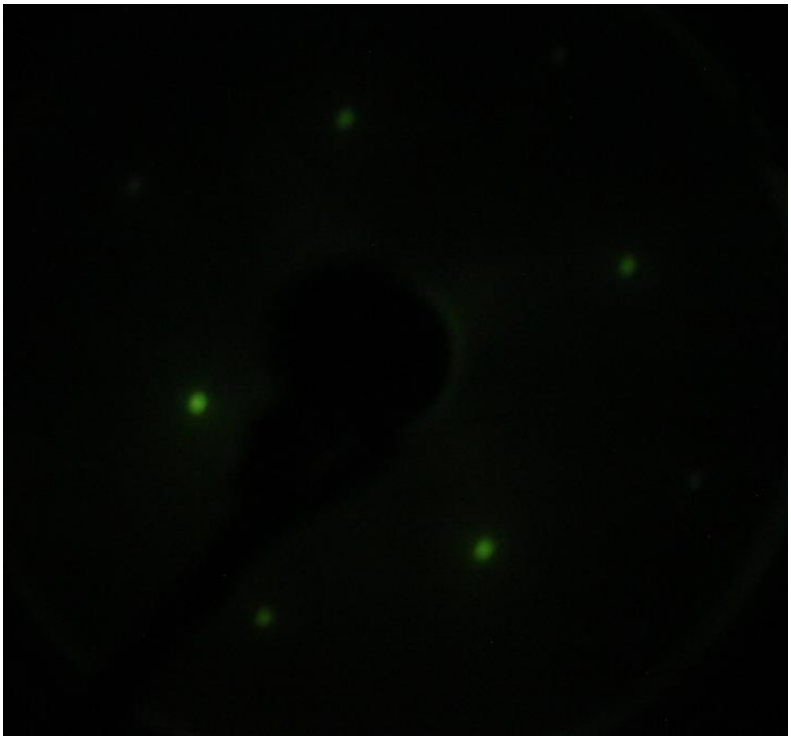

Figure 7.3: LEED image obtained for Cu (100) surface after cleaning the surface.

The sample was then transferred in UHV into a time-of-flight (ToF) based energy analyzer capable of measuring 3-D electron energy distributions of milli-eV energy scale electrons[117]. Two accelerating voltages of 8 V and 4 V between the sample and the detector were used for the measurements. The transverse position of the electrons on the detector and the time of flight was used to obtain the transverse momentum distributions. Both values are directly measured by the detector. The MTE is calculated from these transverse distributions. The MTE values obtained at 8V and 4 V accelerating voltages are identical within the

experimental uncertainty, indicating that the effect of stray fields on the MTE measurement is negligible[27].

Obtaining the longitudinal momentum of the emitted electrons from the time of flight measurement requires a detailed calibration of the work function difference and distance between the sample and the detector. A calibration was performed to ensure that the longitudinal momentum distribution does not change with the voltage applied between the sample and the detector, and that the energy of the Fermi edge in the total energy distribution increases with increasing photon energy. The details of the calibration procedure are given elsewhere[117]. The calibration procedure gave a detector-sample distance of 40.3±0.1 mm and the work function difference of 360±10 meV. These values were used to obtain the longitudinal momentum distributions and the complete total-energy- transverse-momentum distributions. All the measurements could also be performed while the sample was cooled to 35 K using a continuous flow liquid helium cryostat connected to the sample holder[27].

7.2 Band structure of Copper

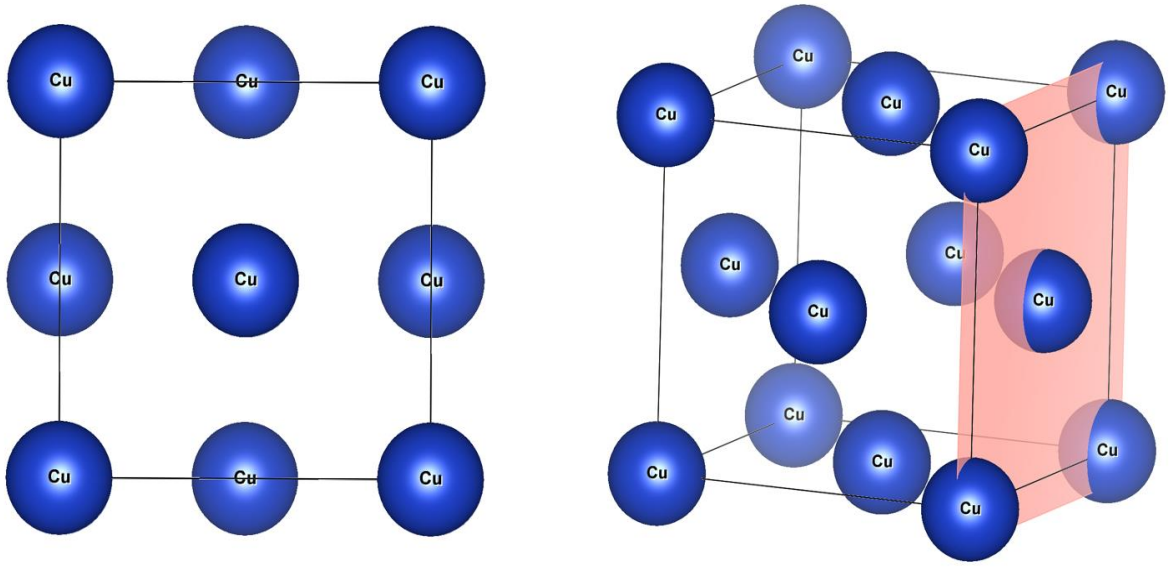

Figure 7.4: Cu crystal structure; FCC structure with an optimized lattice constant a = 3.5719 Å. The right panel is the top view, and the left panel is the 45^0 rotated view with (001) plane indicated. The unit cell contains 4 atoms. (1/8*8 for corners and 1/2*6 on the face)

The DFT calculations of the band structure (and work function) for the bulk Cu crystal, include full relativistic effects, with spin-orbit coupling included during the plane wave self-consistency iterations. That is to say, a fully relativistic pseudopotential within the generalized gradient approximation (GGA)[63] was employed, and the electronic wave function is described by a plane-wave basis set with an energy cut-off of 55 Ry. In addition, the energy cut-off for the charge density is set to 320 Ry, a threshold of 10^{-6} Ry for the ground state energy is used, and a Marzari-Vanderbilt smearing[64] with a broadening of 0.08 Ry is employed. The resulting DFT calculated face-centered cubic crystal structure for Cu has a lattice constant a = 3.5719 Å, which is within 2% of the experimental value[118]. The crystal structure obtained using the optimized lattice constant is shown in Figure 7.4. Figure 7.5 shows the Cu band structure calculated along the k-path $\Gamma \xrightarrow{\Delta} \mathrm{X} \xrightarrow{Z} \mathrm{W} \xrightarrow{\mathrm{Q}} L \xrightarrow{\wedge} \Gamma \xrightarrow{\Sigma} \mathrm{K}$ in the first Brillouin zone, where Δ, Z, Q, Λ, and Σ, are symmetry lines with lengths are $\overline{\Gamma\mathrm{X}} = 2\pi/a$, $\overline{\Gamma\mathrm{L}} = \sqrt{3}\pi/a$, and

$\overline{\Gamma K} = 3\pi/\sqrt{2}a$. For convenience, the Fermi level depicted by the horizontal dashed line is set to zero energy. My electronic band structure is identical to that evaluated by G. Burdick[119].

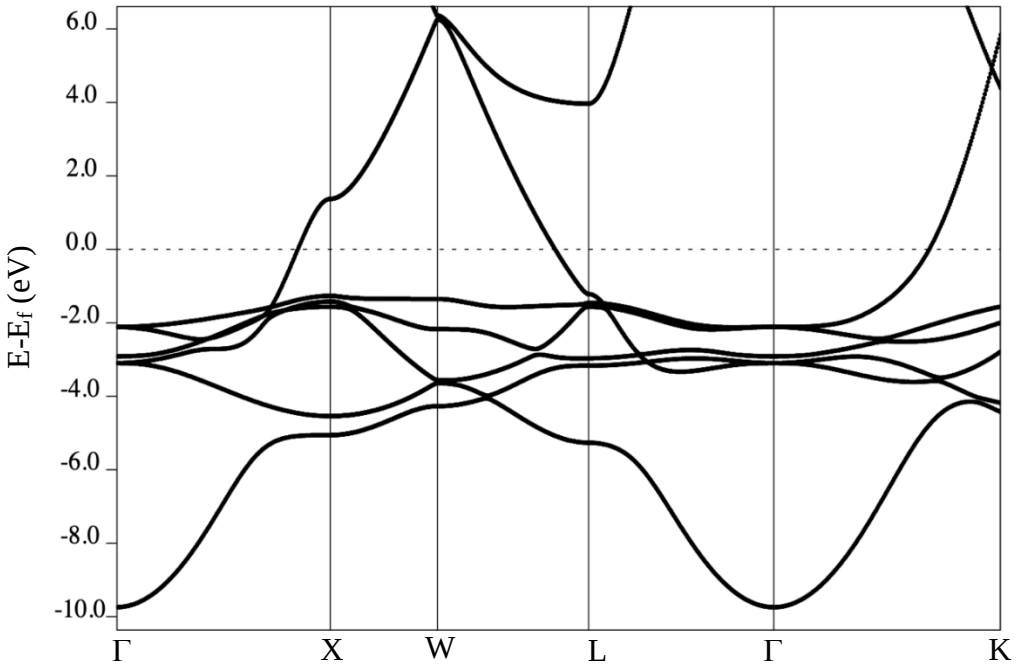

Figure 7.5: Cu band structure along with high symmetry points. The horizontal line at 0 eV represents the Fermi level. Γ→ X is the (001) crystal direction, and Γ→K is the (110) crystal direction.

Due to the conservation of energy and transverse momentum, only electrons close to the Fermi level crossing in the Γ − X direction can be emitted from the Cu (100) surface when the photon energies are within a few 100 meV of the threshold. The transverse momentum of emitted electrons along the Γ − X direction is zero for the Cu (001) face. However, electrons emitted from band states that are transverse to the Γ − X direction close to the Fermi crossing result in the non-zero MTE. Moreover, it is important to note that there are no bulk states in the band-structure of Cu at the 4-5 eV work function energy[41] above this Γ − X Fermi crossing (Figure 7.5). Therefore, low excess energy electrons can only be directly emitted into the vacuum states through a one-step photoemission process. Electrons near other Fermi level

crossings or other locations on the Fermi surface, not close to the Γ−X Fermi crossing, have too large of a transverse momentum to satisfy both the conservation of energy and transverse momentum simultaneously in unassisted single-photon photoemission and hence cannot be emitted[27]. Within the photon energies we have used in this experiment and the band structure figure clearly indicates that there is no two-photon photoemission for Cu (100).

As shown in Figure 7.6, the dispersion of the band states in the vicinity of the Γ−X Fermi crossing that contribute to one-step photoemission for Cu(001) are very well described by an analytical expression of the form

$$E(p) = E_0 + a_z cos[b_z(p_z - p_0)] + c_1 p_T^2 + c_2 p_T^4, \qquad 7.1$$

with the fitting constants E_0 = 0.09491 eV, a_z = -1.474 eV, b_z = 1.93 $(m_o.eV)^{-1/2}$, p_0 = 3.237 $(m_o.eV)^{1/2}$, c_1 = 1.382 m_0^{-1}, and c_2 = -0.3844 $(m_o^{-2}eV^{-1})$ for the case where the Fermi energy is set to zero. It is important to note that the analytical fit given by Equation 7.1 indicates that the inflection point of the longitudinal dispersion of this band is very close to the Fermi level; it is located at p_z = 4.051$(m_o.eV)^{1/2}$ with the longitudinal Fermi momentum p_{fz} = 4.084$(m_o.eV)^{1/2}$. As a result, the effective longitudinal electron mass, $m_z = \left(\frac{\partial^2 E}{\partial p^2}\right)^{-1}$, becomes asymptotically large and thus will affect the quantum transmission (electron probability current) over the photoemission barrier (see Appendix A). Nonetheless, within the parabolic band approximation successfully employed to explain the spectral dependence of both the MTE and QE from a Rh(110) photocathode[25] (see chapter 4), the band dispersion can be reasonably well approximated using E_0 = -7.69eV, p_0 = -1.266 $(m_o.eV)^{1/2}$, m_z = 1.86m_0, and m_T = 0.39m_0 in the expression

$$E(p) = E_0 + \frac{(p_z - p_0)^2}{m_z} + \frac{p_T^2}{m_T}, \qquad 7.2$$

where again the Fermi energy is set to zero. The relatively low value of the transverse effective mass is due to a 'bulge' in the Fermi surface in the Γ − X direction, and its value is sensitive to relativistic pseudopotential and spin-orbit coupling parameter (Slater determinant[101]) used in the DFT calculation.

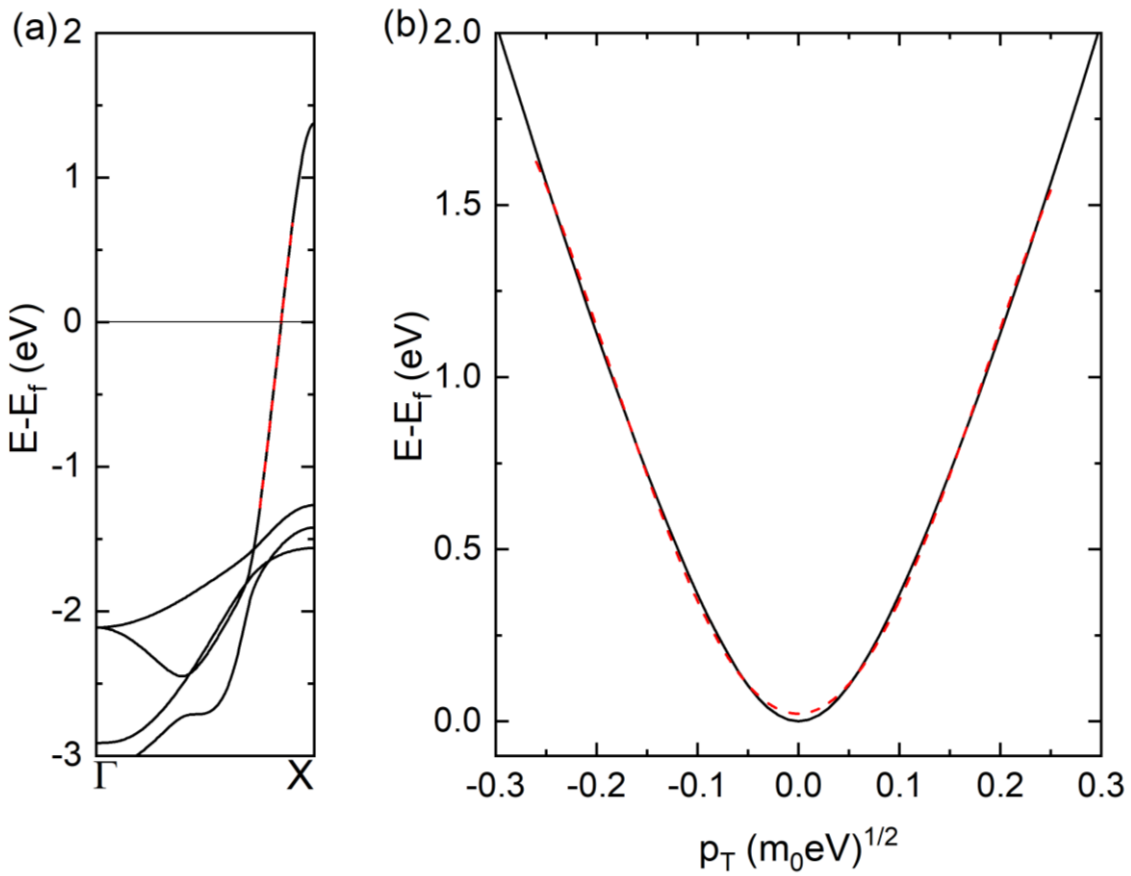

Figure 7.6: (a) Band structure of Cu along the Γ – X direction with the Fermi energy set to zero. The band structure includes parabolic dispersion fits (red dashed lines) to the emitting that crosses fermi level. (b) Band structure for Cu along transverse direction for emitting band. The red dashed lines indicate the parabolic fits used in effective mass calculation along transverse direction.

The work function for a clean Cu (100) photocathode surface was also calculated using the thin-slab technique[68]. A Gaussian-spreading of 0.05 Ry, fully relativistic

pseudopotentials, and n×n×1 Monkhurst-Pack[57] k points were used in this DFT-based evaluation to obtain convergence within 0.05eV. A value of ϕ = 4.74(±0.2)eV for the Cu(001) crystal surface was extracted which is within the range of the accepted value of 4.73(±0.21)eV for Cu(001)[41].

7.3 Room temperature measurements

In this section, I describe the results of the room temperature (300K) spectral characterization of a Cu(001) single-crystal photocathode performed at LBNL. First, the results of the QE measurements will be used to extract the work function in order to set the energy scale for the comparison of the MTE with the one-step photoemission simulations employing different mathematical characterizations of the Γ-X emission band. The following section 7.4 analyzes the experimental data obtained at 35K.

7.3.1 Cu (001): Quantum Efficiency at 300K

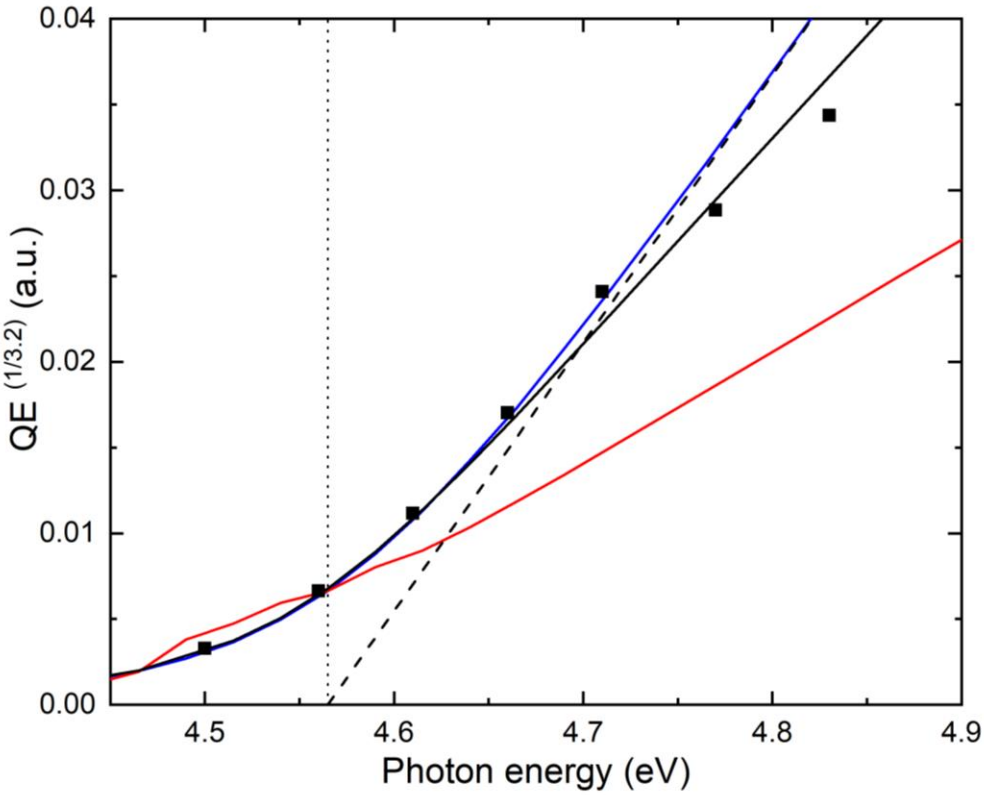

Figure 7.7: Measured QE (data points) to the 0.3125 = $(3.2)^{-1}$ power as a function of incident UV photon energy for a clean Cu (001) photocathodes at 300K: The one-step photoemission simulation fit to the experimentally measured QE (black data points). Parabolic dispersion relationship (equation 7.2) used in the chapter 4 using m_T=0.39m_0 (blue solid line) and m_T=0.89m_0 (black solid line) and the cosine fit (equation 7.1) relationship (red solid line) and linear fit (black dashed line) to high excess energies for extraction of φ = 4.565 eV (thin vertical dotted line)

Figure 7.7 (data points) together with the results of the one-step photoemission simulation employing both Equation (7.1) (red line) and the cylindrical parabolic band approximation of Equation (7.2) (blue and black solid lines). As for Rh(110) (see Figure 4.3), the QE is raised in this case to the power of 0.3125 = 1/3.2 – the inverse of the power law dependence of the QE on the excess photoemission energy ΔE predicted using the parabolic band approximation (Equation 7.2) – in order to extract a value for the work function of 4.57(±0.02)eV[41]. This experimental value for $\phi_{Cu(001)}$ is at the bottom end of the range

predicted by my thin-slab calculation. More interesting is the fact that only the parabolic band approximation predicts the correct trend of the QE with incident photon energy measurement of the QE for the highest two photon energies was affected by electron loss due to beam size on the detector. In fact, it is in very good agreement with the experimental measurements (data points) and illustrates the effect of the 300K Boltzmann tail in the electron distribution when ΔE is less than 0.1eV. On the other hand, the spectral dependence of the QE simulated using Equation (7.1) (red line in Figure 7.7)is clearly not consistent with the experimental data even though it provides a better fit to the band dispersion. The reason for this is still under investigation. However, it is again evident that the QE does not increase as ΔE^2 , as in prior photoemission analyses[18,19], which is due to the density of states of both the emitting bulk band and recipient vacuum states – the joint density of states for the one-step photoemission transition.

7.3.2 Cu (001): Mean transverse energy at 300K

Figure 7.8 displays the spectral dependence of the MTE for photoemission from Cu(001) at room temperature with the extracted 4.57eV work function value indicated by the thin vertical dotted line. In this case, the one-step photoemission simulations for the near exact and approximate parabolic (red and dashed black lines) band dispersions (Equations 7.1 and 7.2 respectively) are both quite inconsistent with the measured MTE values (data points). Both of these simulations attain a limiting value at negative ΔE of around 14meV, which is 40% larger than the value of $(m_T/m_0)k_BT_e$ = 10meV that would be expected if density of states of both the emission bands and the vacuum were omitted[20]. They also both underestimate the MTE of electron emission by a factor of at least 2. Indeed, as shown by the black line in Figure 7.8, the experimental MTE data is a good fit to a one-step photoemission simulation when the

transverse effective mass is increased to $0.89m_0$ in the parabolic band approximation. (The last data point at $\hbar\omega = 4.83$eV may be erroneous due to the difficulty of extracting an accurate value of the MTE for large electron beam spot sizes on the employed micro-channel plate detector.) The reason for this discrepancy is also currently under investigation: One can speculate that phonon scattering may be involved, especially surface photons, since they will be present for the pristine clean Cu(001) surface, but likely strongly suppressed in my Rh(110), Mo(001), and W(001) measurements due to the presence of a thin 1-2ML oxide.

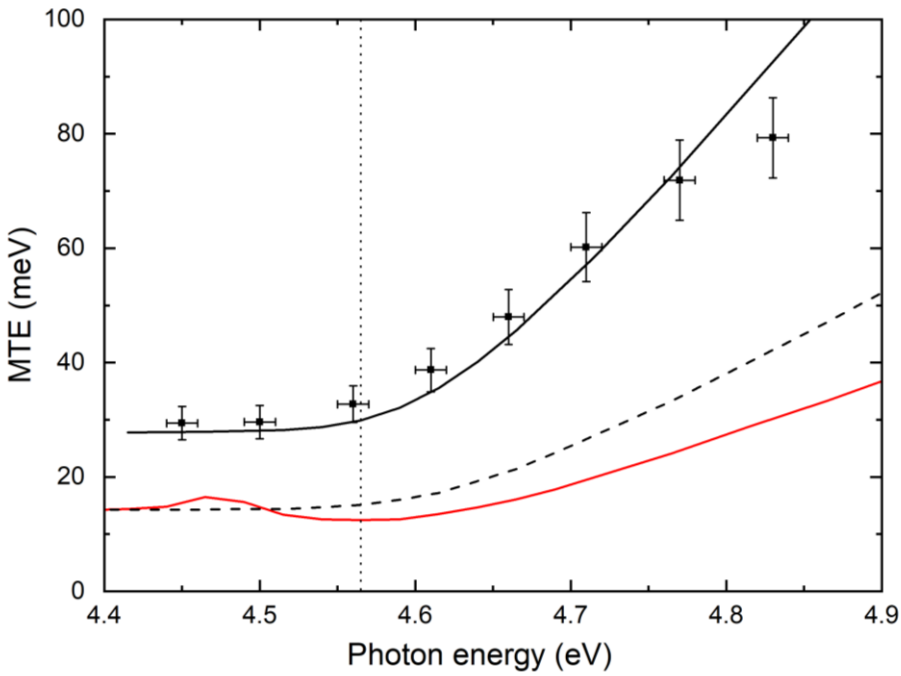

Figure 7.8: The Measured MTE (data points) as a function of incident UV photon energy for a clean Cu(100) photocathode at 300K: Black solid line is a zero free parameter one-step photoemission simulation including the vacuum density of states and using $\varphi = 4.57$eV (thin doted vertical line) and m_T=0.89; Black dashed line represents the one-step photoemission simulation result using m_T=0.39; Red solid line represents the simulation result using cosine fit (equation 7.1)

7.4 Cryogenic Measurements

In this section, I discuss the experimental data obtained for the Cu(001) photocathode at 35K – the cryogenic temperature attained upon liquid Helium cooling as measured in the vicinity of the photocathode. In addition to the QE and MTE measurements, the combined total kinetic energy and transverse momentum photo-electron distributions are presented for two incident photon energies to show that both a small MTE and a narrow kinetic energy distribution can be obtained at 35K close to the photoemission threshold.

7.4.1 Cu (001): Quantum Efficiency at 35K

The measured spectral dependence of the QE for the clean Cu(001) photocathode surface at 35K is shown in Figure 7.9 (data points) together with three sets of results from the one-step photoemission simulation normalized to the same value at $\Delta E = 0$. Again the QE is assumed to increase as $(\Delta E)^n$ so that a plot of $(QE)^{1/n}$ against $\hbar\omega - \phi$ generates a linear dependence for the extraction of the work function[51]. In this case, a value of $n = 2.75$ generates the required linear dependence for the measured QE and the simulations employing Equation 7.1 (blue line) and the parabolic band approximation with $m_T = 0.89m_0$ (black line), allowing a value of $\phi_{Cu(001)} = 4.33(\pm 0.02)$eV at 35K to be determined. This work function value is less than that at 300K, which is counter intuitive since a real space reduction in crystal volume at a lower temperature increases the volume of the Brillouin zone in momentum space thus lowering the Fermi level and increasing the work function (assuming the vacuum energy level is constant).

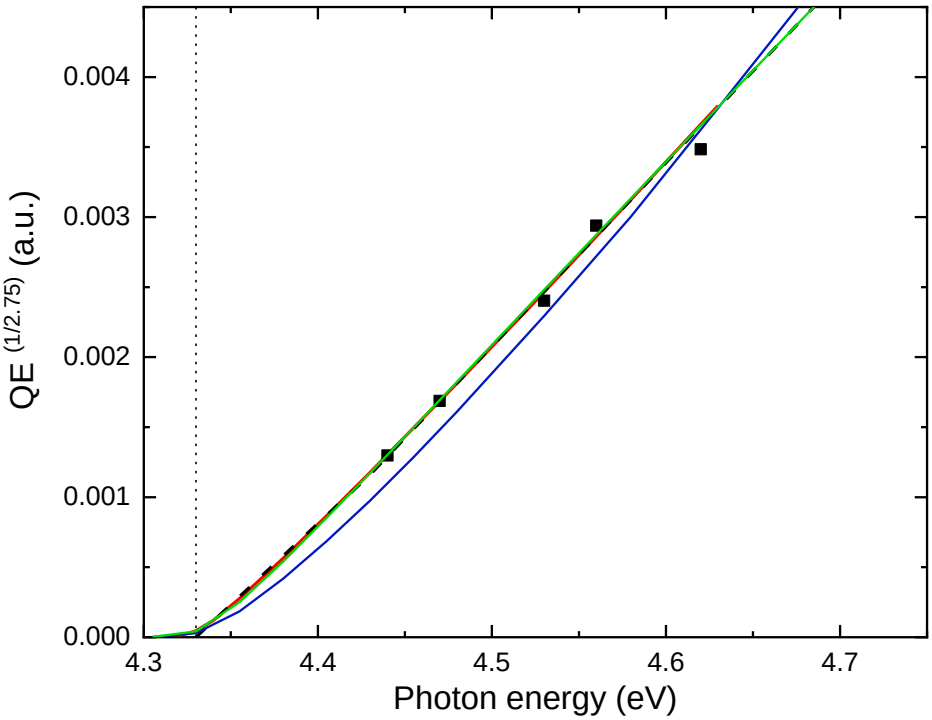

Figure 7.9: Measured QE (data points) to the 0.3636 = $(2.75)^{-1}$ power as a function of incident UV photon energy for a clean Cu (100) photocathodes at 35K: The one-step photoemission simulation fit to the experimentally measured QE (black data points). Parabolic dispersion relationship (equation 7.2) used in the chapter 4 using m_T=0.39m_0 (green solid line) and m_T=0.89m_0 (red solid line) and the cosine fit (equation 7.1) relationship (blue solid line) and linear fit (black dashed line) to high excess energies for extraction of φ = 4.33 eV (thin vertical dotted line).

The fact that the better analytical fit to the band structure (Equation 7.1) is now in better agreement with the experiment than at 300K (Figure 7.7) is likely due to the significantly reduced influence of the inflection point in the longitudinal dispersion of the emitting band; specifically, as the band inflection point is ~100meV above the Fermi level, substantially less electrons occupy states in the vicinity of this point at 35K. On the other hand, the one-step photoemission simulations using the cylindrical parabolic band approximation of Equation (7.2) (green line on dashed black line) with m_T = 0.39m_0 does run through the data points, but

the $(QE)^{1/n}$ versus $\hbar\omega - \phi$ dependence is not linear for $n = 2.75$. As was the case for 300K (Figure 7.7), it requires $n = 3.2$ for the theoretical dependence to be linear for $\Delta E > 4k_B T_e$ [20].

The one-step photoemission simulations also indicate that the QE near the photoemission threshold decreases by a factor of ~100 as the temperature is reduced from 300K to 35K due to the temperature dependence of the Boltzmann tail of the electron distribution in the emission band. As a result, the QE falls below the ~10^{-8} detection limit of the experiment for $\Delta E < 0$. For ΔE values greater than ~0.1eV, the QE recovers to values close to that at 300K (Figure 7.7) as emission from the occupied band states below the Fermi level dominates.

7.4.2 Cu(001): Mean transverse energy at 35K

The expectation that decreasing the photocathode temperature will allow for a reduction in the MTE of electrons emitted near the photoemission threshold energy is supported by the spectral measurements (data points) displayed in Figure 7.10 for a Cu(001) photocathode at 35K. For $\Delta E < 25$meV, MTE values less than 10meV are measured, albeit with a significantly reduced QE of ~10^{-8} (Figure 7.9). In order to increase the electron yield from such a cooled metal photocathode, higher incident laser powers will then be required, which are likely to heat the electron gas in the metal increasing its temperature T_e [89] and result in nonlinear (e.g. two-photon) photoemission[120], especially for pulsed lasers. Both effects will increase the MTE of the emitted electrons, negating the benefit of employing a cryogenically cooled photocathode. On the other hand, such a sub-10meV MTE electron source is likely practical and attractive for UED and UEM applications only requiring one (or a few) electrons per pulse[27].

The one-step photoemission simulations all agree with the clear experimental determination that lowering the photocathode temperature reduces the MTE near the photoemission threshold. However, only the simulation employing a transverse effective mass of $0.89m_0$ (red line in Figure 7.10) is in close agreement with the measurements for all excess photoemission energies. Both the simulations using the more dispersive transverse band structure (Equations 7.1 and 7.2) with more accurate m_T values around $0.4m_0$ predict MTE values that are roughly half the measured values – the same discrepancy as observed at 300K (Figure 7.8). Consequently, one can conclude that phonon scattering is not likely to be responsible: For the primary ~3THz surface phonon mode on the Cu(001) surface[121], for example, a reduction in temperature from 300K to 35K should have reduced the scattering rate by a factor of about 10. Further work will therefore be needed to explain this result.

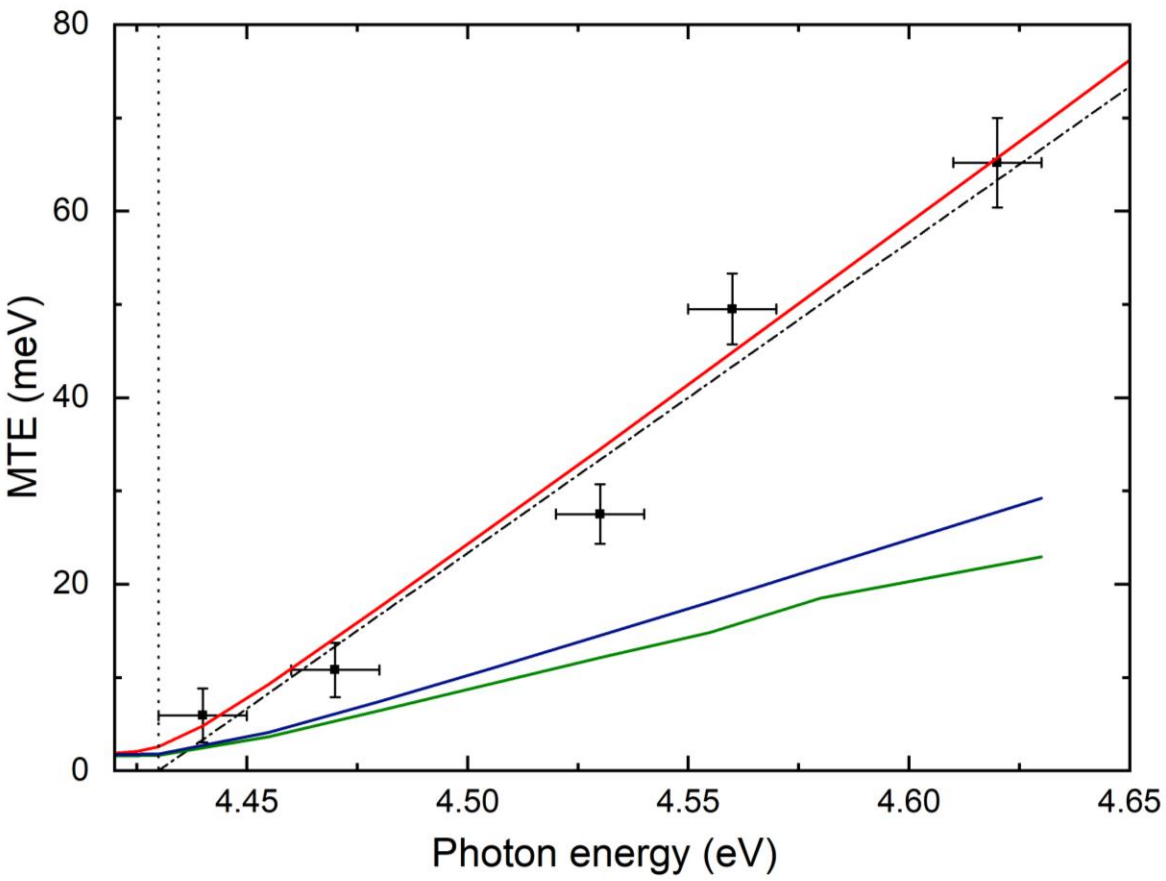

Figure 7.10: The Measured MTE (data points) as a function of incident UV photon energy for a clean Cu(100) photocathode at 35K: Red solid line is a one-step photoemission simulation including the vacuum density of states, m_T=0.89m_0 and using φ = 4.43eV (thin dotted vertical line); dot-dashed line represents the Dowell theory[18]; blue line one-step photoemission simulation including the vacuum density of states, m_T=0.39m_0; green line represents the cosine fit (equation 7.1).

I also note that the one-step photoemission simulations presented in Figure 7.10 assume a Cu(001) work function of 4.43eV (thin vertical line); that is, 0.1eV higher than that used for the QE in Figure 7.9. This small difference is likely due to surface contamination at the 35K cryogenic temperature – predominantly hydrogen under the UHV conditions. Indeed, experiments on a Cu(110) photocathode could not be performed as the more reactive (110)-face of this face-centered cubic crystal[25] ensured that the effective work function value varied throughout the duration of any measurement – the crystal surface effectively acting as a 'getter' for residual gas even under the ~10^{-10} torr vacuum conditions.

7.4.3 Cu(001): Total electron energy-momentum distributions at 35K

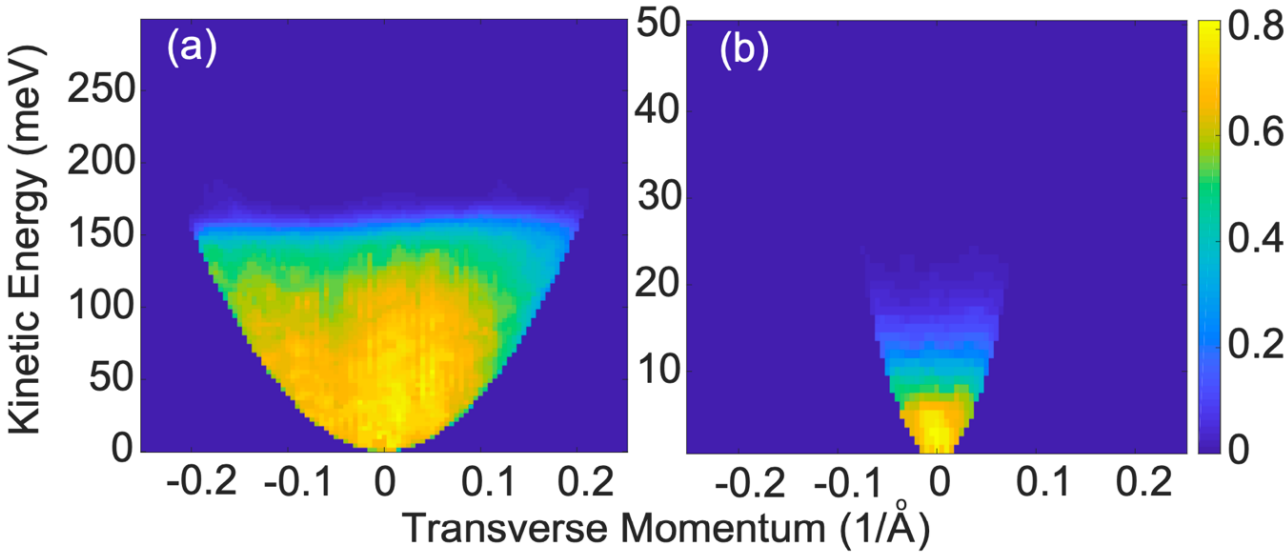

Figure 7.11: Total kinetic energy vs transverse momentum distributions of emitted electrons using photon energy (a) 4.56 eV, (b) 4.43 eV. The transverse momentum spread with the 4.43 eV photon energy corresponds to 5 meV MTE. The figure shows the transverse momentum in only one transverse directions. The distributions are cylindrically symmetric in the transverse plane. The color bar is in arbitrary units.

The careful calibration of the ToF detector in the LBNL photocathode characterization system[117] allows for precise and simultaneous measurement of both the total kinetic energy and transverse momentum electron distributions. An example of two such measurements is shown in Figure 7.11 for the Cu(001) photocathode at 35K; one at an excess energy of 0.13eV and the other near the photoemission threshold at $\hbar\omega$ = 4.43eV. As expected, both the total kinetic energy and transverse momentum of the emitted electrons increases with ΔE, as evidenced by the wider parabolic limit of the distribution in Figure 7.11(a) compared to that in Figure 7.11(b) at the lower ΔE. Integration of these electron distributions over the kinetic energy generates their transverse momentum spread which yields the MTE (through its second moment), which for the 4.43eV incident photon energy (Figure 7.11(b)) is equal to 5meV.

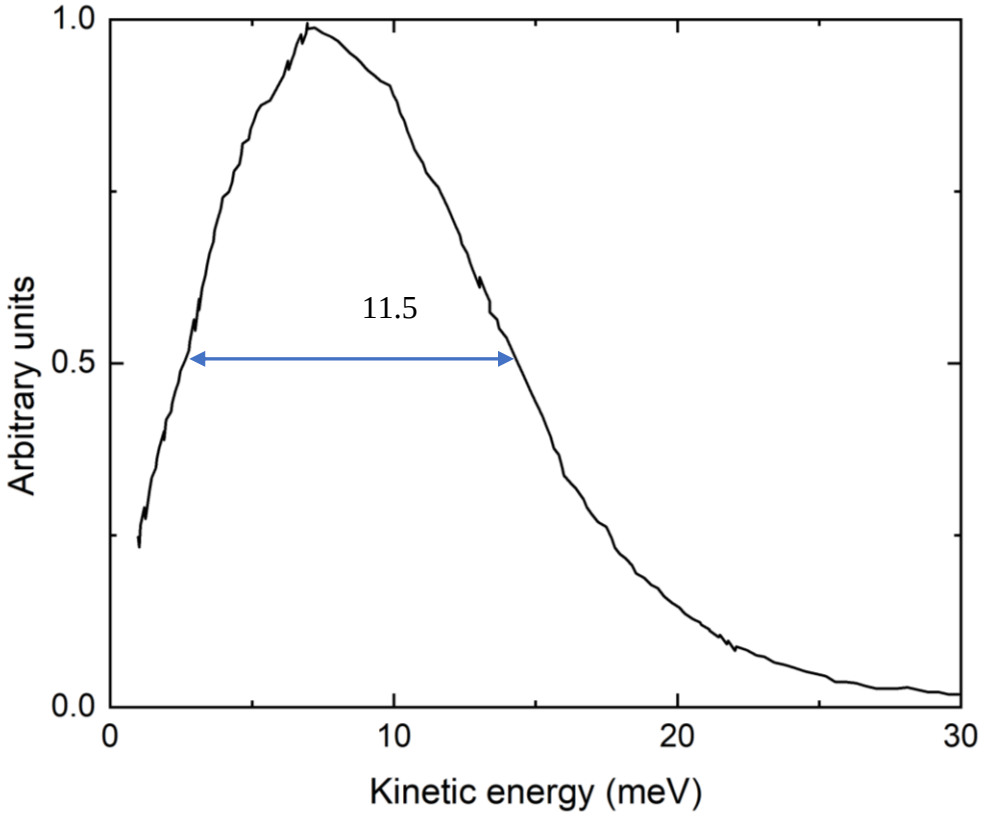

Figure 7.12: Electron energy distribution for a 4.43 eV incident photon energy showing a FWHM spread of 11.5 meV.

Integration of the total kinetic energy and transverse momentum distributions over the transverse momentum yields the energy distribution of the emitted photo electrons. Figure 7.12 shows the electron energy distribution at the near-threshold 4.43eV photon energy which has a measured FWHM energy spread of less than 11.5 meV a value that is limited by the instrumental resolution, the temperature, and the vacuum density of states. The high energy edge in the distribution is given by the Fermi distribution, whereas the low-energy-side rise is due to the small density of vacuum states[20] close to the threshold (increasing as the square root of the total kinetic energy) and the low transmission probability over the photoemission barrier as the kinetic energy goes to zero.

Together with the 5 meV MTE at this incident photon energy, the measured 11.5meV total energy spread implies that a Cu(001) photocathode at 35K has a nearly two orders of magnitude brightness increase over current electron sources used for stroboscopic UED (UEM) applications[4]. Moreover, the low energy spread of this source for such applications that require few to a single electron per pulse can result in dramatically better energy resolution in ultrafast EELS techniques.

CHAPTER 8

CONCLUSION

In this thesis, I have demonstrated that a one-step photoemission simulation, which incorporates the joint density of states between the occupied emitting band and recipient vacuum states, is consistent with spectral measurements of the emission properties of several single-crystal metal photocathodes. In agreement with the one-step photoemission analysis, my work has shown that the QE is not proportional to the square of the excess photoemission energy ΔE, but instead a QE = A.$(\Delta E)^n$ relationship is required and the power n appears to depend upon the occupied DOS and the dispersion of emitting band(s). As a result, a plot of $QE^{(1/n)}$ vs. the photon energy should be used to extract the work function (ϕ) of photocathode material[51]. Moreover, the newly developed photoemission theory indicates that the band dispersion (predominantly the transverse effective mass m_T) strongly affects the MTE; specifically, the MTE is greater than $\Delta E/3$ for large m_T (due to the joint density of states) and MTE < $\Delta E/3$ for sufficiently small m_T (due to the band restriction on available states). During my Ph.D. research work, I have also obtained a record low MTE of 5meV from a cryogenically-cooled Cu(100) photocathode surface using near-threshold photoemission. Near the threshold, when the excess energy is close to or less than zero, photoemission occurs from the tail of the Boltzmann distribution, limiting the MTE to k_BT_e, where k_B is the Boltzmann constant and T_e is the temperature of the electrons in the crystal, thus allowing the MTE to be reduced by cooling cathode material to low temperatures[27].

The spectral characterization of the single-crystal metal photocathodes described in this thesis employed a home-built, 3.0-5.3eV UV tunable, laser radiation source with a solenoid

scan technique[25] coupled to an extended analytical Gaussian beam propagation model[11,23,24] to extract the MTE of electron emission and a Faraday cup for the QE measurements. A diode-pumped, mode-locked femtosecond Yb:KGW oscillator is used as the front end of the laser radiation source. A super-continuum fiber is used to generate ~~a~~ the seed radiation for a 2-stage OPA pumped by the green second harmonic of the Yb:KGW laser, and the amplified tunable signal and idler radiation is used to produce near continuously tunable UV radiation by sum-frequency generation with second and third harmonics of laser oscillator[25]. The p-polarized UV radiation focused to a ~100-micron spot at a 60° angle of incidence on the photocathode surface in 20 kV DC electron gun. The solenoid scan technique is used to measure MTE of the resulting electron beam using a Ce:GAGG scintillator screen[22] and 1:1 imaging onto a CCD camera with 5-micron resolution and an extended Analytical Gaussian (AG) model of the electron beam propagation[23,24]. To obtain QE measurements down to ~10^{-8} electrons/photon, a 5mm-diameter aperture Faraday Cup connected to a pA meter is used to collect all emitted electrons. In addition, the spectral characterization of a Cu(100) photocathode was performed at LBNL using a characterization system in a UHV (~10^{-10} torr) vacuum chamber with a 250-280 nm (4.43-4.96 eV) UV radiation source based on a Ti: Sapphire laser system. The pristine crystal surface was obtained after performing several cycles of ion bombardment Ar^{+} ion bombardment and temperature annealing until a strong low energy electron diffraction (LEED) pattern from the required crystalline surface was observed.

The experimental spectral measurements of the MTE and QE for the single-crystal metal photocathodes are compared to a one-step photoemission simulation that employs a cylindrical approximation to the dispersion of the emitting bands evaluated using DFT techniques. This one-step photoemission model is employed in my theoretical analysis as there

are no higher-lying bands to populate in the studied single-crystal metal photocathodes. Full relativistic effects with spin-orbit coupling are used in the DFT calculations to obtain a band structure with the correct band positions required to achieve the high <100 meV precision in the photoemission analysis. Additionally, the work function for clean single-crystal metals was calculated using the thin slab technique[68]. The developed one-step photoemission simulation then employs a cylindrical band approximation for the evaluated band dispersion E(**p**) around the emission direction and Forbes and Deane's[38] treatment of emission over and under a triangular barrier from a 'virtual' state replicating the characteristics of the band state at the prescribed excess photoemission energy ΔE. Also included in my simulation is the joint density of states involved in the photoemission transition; that is, the density of states of both the emitting bulk electronic bands and the recipient vacuum states. The MTE is then evaluated from the second moment of extracted p_T distribution in the vacuum, and the relative QE is also evaluated by integrating the distribution[20]. In this one-step photoemission simulation, I have not included transition matrix elements, the Schottky effect, optical and chemical properties of material, and finally, carrier-carrier scattering.

In chapter 4, I show that this theoretical formalism agrees with the spectral MTE and QE measurements for a Rh(110) photocathode[25]. Two bands contribute to the photoemission for Rh(110) direction, and the Σ_2 band dominates the photoemission over that of the Σ_1 band due to its substantially larger longitudinal effective mass m_Z in the Γ-*K* direction. The inclusion of both vacuum and bulk band density of states results in (i) a limiting value of the MTE at 300K below the photoemission threshold that is significantly larger than $k_B T_e$ = 25meV and (ii) a QE that follows a power-law dependence on ΔE that is greater (n=2.89) than quadratic (QE ≠ A.$(\Delta E)^2$). Knowledge of this power-law dependence allowed a work function value of 4.23eV to be extracted for Rh(110) using QE data. Critical to the agreement between the

experimental measurements and the one-step photoemission model is a highly accurate knowledge of the energy-momentum positions of the emitting electronic states since this determines their excess energy, the local density of states, and crucially transverse momentum. Even for Rhodium, a second-row transition metal, to achieve the necessary accuracy, the DFT band structure calculation needed to include full relativistic effects and spin-orbit coupling.

In chapter 5, the experimental MTE and QE data for Mo(001) and W(001) are compared to the values predicted from the one-step photoemission simulation. Unlike for the Rh(110) photocathode, the agreement between the experimental data and the photoemission theory is not as good for Mo(001). The DFT band structure calculated using full relativistic effects and spin-orbit coupling along the (001) emission direction for Mo is complex and not well described by a constant m_T in the cylindrical parabolic approximation was used for the 4 bands that cross the Fermi level and contribute to the photoemission. The QE values follow a power-law dependence relationship of $QE = A.(\Delta E)^{2.8}$ and a work function of 3.7 eV is extracted from the spectral dependence of the QE. Compared to Mo(001), the measured spectral dependence of the MTE and QE for W(001) are in better agreement with the prediction of the one-step photoemission simulation despite the stronger relativistic and spin-orbit coupling effects on the band structure. For W(001), there is no contribution from the lens band to photoemission, and only two bands contribute to the emission. In this case, the QE values follow a power-law dependence relationship of $QE = A.(\Delta E)^{3.0}$ and a work function of 3.78 eV obtained.

The experimental study and theoretical analysis of the spectral properties of the Hf(0001)/HfO_2 photocathode I present in chapter 6 is expected to have significant implications for future research in photocathode physics. The band-based one-step photoemission simulation is in agreement with the spectral dependence of the MTE data for the polished

Hf(0001) (polished to remove a thin (~10 Å) oxide layer), and this result clearly indicates that bulk electronic bands with low transverse effective mass ($m_T < m_0$) can emit electrons with a lower MTE than that predicted by the Dowell-Schmerge theory[18]. Consequently, a low transverse effective mass can be used as a selection criterion to discover future low emittance photocathode materials. On the other hand, the QE will need to be improved by increasing the density of emitting states. This study also showed that the thin layer of oxide on the polished Hf(0001) did not deleteriously affect the emission properties of this low-emittance single-crystal photocathode, as a thin layer of oxide does not have a sufficiently high density of states make a significant contribution to the photoemission from the metal. However, as the thickness of the oxide layer increases, the emission from the oxygen vacancy defect states in HfO_2 was shown to dominate the MTE from the Hf(0001)/HfO_2 photocathode at low excess photoemission energies. A modification to the one-step photoemission analysis allowed photoemission from fixed energy states such as 1s-like states associated with defects and dopants etc. to be modeled.

Despite being an intrinsically simpler photo-emitter according to the *Ab initio* band structure calculations, the analysis of the spectral measurements I describe in chapter 7 for a Cu(001) photocathode with a clean surface is evidently incomplete. Although the one-step photoemission simulation is in general agreement with the temperature dependence of the single-crystal photocathode's emission characteristics, the value of $m_T \approx 0.4m_0$ extracted from the DFT band structure calculations leads to a significantly lower predicted MTE value than that measured using the photocathode characterization system at LBNL. Nonetheless, the measured sub-10meV MTE from Cu(001) at 35K just above the photoemission threshold represents a landmark observation in the photocathode community, albeit that it is associated

with a significantly reduced QE due to the much-reduced emission from the Boltzmann tail of the electron distribution at such low temperatures.

In spite of the approximations employed in this Thesis, I would contend that it has laid the groundwork for the selection of potential solid-state photocathode materials by Ab initio techniques that could exhibit (ultra)low emittance (i.e., MTE) at 300K while maintaining a reasonable QE (~10^{-6} or greater) – photocathode characteristics that could improve the performance of XFELs, UED systems and future UEMs by over an order of magnitude. A possible example of such a new photocathode material is the rare-earth pnictide YSb. Its DFT calculated band structure (Figure 8.1) clearly shows the presence of three hole-like low effective mass bands crossing the Fermi level around the Γ point. Moreover, for emission in the Γ-X direction (i.e. from a YSb(001) photocathode), the electron-like band with a minimum at the X point could also contribute to photoemission, and this band also has a low transverse effective mass.

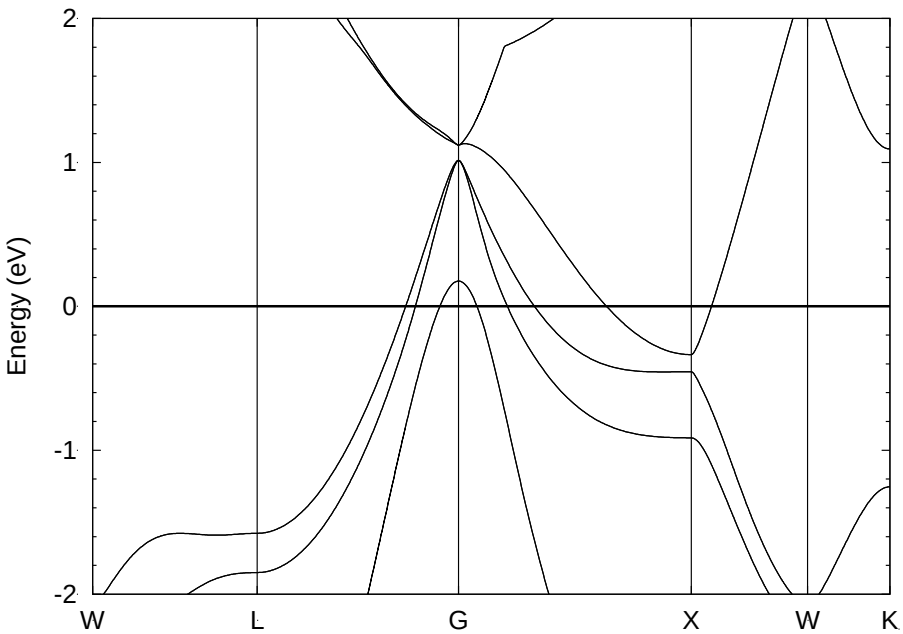

Figure 8.1: Band structure of YSb. Three low effective mass hole like emission bands cross the Fermi level (at zero energy) around the Γ point.

Of course, a more useful theoretical formulation of photoemission than that presented in this Thesis would be one that includes an estimate (or absolute evaluation) of the QE. For the one-step photoemission simulation, I have shown, this is expected to be possible since the formalism it is based on[20] employs essentially the same plane-wave electron description that may be used to evaluate the matrix elements associated with the photo-excitation leading to photoemission. It should also be possible to improve the predictive accuracy of the photoemission simulation by employing the precise E(**p**) dispersion characteristics of the emitting band(s) evaluated by DFT; that is, using an array of Monkhorst-Pack k-points instead of the limited analytical fits to the band dispersion presented in chapters 4, 5, 6, and 7. However, care would then have to be taken to ensure that only electrons from band states 'mapping' correctly to the positive group and phase velocities of the vacuum states can emit.

Several other factors could be included in a more complete one-step photoemission analysis. Amongst these is a physical description of the effect that the finite absorption depth has in the longitudinal direction through the inclusion of the Heisenberg uncertainty principle; specifically, a Δz restriction in emission in real space implies a Δp_z convolution over band states in momentum space. In addition, the intermediate region between the crystal face and the peak of the potential barrier (Schottky effect) usually gets overlooked but it should have periodic potential variations due to the periodic crystal surface potential that could affect the MTE.

APPENDICES

Appendix A

ANALYTICAL DERIVATION OF TRANSMISSION COEFFICIENT

The new theoretical formulation of one-step photoemission was described in chapter 2. The transmission through or over the triangular barrier generated by an applied surface acceleration field E_{acc} of the electron gun has been described by Forbes and Deane's recent exact analytical one-dimensional quantum solution[38]. Below I will present a detailed analytical derivation of the transmission coefficient (equation 2.12) used in the one-step simulation. In this derivation, I assumed a flat planar photocathode surface, and the one-dimensional barrier shown in figure A.1. Electrons move from left to right into the vacuum and are considered as propagating waves.

In figure A.1, the left side (region E) represents the emitter region, and the right side (region V) represents the vacuum. χ represents the potential energy barrier inside emitter, which is assumed to be independent of the acceleration field $E_{acc,}$ and W is the kinetic energy of an electron inside emitter. The transmission energy w is defined as W- χ and positive and negative values of w indicate above the barrier transmission (flyover) and below barrier transmission (tunneling), respectively.

Appendix A (Continued)

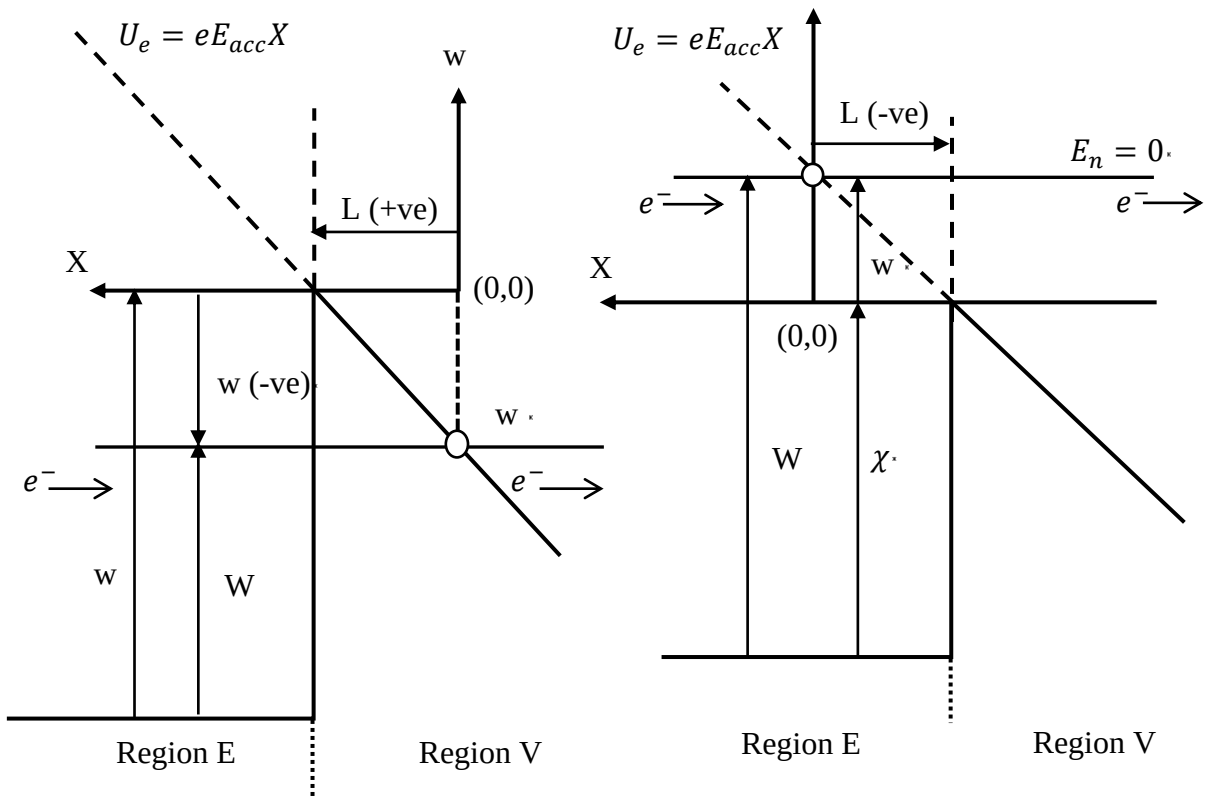

Figure A.1: Schematic of the simulated one-step photoemission process for $m_z = m_0$: Photo-excitation of the electrons from a bulk band states into (with transverse momentum conservation) the vacuum states (effective mass = m_0) either above (photoemission with $\Delta E > 0$, right panel) or below (photo-assisted tunneling with $\Delta E < 0$, left panel) the triangular barrier generated by the applied acceleration field in an electron gun: E_{acc}.

<u>Below barrier transmission ($\Delta E < 0$)</u>

The electron's potential energy, U_e, is W in the region E and $eE_{acc}X$ in the region V. The total forward energy is assumed to be zero. The Schrodinger equation becomes

$$\frac{-\hbar^2}{2m_0}\frac{d^2\varphi}{dX^2} - W\varphi = 0, \qquad \text{A.1}$$

in the region E, where $K'^2 = \frac{2m_0 W}{\hbar^2}$. The solution to the Schrodinger equation is

Appendix A (Continued)

$$\varphi = C_{+}e^{-iK'X} + C_{-}e^{iK'X} \qquad \text{A.2}$$

where the first part represents the reflected wave, the second part represents the transmitted wave, and C_{+}, C_{-} are complex amplitudes. The one-dimension probability current Π for $\varphi = C_{-}e^{iK'X}$ can be written as

$$\Pi = \frac{i\hbar}{2m_0}\left(\varphi\frac{d\varphi^*}{dX} - \varphi^*\frac{d\varphi}{dX}\right). \qquad \text{A.3}$$

The substitution of the solution to the Schrodinger equation further simplifies the probability current to

$$\Pi = |C_{-}|^2\frac{\hbar K'}{m_0}, \qquad \text{A.4}$$

where $|C_{-}|^2 = \frac{\Pi_u m_0}{\hbar K'}$ and Π_u is the probability current of unit magnitude; i.e., Π_u = 1 s^{-1}. The wave traveling to the right with a unit probability current is then given by

$$\varphi_{EL}^{UCN}(X) = \left(\frac{\Pi_u m_0}{\hbar K'}\right)^{\frac{1}{2}} e^{i\gamma} e^{iK'X}, \qquad \text{A.5}$$

where $e^{i\gamma}$ is a phase factor that can be chosen arbitrarily. The incident wave is partially reflected at the PE step and the reflected wave function can be written as

$$\varphi_{ER} = C_{Er}\left(\frac{\Pi_u m_0}{\hbar K'}\right)^{1/2} e^{iK'X}. \qquad \text{A.5}$$

Appendix A (Continued)

The unit current normalized wave function in region E is therefore given by

$$\varphi_E(X) = (\frac{\Pi_u m_0}{\hbar K'})^{\frac{1}{2}}(e^{i\gamma}e^{-iK'X} + C_{Er}e^{iK'X}). \qquad \text{A.6}$$

The Schrodinger equation in region V can be written as

$$\frac{-\hbar^2}{2m_0}\frac{d^2\varphi}{dX^2} + eE_{acc}X\varphi = 0. \qquad \text{A.7}$$

The equation can be further simplified to

$$\frac{d^2\varphi}{dX^2} - K^2 eFX\varphi = 0 \qquad \text{A.8}$$

where $K^2 = \frac{2m_0}{\hbar^2}$. With the introduction of a new dimensionless variable $x = K_A X = (K^2 eF)^{1/3}X$, the Schrodinger equation becomes $\frac{d^2\varphi}{dx^2} - x\varphi = 0$. The linearly independent Airy functions $Ai(x)$ and $Bi(x)$ can then be used to write the solution to the simplified Schrodinger equation as $\varphi(x) = C_A(Ai(x) - iBi(x))$, where C_A is the complex constant and $|C_A|^2 = \frac{\Pi_u \pi m_0}{\hbar K_A}$ can be found using the probability current equation. $\varphi(K_A X) = C_A[Ai(K_A X) - iBi(K_A X)]$ is now the wave function in the vacuum region and this can be simplified using Wronskian function, $[Ai(K_A X)Bi'(K_A X) - Bi(K_A X)Ai'(K_A X)] = 1/\pi$[122].

Appendix A (Continued)

The wave function in the region V is then

$$\varphi_V(K_A X) = C_V\left(\frac{\Pi_u \pi m_0}{\hbar K_A}\right)^{\frac{1}{2}}[Ai(K_A X) - iBi(K_A X)]. \qquad \text{A.9}$$

To find the constant C_V, boundary conditions are applied at the potential energy barrier X= L = $-w/_{eF}$, a new dimensionless parameter $\omega = \frac{K'}{K_A}$ is introduced, and the phase factor $\gamma = K'L$ is chosen. In addition, the notation $Ai(K_A L) = A$ and $Bi(K_A L) = B$ is used. The following are the equations employed from the boundary conditions to find the constant C_V that is at the end of the list;

$$\varphi_E|_{X=L} = \varphi_V|_{X=L}$$

$$C_V\left(\frac{K'\pi}{K_A}\right)^{1/2}[A - iB] = 1 + C_{Er}e^{iK'L}$$

$$\left.\frac{d\varphi_E}{dX}\right|_{X=L} = \left.\frac{d\varphi_V}{dX}\right|_{X=L} \qquad \text{A.10}$$

$$C_V\omega^{-1/2}\pi^{1/2}[iA' + B'] = 1 - C_{Er}e^{iK'L}$$

$$C_V = \frac{2}{\omega^{1/2}\pi^{1/2}[A - iB + \omega^{-1}(iA' + B')]}$$

Appendix A (Continued)

The ratio between the transmission probability current to the incident probability current is known as the transmission coefficient T; hence $T = |C_V|^2$. The transmission coefficient is therefore

$$T = \frac{1}{\frac{1}{2}+\frac{1}{4}\pi\omega(A^2+B^2)+\frac{1}{4}\pi\omega^{-1}(A'^2+B'^2)}, \qquad \text{A.11}$$

where $\omega = \frac{K'}{K_A} = \left(\frac{2m_0}{\hbar^2 e^2}\right)^{1/6} W^{1/2} E_{acc}^{-1/3}$.

APPENDIX B

ONE STEP PHOTOEMISSION SIMULATION CODE

The following Mathematica code represents the script that is used to obtain MTE values using the one-step photoemission simulation described in chapter 2. This code is used to obtain MTE values when effective mass is not equal to the free electron mass. In the first part, constants and input values are introduced, and then definitions are introduced. A control statement is used to keep the input values within the emitting band.

```
Remove["Global`*"]
(* Material Parameters *)
m0 = 1.0;
mT = 0.5(*0.42*);
mz = 1.0(*0.11,0.25*mT*);
Te = 300.0;
kBTe = (0.025/300.0)*Te;
W = 4.64 (*4.16,3.87,4.64Ag(100)*);
EF = 5.49 (*7.0Cu,1.2,5.49Ag*);
hw =(*4.67*)W + 0.0;
qE = 1.0;(* units eV/um *)
hbar = 0.0002763; (* units um.Sqrt[m0.eV] *)

(* DEFINITIONS *)
hqE = hbar*qE;
(* Threshold energy in band; MUST be positive *)
Eth = EF + W - hw;
pTth = 0.2*Sqrt[2.0*mT*Eth];
AA = Eth*((2.0*m0/(hqE*hqE))^(1/3));
BB = 0.5*((2.0*m0/(hqE*hqE))^(1/3));
CC = (2.0*m0*hqE)^(-1/3);
(* Local DOS x Barrier Transmission: f(E,pT) *)

T[e_, x_] = (4.0*mz*CC)/(2.0*CC*Sqrt[mz*(2.0*e - x*x/mT)] + Pi*CC*CC*mz*(2.0*e -
x*x/mT)*(AiryAi[AA - BB*(2.0*e - x*x/mT)]*AiryAi[AA -BB*(2.0*e - x*x/mT)] +AiryBi[AA - BB*(2.0*e -
x*x/mT)]*AiryBi[AA - BB*(2.0*e - x*x/mT)]) + Pi*(AiryAiPrime[AA -BB*(2.0*e -
x*x/mT)]*AiryAiPrime[AA - BB*(2.0*e - x*x/mT)] + AiryBiPrime[AA - BB*(2.0*e -
x*x/mT)]*AiryBiPrime[AA - BB*(2.0*e - x*x/mT)]));
(* Barrier Transmission: f(E,pT) ... no Local DOS *)
(* Electron Local DOS and Occupation; Fermi function *)

f[e_] = 1.0/(1.0 + Exp[(e - EF)/kBTe]);
Vza[e_, x_] = 1.0*m0*Sqrt[x*x + (Re[Sqrt[2.0*m0*(e - Eth) - x*x]])^2]* Re[Sqrt[2.0*m0*(e -Eth) -
x*x]]/Sqrt[2.0*m0*(e - Eth + 0.00000001) - x*x];
Vzb[x_] = 1.0*m0*Sqrt[x*x];
```

Appendix B (Continued)

```
(* Control statement; Zero outside band *)
Zero[e_, x_] = (Re[Sqrt[e]]/Sqrt[e + 0.00000001])*Re[Sqrt[2.0*e - x*x/mT]]/Sqrt[2.0*(e + 0.00000001) -
x*x/mT];

(* pT mesh definitions *)
(* Constant pT mesh size for QE calc., variable in general *)
dpT = 0.005(*pTth/ith*);
ith = pTth/dpT;
jmax = IntegerPart[Re[Sqrt[2.0*mT*(hw - W + 5.0*kBTe)]]/dpT];
imax = ith + jmax;
Elow = 0.002;(* units eV *)
kmax = 1.0*IntegerPart[Sqrt[2.0*m0*Elow]/dpT];

(* Above barrier energy; E > Eth *)
Ea[j_] = Eth + ((2.0*j - 1.0)*pTth + (j*(j - 1.0) + 0.5)*dpT)*dpT/(2.0*mT);
dEa[j_] = (pTth + (j - 0.5)*dpT)*dpT/mT;

(* Below barrier energy; E < Eth *)
Eb[k_] = Eth - ((2.0*k - 1.0)*pTth + (k*(k - 1.0) + 0.5)*dpT)*dpT/(2.0*mT);
dEb[k_] = (pTth - (k - 0.5)*dpT)*dpT/mT;

(* Normalization Factor: Above barrier emission at pT=0 *)
xx = 0.5*dpT;
Plot[(Zero[Ea[j], xx]*T[Ea[j], xx]*f[Ea[j]]*Vza[Ea[j], xx]), {j, 1, jmax}, {PlotRange -> All}]
T0a = Sum[(Zero[Ea[j], 0.5*dpT]*T[Ea[j], 0.5*dpT]*f[Ea[j]]*Vza[Ea[j], 0.5*dpT]*dEa[j]), {j, 1, jmax}];

(* Data Table: (pT,emission) *)
a = Table[{(i - 0.5)*dpT, Re[Sum[(Zero[Ea[j], (i - 0.5)*dpT]*T[Ea[j], (i - 0.5)*dpT]* f[Ea[j]]*Vza[Ea[j], (i -
0.5)*dpT]*dEa[j]), {j, 1, jmax}]]}, {i, 1, imax}];
ListPlot[Table[{a[[i, 1]], (a[[i, 2]]/T0a)}, {i, 1, imax}],
 Axes -> False, Frame -> True, PlotRange -> All, PlotStyle -> Red,
 Joined -> True]

(* Normalization Factor: Below barrier emission at pT=0 *)
Plot[(Zero[Eb[k], 0.5*dpT]*T[Eb[k], 0.5*dpT]*f[Eb[k]]*Vzb[0.5*dpT]), {k, 1, kmax}, {PlotRange -> All}]

(* Data Table: (pT,emission) *)
b = Table[{(i - 0.5)*dpT, Re[Sum[(Zero[Eb[k], (i - 0.5)*dpT]*T[Eb[k], (i - 0.5)*dpT]* f[Eb[k]]*Vzb[(i -
0.5)*dpT]*dEb[k]), {k, 1, kmax}]]}, {i, 1, imax}];

(* Normalization by above barrier constant for comparison *)
ListPlot[Table[{b[[i, 1]], (b[[i, 2]]/T0a)}, {i, 1, imax}], Axes -> False, Frame -> True, PlotRange -> All, PlotStyle
-> Red, Joined -> True]

(* Output: MTE via (DpT)^2 *)
st0 = Sum[(a[[i, 2]] + b[[i, 2]]), {i, 1, imax}];
st2 = Sum[(a[[i, 2]]*a[[i, 1]]*a[[i, 1]] + b[[i, 2]]*b[[i, 1]]*b[[i, 1]]), {i, 1, imax}];
MTEa =(1000.0/m0)*Sum[a[[i, 2]]*a[[i, 1]]*a[[i, 1]], {i, 1, imax}]/ Sum[a[[i, 2]], {i, 1, imax}]
MTEb = (1000.0/m0)*Sum[b[[i, 2]]*b[[i, 1]]*b[[i, 1]], {i, 1, imax}]/ Sum[b[[i, 2]], {i, 1, imax}]
MTEmeV = (1000.0/m0)*(st2/st0)

(* Photoemission Efficiency *)
etaPE = (10^6)* Sum[(i - 0.5)*dpT*dpT*(a[[i, 2]] + b[[i, 2]]), {i, 1, imax}]

(* PE efficiency normalized; e.g. to QE(W=hw) *)
normeta = etaPE/(11.6249)
```

APPENDIX C

CUBIC METAL PHOTOCATHODES

For completeness, I include the obtained experimental data for W(111) and Ta(001) single-crystal metal photocathodes in this appendix section. The measured MTE and QE values are compared to the prior photoemission theories. As in chapters 4 and 5, the Gobeli & Allen method[51] used to obtain the work function as the results clearly indicate that the quadratic relationship QE $=A.(\Delta E)^2$ is not valid for every material.

The W(111) photocathode

The measured spectral dependences of the QE and MTE for the single-crystal W(111) photocathode are shown by the data points in figures A.2 and A.3 respectively. The QE is compared to that predicted by Vecchione's poly-logarythmic formulation[19] (solid line) and the quadratic dependence on excess photoemission energy ΔE from Fowler and DuBridge[26,30] (dashed line). Although both prior photoemission theories appear to be good agreement with the experimental data, the insert of figure A.2 indicates that the QE follows a power law of $(\Delta E)^{2.7}$, which allows for the extraction of a work function value of 3.88eV using the Gobeli & Allen method. This is to be contrasted with a value of $\phi_{W(111)}$ = 4.55(±0.2)eV I determined from a DFT-based thin-slab calculation, which is within the range of the accepted value of 4.44(±0.21)eV for W(111)[41]. It is, however, ~0.67eV above the experimental value a discrepancy that is again likely due to a 1 (±0.5) monolayer surface oxide[97].

Appendix C (Continued)

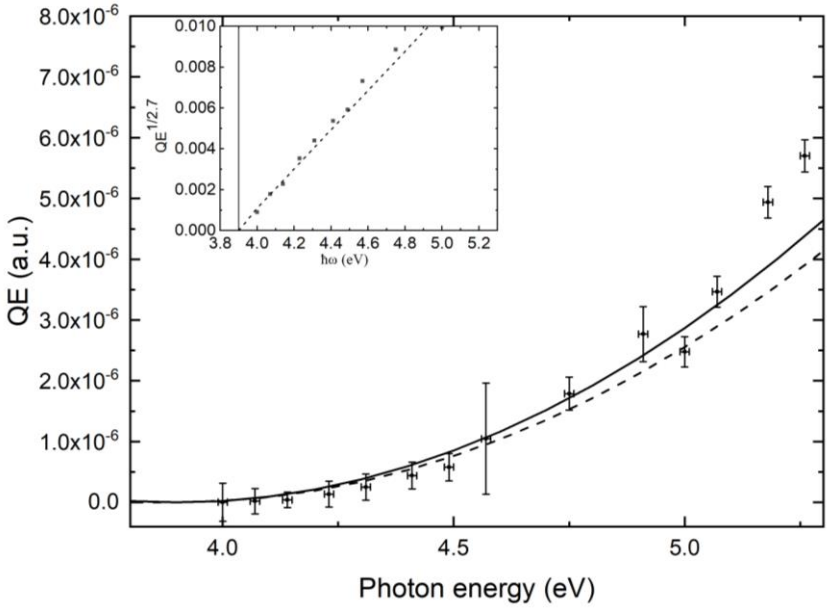

Figure A.2: Quantum efficiency (QE) per absorbed photon of W(111) as a function of incident UV photon energy (ħω): Experimental measurements (data points) and QE calculated using Vecchione theory[19] using E_f=7.45 eV[100] (equation 2.7) (solid black line); QE calculated using Fowler-Dubridge theory[30] [26] (QE = A.ΔE^2) (dashed black line). Inset: Extraction of the 3.88 eV work function (vertical line) using $(QE)^{1/2.7}$ vs. ħω.

In figure A.3, the measured spectral dependence of the MTE for W(111) is compared to Vecchione's poly-logarythmic formulation[19] (solid line) and the Dowell-Schmerge $\Delta E/3$ dependence (dashed line)[123] using the 3.88eV value for the work function determined from the QE data. The prior photoemission theories are again in good qualitative agreement with the experimental results with the clear exception that around the photoemission threshold the simple inclusion of the $k_B T_e$ = 25meV Boltzmann tail in Vecchione's analysis is insufficient – the measured MTE is significantly larger. This is, of course, primarily due to joint density of states, between the occupied band emission states and the vacuum states, in the photoemission process. In addition, the details of the dispersion of the emission band likely further contributes to the observed increase in the MTE over the $\Delta E/3$ dependence for incident photon energies below ~4.6eV (excess energies less than ~0.7eV).

Appendix C (Continued)

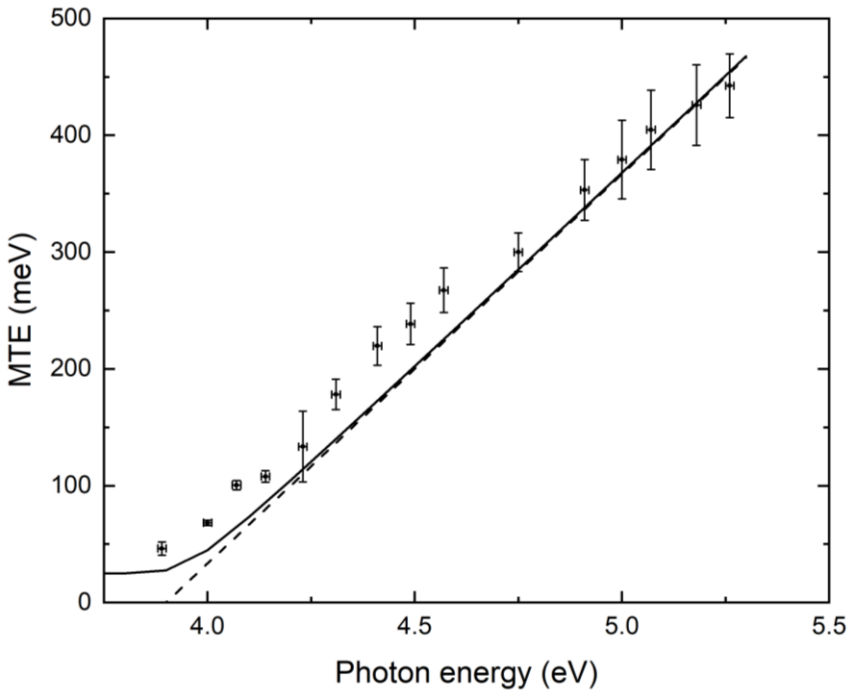

Figure A.3: Mean transverse energy of emitted electrons from W(111) and a function of incident UV photon energy (ħω): Experimental solenoid scan data with error bars (data points); MTE calculated using Vecchione theory with E_f=7.45 eV[100] (equation 2.6) (solid black line); MTE calculated using Dowell theory (MTE = $\Delta E/3$) (dashed black line).

The Ta(001) photocathode

Figures A.4 and A.5 display, respectively, the measured spectral dependences of the QE and MTE for the single-crystal Ta(001) photocathode (data points). The predicted spectral dependences of the QE from the prior photoemission theories of Vecchione et al.[19] (solid line) and Fowler and DuBridge[26,30] (dashed line) again compare favorably with the measurements: But, the insert in figure A.4 suggests that QE = $A.(\Delta E)^{2.8}$, where A is a constant, which allows a value of $\phi_{Ta(001)}$ = 3.78eV to be extracted using the method of Gobeli &

Appendix C (Continued)

Allen[51]. This is to be contrasted with a work function value of 4.4(±0.2) eV that I evaluated from a DFT-based thin-

slab calculation for a clean Ta(001) surface, which is close the accepted value of 4.10(±0.21)eV[41]. It is, however, ~0.6eV greater than the experimental value due to an oxide-related surface dipole. Tantalum is certainly well-known to readily form a Ta_2O_5 transparent UV surface oxide layer at room temperature.

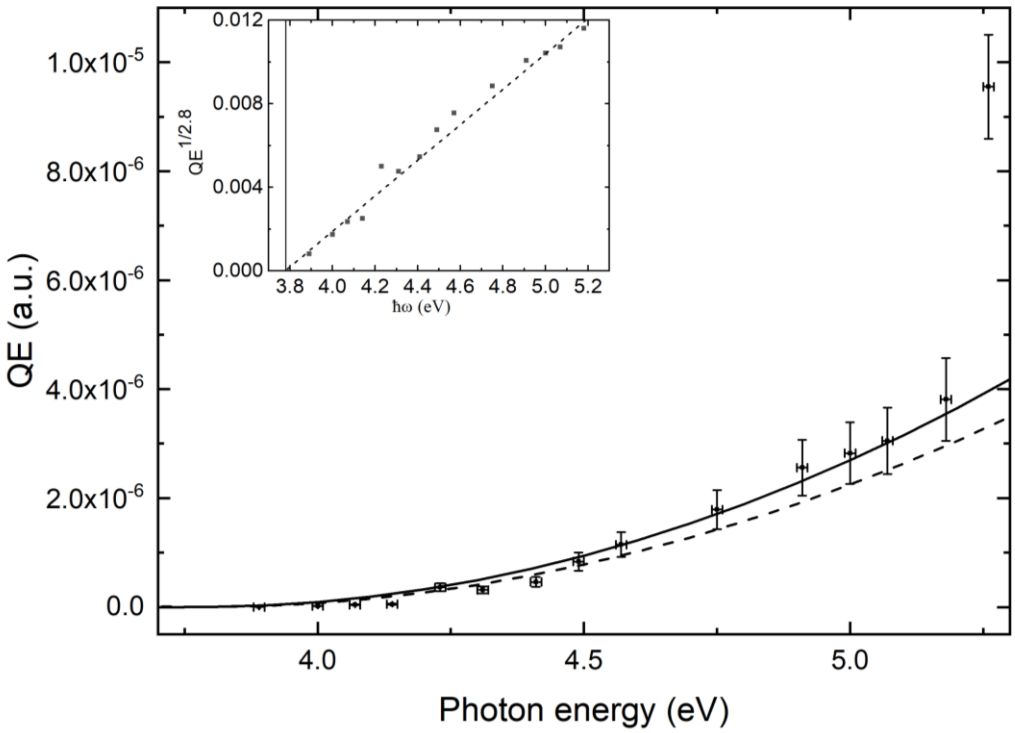

Figure A.4: Quantum efficiency (QE) per absorbed photon of Ta(001) as a function of incident UV photon energy (ħω): Experimental measurements (data points) and QE calculated using Vecchione theory[19] (equation 2.7) (solid black line); QE calculated using Fowler Dubridge theory[30] [26] (QE = A.ΔE^2) (dashed black line). Inset: Extraction of the 3.78 eV work function (vertical dotted line) using $(QE)^{1/2.8}$ vs. ħω.

In figure A.5, the measured spectral dependence of the MTE for Ta(001) is compared to Vecchione's poly-logarithmic formulation[19] (solid line) and the Dowell-Schmerge $\Delta E/3$

Appendix C (Continued)

dependence (dashed line)[123] using the 3.78eV value for the work function determined from the QE data. The prior photoemission theories are once again in good qualitative agreement with the experimental results with the exception that the measured MTE is ~25meV larger over the

whole spectral range. At excess photoemission energies near threshold, this discrepancy is primarily due to the density of states of the emitting band states and the recipient vacuum states. At larger excess energies, the dispersion of the one band contributing to photoemission in Ta(001) likely provides the reason for the small increase in MTE over the Dowell-Schmerge $\Delta E/3$ dependence.

Appendix C (Continued)

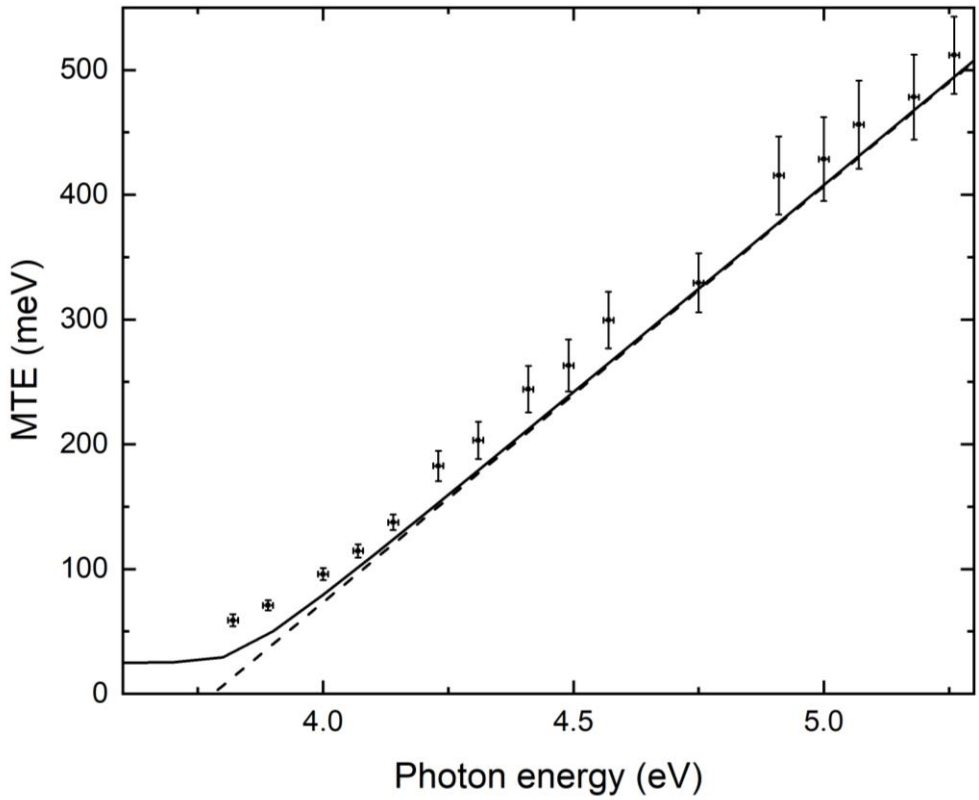

Figure A.5: Mean transverse energy of emitted electrons from Ta(001) and a function of incident UV photon energy (ħω): Experimental solenoid scan data with error bars (data points); MTE calculated using Vecchione theory (equation 2.6) (solid black line); MTE calculated using Dowell theory (MTE = $\Delta E/3$) (dashed black line).

APPENDIX D

ONE STEP PHOTOEMISSION SIMULATION FOR DEFECT STATES

In this appendix section, I include a description to the theoretical simulation used in chapter 6 for the emission from the defect states. The employed analysis for emission from a defect state assumes that it is the populated ground state of the isotropic Coulomb potential; that is, the hydrogenic 1*s* state of an exciton or F-center like state. In momentum space, the quantum wave function is therefore of the form

$$a(\mathbf{p}) = A\left[\frac{(\Delta p)^2}{(\Delta p)^2 + p^2}\right]^2 \qquad \text{A.12}$$

where Δp represents the characteristic width of the state for an electron mass $m_{0,}$ and A is the normalization constant. In principle, the analysis can be adapted for any square-integrable defect state wave function, such as the Gaussian ground state of the harmonic oscillator.

Coupling the initial momentum distribution of the electrons, associated with the modulus square of the wave function in equation (A), to our one-step photoemission analysis of Ref. 15 simply requires the decomposition of **p** into longitudinal p_z and transverse p_T components representing the virtual excited state wave function incident on the photoemission barrier from the bulk material. Integration over the longitudinal momentum p_z using the probability density of $a(\mathbf{p})$ as the local density of states (LDOS), the transmission coefficient for the triangular barrier generated by the applied acceleration field [38], and incorporating p_T conservation for above and below barrier photoemission [20] yields the transverse momentum distribution of the photo-emitted electrons for one energy with respect to the top of the barrier. To incorporate an energy width δE to the defect, further Gaussian distribution is used, and this

Appendix D (Continued)

is multiplied by a Fermi-Dirac distribution at the lattice temperature of the bulk to describe the energetic population distribution of the defect state.

As a result, this formalism allows one to model the case where a defect state 'pins' the position of the Fermi level, as is the case for doped semiconductors, for example. Integration over energy distribution of the populated states then gives the emitted transverse momentum distribution for one incident photon energy ħω; that is, the excess photoemission energy $\Delta E = \hbar\omega - \phi$. For the 1*s* momentum space wave function (Equation A), these transverse momentum distributions are Lorentzian-like truncated at the point where $p_T = \sqrt{2m_0\Delta E}$; that is the limit where the transverse motion of the emitted electron takes all the excess photoemission energy. Consequently, for consistency with the Analytical Gaussian electron pulse propagation model [11,23,24], which assumes a Gaussian electron momentum distribution and is employed to extract the MTE from the experimental measurements [21,124], a weighted least-squares Gaussian fit to the simulated transverse momentum distributions is performed to extract a comparative value for the MTE at each ΔE. A direct integration of transverse momentum distributions over p_T is also performed to yield a numerical value proportional to the quantum efficiency (QE) of emission

In our simulation of the oxygen vacancy defect state ~1 eV below the conduction band edge in HfO_2 [27], a full-width e^{-1} maximum (FWe^{-1}M) energy width of δE = 0.1 eV is used and the Fermi level, at the 3.35 eV work function below the vacuum level, is placed at the central average energy of the modeled 1*s* defect states. Their momentum width Δp is set to 0.54 $(m_0.\text{eV})^{1/2}$ as this provides an acceptable fit to the spectral MTE measurements for the Hf

Appendix D (Continued)

(0001)/HfO_2 photocathode when photoemission from both oxide layer and the underlying single-crystal metal are accounted for using their relative quantum efficiencies.

CITED LITERATURE

1. Chapman, H. N.; Barty, A.; Bogan, M. J.; Boutet, S.; Frank, M.; Hau-Riege, S. P.; Marchesini, S.; Woods, B. W.; Bajt, S.; Benner, W. H.; London, R. A.; Plönjes, E.; Kuhlmann, M.; Treusch, R.; Düsterer, S.; Tschentscher, T.; Schneider, J. R.; Spiller, E.; Möller, T.; Bostedt, C.; Hoener, M.; Shapiro, D. A.; Hodgson, K. O.; van der Spoel, D.; Burmeister, F.; Bergh, M.; Caleman, C.; Huldt, G.; Seibert, M. M.; Maia, F. R. N. C.; Lee, R. W.; Szöke, A.; Timneanu, N.; Hajdu, J. "Femtosecond Diffractive Imaging with a Soft-X-Ray Free-Electron Laser." *Nat. Phys.* 2 (12):839–843, 2006.

2. LaGrange, T.; Armstrong, M. R.; Boyden, K.; Brown, C. G.; Campbell, G. H.; Colvin, J. D.; DeHope, W. J.; Frank, A. M.; Gibson, D. J.; Hartemann, F. V.; Kim, J. S.; King, W. E.; Pyke, B. J.; Reed, B. W.; Shirk, M. D.; Shuttlesworth, R. M.; Stuart, B. C.; Torralva, B. R.; Browning, N. D. "Single-Shot Dynamic Transmission Electron Microscopy." *Appl. Phys. Lett.* 89 (4):044105, 2006.

3. Fritz, D. M.; Reis, D. A.; Adams, B.; Akre, R. A.; Arthur, J.; Blome, C.; Bucksbaum, P. H.; Cavalieri, A. L.; Engemann, S.; Fahy, S.; Falcone, R. W.; Fuoss, P. H.; Gaffney, K. J.; George, M. J.; Hajdu, J.; Hertlein, M. P.; Hillyard, P. B.; Horn-von Hoegen, M.; Kammler, M.; Kaspar, J.; Kienberger, R.; Krejcik, P.; Lee, S. H.; Lindenberg, A. M.; McFarland, B.; Meyer, D.; Montagne, T.; Murray, E. D.; Nelson, A. J.; Nicoul, M.; Pahl, R.; Rudati, J.; Schlarb, H.; Siddons, D. P.; Sokolowski-Tinten, K.; Tschentscher, T.; von der Linde, D.; Hastings, J. B. "Ultrafast Bond Softening in Bismuth: Mapping a Solid's Interatomic Potential with X-Rays." *Science (80-.).* 315 (5812):633–636, 2007.

4. van Oudheusden, T.; de Jong, E. F.; van der Geer, S. B.; 't Root, W. P. E. M. O.; Luiten, O. J.; Siwick, B. J. "Electron Source Concept for Single-Shot Sub-100 Fs Electron Diffraction in the 100 KeV Range." *J. Appl. Phys.* 102 (9):093501, 2007.

5. Miller, R. J. D. "Mapping Atomic Motions with Ultrabright Electrons: The Chemists' Gedanken Experiment Enters the Lab Frame." *Annu. Rev. Phys. Chem.* 65 (1):583–604, 2014.

6. Huang, Z.; Kim, K.-J. "Review of X-Ray Free-Electron Laser Theory." *Phys. Rev. Spec. Top. - Accel. Beams* 10 (3):034801, 2007.

7. Musumeci, P.; Moody, J. T.; Scoby, C. M.; Gutierrez, M. S.; Bender, H. A.; Wilcox, N. S. "High Quality Single Shot Diffraction Patterns Using Ultrashort Megaelectron Volt Electron Beams from a Radio Frequency Photoinjector." *Rev. Sci. Instrum.* 81 (1):013306, 2010.

8. Phillips, R. "Liouville's Theorem." *Pacific J. Math.* 28 (2):397–405, 1969.
9. Rickman, B. L.; Berger, J. A.; Nicholls, A. W.; Schroeder, W. A. "Intrinsic Electron Beam Emittance from Metal Photocathodes: The Effect of the Electron Effective Mass." *Phys. Rev. Lett.* 111 (23):237401, 2013.

10. Himpsel, F. J. "Angle-Resolved Measurements of the Photoemission of Electrons in the

Study of Solids." *Adv. Phys.* 32 (1):1–51, 1983.

11. Li, T.; Rickman, B. L.; Schroeder, W. A. "Emission Properties of Body-Centered Cubic Elemental Metal Photocathodes." *J. Appl. Phys.* 117 (13):134901, 2015.

12. Qian, H. J.; Li, C.; Du, Y. C.; Yan, L. X.; Hua, J. F.; Huang, W. H.; Tang, C. X. "Experimental Investigation of Thermal Emittance Components of Copper Photocathode." *Phys. Rev. Spec. Top. - Accel. Beams* 15 (4):040102, 2012.

13. Karkare, S.; Bazarov, I. "Effects of Surface Nonuniformities on the Mean Transverse Energy from Photocathodes." *Phys. Rev. Appl.* 4 (2):024015, 2015.

14. Smoluchowski, R. "Anisotropy of the Electronic Work Function of Metals." *Phys. Rev.* 60 (9):661–674, 1941.

15. Bazarov, I.; Rao, T. "Semiconductor Photocathodes for Unpolarized Electron Beams." In *An Engineering Guide to Photoinjectors*.

16. Mahan, G. D. "Theory of Photoemission in Simple Metals." *Phys. Rev. B* 2 (11):4334–4350, 1970.

17. Berglund, C. N.; Spicer, W. E. "Photoemission Studies of Copper and Silver: Theory." *Phys. Rev.* 136 (4A):A1030–A1044, 1964.

18. Dowell, D. H.; Schmerge, J. F. "Quantum Efficiency and Thermal Emittance of Metal Photocathodes." *Phys. Rev. Spec. Top. - Accel. Beams* 12 (7):074201, 2009.

19. Vecchione, T.; Dowell, D.; Wan, W.; Feng, J.; Padmore, H. A. "Quantum Efficiency and Transverse Momentum from Metals." In *FEL 2013: Proceedings of the 35th International Free-Electron Laser Conference*.

20. Schroeder, W. A.; Adhikari, G. "Evaluation of Photocathode Emission Properties in an Electron Gun: One-Step Photoemission from Bulk Band to Vacuum States." *New J. Phys.* 21 (3):033040, 2019.

21. Berger, J. A.; Greco, M. J.; Schroeder, W. A. "High-Power, Femtosecond, Thermal-Lens-Shaped Yb: KGW Laser." In *Optics InfoBase Conference Papers*.

22. Park, C.; Kim, C.; Kim, J.; Lee, Y.; Na, Y.; Lee, K.; Yeom, J. Y. "Performance Comparison between Ceramic Ce:GAGG and Single Crystal Ce:GAGG with Digital-SiPM." *J. Instrum.* 12 (01):P01002–P01002, 2017.

23. Berger, J. A.; Rickman, B. L.; Li, T.; Nicholls, A. W.; Andreas Schroeder, W. "Excited-State Thermionic Emission in III-Antimonides: Low Emittance Ultrafast Photocathodes." *Appl. Phys. Lett.* 101 (19):194103, 2012.

24. Berger, J. A.; Schroeder, W. A. "Semianalytic Model of Electron Pulse Propagation: Magnetic Lenses and Rf Pulse Compression Cavities." *J. Appl. Phys.* 108 (12):124905, 2010.

25. Adhikari, G.; Riley, P.; Schroeder, W. A. “Spectral Characterization of a Rh(110) Photocathode: Band Structure Interpretation.” *AIP Adv.* 9 (6):065305, 2019.

26. DuBridge, L. A. “Theory of the Energy Distribution of Photoelectrons.” *Phys. Rev.* 43 (9):727–741, 1933.

27. Karkare, S.; Adhikari, G.; Schroeder, W. A.; Nangoi, J. K.; Arias, T.; Maxson, J.; Padmore, H. “Ultracold Electrons via Near-Threshold Photoemission from Single-Crystal Cu(100).” No. 1002020.

28. Einstein, A. “On the Electrodynamics of Moving Bodies (Zur Elektrodynamik Bewegter Körper).” *Ann. Phys.* 1905.

29. Dowell, D. H.; King, F. K.; Kirby, R. E.; Schmerge, J. F.; Smedley, J. M. “In Situ Cleaning of Metal Cathodes Using a Hydrogen Ion Beam.” *Phys. Rev. Spec. Top. - Accel. Beams* 9 (6):063502, 2006.

30. Fowler, R. H. “The Analysis of Photoelectric Sensitivity Curves for Clean Metals at Various Temperatures.” *Phys. Rev.* 38 (1):45–56, 1931.

31. Schottky, W. “Über Kalte Und Warme Elektronenentladungen.” *Zeitschrift für Phys.* 14 (1):63–106, 1923.

32. Fowler, R. H.; Nordheim, L. “Electron Emission in Intense Electric Fields.” *Proc. R. Soc. London. Ser. A, Contain. Pap. a Math. Phys. Character* 119 (781):173–181, 1928.

33. Nordheim, L. “Zur Theorie Der Thermischen Emission Und Der Reflexion von Elektronen an Metallen.” *Zeitschrift f**r Phys.* 46 (11–12):833–855, 1928.

34. Rokhlenko, A. “Strong Field Electron Emission and the Fowler–Nordheim–Schottky Theory.” *J. Phys. A Math. Theor.* 44 (5):055302, 2011.

35. Jeffreys., H. “The Effect on Love Waves of Heterogeneity in the Lower Layer.” *Geophys. J. Int.* 2101–111, 1928.

36. Gadzuk, J. W.; Plummer, E. W. “Field Emission Energy Distribution (FEED).” *Rev. Mod. Phys.* 45 (3):487–548, 1973.

37. Jensen, K. L.; Ganguly, A. K. “Numerical Simulation of Field Emission and Tunneling: A Comparison of the Wigner Function and Transmission Coefficient Approaches.” *J. Appl. Phys.* 73 (9):4409–4427, 1993.

38. Forbes, R. G.; Deane, J. H. B. “Transmission Coefficients for the Exact Triangular Barrier: An Exact General Analytical Theory That Can Replace Fowler & Nordheim’s 1928 Theory.” *Proc. R. Soc. A Math. Phys. Eng. Sci.* 467 (2134):2927–2947, 2011.

39. Feng, J.; Nasiatka, J.; Wan, W.; Karkare, S.; Smedley, J.; Padmore, H. A. “Thermal Limit to the Intrinsic Emittance from Metal Photocathodes.” *Appl. Phys. Lett.* 107 (13):134101, 2015.

40. Pankove, J. I.; Kiewit, D. A. “Optical Processes in Semiconductors.” *J. Electrochem. Soc.* 119 (5):156C, 1972.

41. Derry, G. N.; Kern, M. E.; Worth, E. H. “Recommended Values of Clean Metal Surface Work Functions.” *J. Vac. Sci. Technol. A Vacuum, Surfaces, Film.* 33 (6):060801, 2015.

42. Karkare, S.; Feng, J.; Chen, X.; Wan, W.; Palomares, F. J.; Chiang, T.-C.; Padmore, H. A. “Reduction of Intrinsic Electron Emittance from Photocathodes Using Ordered Crystalline Surfaces.” *Phys. Rev. Lett.* 118 (16):164802, 2017.

43. Jensen, K. L.; O’Shea, P. G.; Feldman, D. W.; Shaw, J. L. “Emittance of a Field Emission Electron Source.” *J. Appl. Phys.* 107 (1):014903, 2010.

44. Bradley, D. J.; Allenson, M. B.; Holeman, B. R. “The Transverse Energy of Electrons Emitted from GaAs Photocathodes.” *J. Phys. D. Appl. Phys.* 10 (1):111–125, 1977.

45. Karkare, S.; Bazarov, I. “Effect of Nanoscale Surface Roughness on Transverse Energy Spread from GaAs Photocathodes.” *Appl. Phys. Lett.* 98 (9):094104, 2011.

46. Zhang, Z.; Tang, C. “Analytical Study on Emittance Growth Caused by Roughness of a Metallic Photocathode.” *Phys. Rev. Spec. Top. - Accel. Beams* 18 (5):053401, 2015.

47. Nangoi, J. K.; Arias, T. A.; Karkare, S.; Padmore, H. A.; Schroeder, W. A. “The Role of Electron-Phonon Scattering in Transverse Momentum Conservation in PbTe(111) Photocathodes.” In *Proceedings of the 9th International Particle Accelerator Conference, Vancouver, BC, Canada*; pp 1414–1416.

48. Wooten, F.; Hernandez, J. P.; Spicer, W. E. “Photoemission and Electron Scattering in Cs 3 Bi and Cs 3 Sb.” *J. Appl. Phys.* 44 (3):1112–1117, 1973.

49. Weaire, D. “Band Effective Masses for Nineteen Elements.” *Proc. Phys. Soc.* 92 (4):956–961, 1967.

50. L. Cultrera. “Photoemission Research at Cornell University: Recent Advances and Future Perspectives.” In *European Workshop on Photocathodes for Particle Accelerator Applications (EWPAA)*; Berlin.

51. Gobeli, G. W.; Allen, F. G. “Photoelectric Properties of Cleaved GaAs, GaSb, InAs, and InSb Surfaces; Comparison with Si and Ge.” *Phys. Rev.* 137 (1A):A245–A254, 1965.

52. Chen, G.; Adhikari, G. D.; Kovi, K. K.; Antipov, S. P.; Jing, C.; Spentzouris, L.; Schroeder, A.; Baryshev, S. V. “Study of Mean Transverse Energy of (N)UNCD with Tunable Laser Source; Study of Mean Transverse Energy of (N)UNCD with Tunable Laser Source.” 1677–1679, 2018.

53. Giannozzi, P.; Baroni, S.; Bonini, N.; Calandra, M.; Car, R.; Cavazzoni, C.; Ceresoli, D.; Chiarotti, G. L.; Cococcioni, M.; Dabo, I.; Dal Corso, A.; de Gironcoli, S.; Fabris, S.; Fratesi, G.; Gebauer, R.; Gerstmann, U.; Gougoussis, C.; Kokalj, A.; Lazzeri, M.; Martin-Samos, L.; Marzari, N.; Mauri, F.; Mazzarello, R.; Paolini, S.; Pasquarello, A.; Paulatto, L.; Sbraccia, C.; Scandolo, S.; Sclauzero, G.; Seitsonen, A. P.; Smogunov, A.;

Umari, P.; Wentzcovitch, R. M. "QUANTUM ESPRESSO: A Modular and Open-Source Software Project for Quantum Simulations of Materials." *J. Phys. Condens. Matter* 21 (39):395502, 2009.

54. Kresse, G.; Marsman, M.; Jürgen, F. "Data Description and Simple Inference." In *Handbook of Statistical Analyses Using SAS, Second Edition*; Chapman and Hall/CRC.

55. Gonze, X. "A Brief Introduction to the ABINIT Software Package." *Zeitschrift für Krist. - Cryst. Mater.* 220 (5/6):2005.

56. Clark, S. J.; Segall, M. D.; Pickard, C. J.; Hasnip, P. J.; Probert, M. I. J.; Refson, K.; Payne, M. C. "First Principles Methods Using CASTEP." *Zeitschrift für Krist. - Cryst. Mater.* 220 (5/6):2005.

57. Monkhorst, H. J.; Pack, J. D. "Special Points for Brillouin-Zone Integrations." *Phys. Rev. B* 13 (12):5188–5192, 1976.

58. Li, T.; Rickman, B. L.; Schroeder, W. A. "Density Functional Theory Analysis of Hexagonal Close-Packed Elemental Metal Photocathodes." *Phys. Rev. Spec. Top. - Accel. Beams* 18 (7):073401, 2015.

59. Kokalj, A. "Computer Graphics and Graphical User Interfaces as Tools in Simulations of Matter at the Atomic Scale." *Comput. Mater. Sci.* 28 (2):155–168, 2003.

60. Elstner, M.; Porezag, D.; Jungnickel, G.; Elsner, J.; Haugk, M.; Frauenheim, T.; Suhai, S.; Seifert, G. "Self-Consistent-Charge Density-Functional Tight-Binding Method for Simulations of Complex Materials Properties." *Phys. Rev. B* 58 (11):7260–7268, 1998.

61. Li, T. "Photoelectric Emission Properties of Photocathode Materials," University of Illinois at Chicago.

62. Janert, P. K. *Gnuplot in Action: Understanding Data With Graphs*.

63. Perdew, J. P.; Burke, K.; Ernzerhof, M. "Generalized Gradient Approximation Made Simple." *Phys. Rev. Lett.* 77 (18):3865–3868, 1996.

64. Marzari, N.; Vanderbilt, D.; De Vita, A.; Payne, M. C. "Thermal Contraction and Disordering of the Al(110) Surface." *Phys. Rev. Lett.* 82 (16):3296–3299, 1999.

65. Arblaster, J. W. "Crystallographic Properties of Ruthenium." *Platin. Met. Rev.* 57 (2):127–136, 2013.

66. Lang, N. D.; Kohn, W. "Theory of Metal Surfaces: Work Function." *Phys. Rev. B* 3 (4):1215–1223, 1971.

67. Schulte, F. K. "Chemical Potentials and Workfunctions of Metal Surfaces in the Theory of an Inhomogeneous Electron Gas." *J. Phys. C Solid State Phys.* 7 (20):L370–L373, 1974.

68. Fall, C. J.; Binggeli, N.; Baldereschi, A. "Deriving Accurate Work Functions from Thin-

Slab Calculations." *J. Phys. Condens. Matter* 11 (13):2689–2696, 1999.

69. Methfessel, M.; Hennig, D.; Scheffler, M. "Trends of the Surface Relaxations, Surface Energies, and Work Functions of the 4 d Transition Metals." *Phys. Rev. B* 46 (8):4816–4829, 1992.

70. Rossky, P. J.; Doll, J. D.; Friedman, H. L. "Brownian Dynamics as Smart Monte Carlo Simulation." *J. Chem. Phys.* 69 (10):4628–4633, 1978.

71. Vinet, L.; Zhedanov, A. "A 'Missing' Family of Classical Orthogonal Polynomials." *J. Phys. A Math. Theor.* 44 (8):085201, 2011.

72. Brunner, F.; Spühler, G. J.; Aus der Au, J.; Krainer, L.; Morier-Genoud, F.; Paschotta, R.; Lichtenstein, N.; Weiss, S.; Harder, C.; Lagatsky, A. A.; Abdolvand, A.; Kuleshov, N. V.; Keller, U. "Diode-Pumped Femtosecond Yb:KGd(WO_4)_2 Laser with 11-W Average Power." *Opt. Lett.* 25 (15):1119, 2000.

73. Chenais, S.; Balembois, F.; Druon, F.; Lucas-Leclin, G.; Georges, P. "Thermal Lensing in Diode-Pumped Ytterbium Lasers-Part II: Evaluation of Quantum Efficiencies and Thermo-Optic Coefficients." *IEEE J. Quantum Electron.* 40 (9):1235–1243, 2004.

74. Boulon, G. "Yb3+-Doped Oxide Crystals for Diode-Pumped Solid State Lasers: Crystal Growth, Optical Spectroscopy, New Criteria of Evaluation and Combinatorial Approach." *Opt. Mater. (Amst).* 22 (2):85–87, 2003.

75. Holtom, G. R. "Mode-Locked Yb:KGW Laser Longitudinally Pumped by Polarization-Coupled Diode Bars." *Opt. Lett.* 31 (18):2719, 2006.

76. Rimington, N. W.; Schieffer, S. L.; Schroeder, W. A.; Brickeen, B. K. "Thermal Lens Shaping in Brewster Gain Media: A High-Power, Diode-Pumped Nd:GdVO4 Laser." *Opt. Express* 12 (7):1426, 2004.

77. https://www.limo.de https://www.limo.de.

78. Paunescu, G.; Hein, J.; Sauerbrey, R. "100-Fs Diode-Pumped Yb:KGW Mode-Locked Laser." *Appl. Phys. B* 79 (5):555–558, 2004.

79. Biswal, S.; O'Connor, S. P.; Bowman, S. R. "Thermo-Optical Parameters Measured in Ytterbium-Doped Potassium Gadolinium Tungstate." *Appl. Opt.* 44 (15):3093, 2005.

80. Brunner, F.; Innerhofer, E.; Marchese, S. V.; Südmeyer, T.; Paschotta, R.; Usami, T.; Ito, H.; Kurimura, S.; Kitamura, K.; Arisholm, G.; Keller, U. "Powerful Red-Green-Blue Laser Source Pumped with a Mode-Locked Thin Disk Laser." *Opt. Lett.* 29 (16):1921, 2004.

81. Layertec optical coatings https://www.layertec.de/en/.

82. Schieffer, S. L.; Berger, J. A.; Rickman, B. L.; Nayyar, V. P.; Schroeder, W. A. "Thermal Effects in Semiconductor Saturable-Absorber Mirrors." *J. Opt. Soc. Am. B* 29 (4):543, 2012.

83. Rickman, B. L. “Electron Sources and Column Components for Ultrafast Electron Microscopy,” University of Illinois.

84. Buch, F.; Fahrenbruch, A. L.; Bube, R. H. “Photovoltaic Properties of Five II-VI Heterojunctions.” *J. Appl. Phys.* 48 (4):1596–1602, 1977.

85. Crewe, A. V.; Eggenberger, D. N.; Wall, J.; Welter, L. M. “Electron Gun Using a Field Emission Source.” *Rev. Sci. Instrum.* 39 (4):576–583, 1968.

86. Rose, J.; Graves, W.; Heese, R.; Johnson, E.; Krinsky, S.; Sheehy, B. “Modeling and Measurements of the DUVFEL Photoinjector Cavity Rf Properties.” In *PACS2001. Proceedings of the 2001 Particle Accelerator Conference (Cat. No.01CH37268)*; IEEE: Chicago; **Vol. 3**, pp 2221–2223.

87. Christensen, N. E. “The Band Structure of Rhodium and Its Relation to Photoemission Experiments.” *Phys. Status Solidi* 55 (1):117–127, 1973.

88. Borstel, G.; Braun, W.; Neumann, M.; Seitz, G. “Band Structure of Rhodium and Photoemission from Its Low Index Surfaces.” *Phys. Status Solidi* 95 (2):453–460, 1979.

89. Chen, J. K.; Tzou, D. Y.; Beraun, J. E. “A Semiclassical Two-Temperature Model for Ultrafast Laser Heating.” *Int. J. Heat Mass Transf.* 49 (1–2):307–316, 2006.

90. Weaver, J. H.; Olson, C. G.; Lynch, D. W. “Optical Investigation of the Electronic Structure of Bulk Rh and Ir.” *Phys. Rev. B* 15 (8):4115–4118, 1977.

91. Swank, R. K. “Surface Properties of II-VI Compounds.” *Phys. Rev.* 153 (3):844–849, 1967.

92. Kiskinova, M. “Surface Structure and Reactivity: Reactions on Face-Centered Cubic (110) Metal Surfaces Involving Adatom-Induced Reconstructions.” *Chem. Rev.* 96 (4):1431–1448, 1996.

93. Dandliker, R. B.; Conner, R. D.; Johnson, W. L. “Melt Infiltration Casting of Bulk Metallic-Glass Matrix Composites.” *J. Mater. Res.* 13 (10):2896–2901, 1998.

94. Seydel, U.; Kitzel, W. “Thermal Volume Expansion of Liquid Ti, V, Mo, Pd, and W.” *J. Phys. F Met. Phys.* 9 (9):L153–L160, 1979.

95. Fu, C. L.; Ho, K. M. “First-Principles Calculation of the Equilibrium Ground-State Properties of Transition Metals: Applications to Nb and Mo.” *Phys. Rev. B* 28 (10):5480–5486, 1983.

96. Iverson, R. .; Hodges, L. “Molybdenum: Band Structure, Fermi Surface, and Spin-Orbit Interaction.” *Phys. Rev. B* 8 (4):1429–1432, 1973.

97. Greiner, M. T.; Chai, L.; Helander, M. G.; Tang, W.-M.; Lu, Z.-H. “Metal/Metal-Oxide Interfaces: How Metal Contacts Affect the Work Function and Band Structure of MoO 3.” *Adv. Funct. Mater.* 23 (2):215–226, 2013.

98. Fehlner, F. P.; Mott, N. F. “Low-Temperature Oxidation.” *Oxid. Met.* 2 (1):59–99, 1970.

99. M. N. Polyanskiy. Refractive index database https://refractiveindex.info/?shelf=main&book=Mo&page=Werner (accessed Oct 4, 2020).

100. Loucks, T. L. "Fermi Surfaces of Cr, Mo, and W by the Augmented-Plane-Wave Method." *Phys. Rev.* 139 (4A):A1181–A1188, 1965.

101. Christensen, N. E.; Feuerbacher, B. "Volume and Surface Photoemission from Tungsten. I. Calculation of Band Structure and Emission Spectra." *Phys. Rev. B* 10 (6):2349–2372, 1974.

102. Monaghan, S.; Hurley, P. K.; Cherkaoui, K.; Negara, M. A.; Schenk, A. "Determination of Electron Effective Mass and Electron Affinity in HfO2 Using MOS and MOSFET Structures." *Solid. State. Electron.* 53 (4):438–444, 2009.

103. Chen, G.; Adhikari, G.; Spentzouris, L.; Kovi, K. K.; Antipov, S.; Jing, C.; Andreas Schroeder, W.; Baryshev, S. V. "Mean Transverse Energy of Ultrananocrystalline Diamond Photocathode." *Appl. Phys. Lett.* 114 (9):093103, 2019.

104. Gritsenko, V. A.; Perevalov, T. V.; Islamov, D. R. "Electronic Properties of Hafnium Oxide: A Contribution from Defects and Traps." *Phys. Rep.* 6131–20, 2016.

105. Papernov, S.; Brunsman, M. D.; Oliver, J. B.; Hoffman, B. N.; Kozlov, A. A.; Demos, S. G.; Shvydky, A.; Cavalcante, F. H. M.; Yang, L.; Menoni, C. S.; Roshanzadeh, B.; Boyd, S. T. P.; Emmert, L. A.; Rudolph, W. "Optical Properties of Oxygen Vacancies in HfO 2 Thin Films Studied by Absorption and Luminescence Spectroscopy." *Opt. Express* 26 (13):17608, 2018.

106. Janthon, P.; Luo, S. (Andy); Kozlov, S. M.; Viñes, F.; Limtrakul, J.; Truhlar, D. G.; Illas, F. "Bulk Properties of Transition Metals: A Challenge for the Design of Universal Density Functionals." *J. Chem. Theory Comput.* 10 (9):3832–3839, 2014.

107. Jepsen, O.; Andersen, O. K.; Mackintosh, A. R. "Electronic Structure of Hcp Transition Metals." *Phys. Rev. B* 12 (8):3084–3103, 1975.

108. Jain, A.; Ong, S. P.; Hautier, G.; Chen, W.; Richards, W. D.; Dacek, S.; Cholia, S.; Gunter, D.; Skinner, D.; Ceder, G.; Persson, K. A. "Commentary: The Materials Project: A Materials Genome Approach to Accelerating Materials Innovation." *APL Mater.* 1 (1):011002, 2013.

109. Altmann, S. L.; Bradley, C. J. "The Band Structure of Hexagonal Close-Packed Metals II. Sc, Ti, Y and Zr." *Proc. Phys. Soc.* 92 (3):764–775, 1967.

110. Leung, T. C.; Kao, C. L.; Su, W. S.; Feng, Y. J.; Chan, C. T. "Relationship between Surface Dipole, Work Function and Charge Transfer: Some Exceptions to an Established Rule." *Phys. Rev. B* 68 (19):195408, 2003.

111. Allred, A. L. "Electronegativity Values from Thermochemical Data." *J. Inorg. Nucl. Chem.* 17 (3–4):215–221, 1961.

112. Schaeffer, J. K.; Gilmer, D. C.; Capasso, C.; Kalpat, S.; Taylor, B.; Raymond, M. V.; Triyoso, D.; Hegde, R.; Samavedam, S. B.; White, B. E. "Application of Group Electronegativity Concepts to the Effective Work Functions of Metal Gate Electrodes on High-κ Gate Oxides." *Microelectron. Eng.* 84 (9–10):2196–2200, 2007.

113. Bae, J. K.; Cultrera, L.; DiGiacomo, P.; Bazarov, I. "Rugged Spin-Polarized Electron Sources Based on Negative Electron Affinity GaAs Photocathode with Robust Cs 2 Te Coating." *Appl. Phys. Lett.* 112 (15):154101, 2018.

114. Perevalov, T. V.; Aliev, V. S.; Gritsenko, V. A.; Saraev, A. A.; Kaichev, V. V. "Electronic Structure of Oxygen Vacancies in Hafnium Oxide." *Microelectron. Eng.* 10921–23, 2013.

115. Rieke, R. D.; Rhyne, L. D. "Preparation of Highly Reactive Metal Powders. Activated Copper and Uranium. The Ullmann Coupling and Preparation of Organometallic Species." *J. Org. Chem.* 44 (19):3445–3446, 1979.

116. Corin Michael Ricardo Greaves. "Metal Photocathodes for Free Electron Laser Applications," University of California, Berkley.

117. Karkare, S.; Feng, J.; Maxson, J.; Padmore, H. A. "Development of a 3-D Energy-Momentum Analyzer for MeV-Scale Energy Electrons." *Rev. Sci. Instrum.* 90 (5):053902, 2019.

118. Zhu, Y. D.; Yan, M. F.; Zhang, Y. X.; Zhang, C. S. "First-Principles Investigation of Structural, Mechanical and Electronic Properties for Cu–Ti Intermetallics." *Comput. Mater. Sci.* 12370–78, 2016.

119. Burdick, G. A. "Energy Band Structure of Copper." *Phys. Rev.* 129 (1):138–150, 1963.

120. Ueba, H.; Gumhalter, B. "Theory of Two-Photon Photoemission Spectroscopy of Surfaces." *Prog. Surf. Sci.* 82 (4–6):193–223, 2007.

121. Papanicolaou, N. I.; Lagaris, I. E.; Evangelakis, G. A. "Modification of Phonon Spectral Densities of the (001) Copper Surface Due to Copper Adatoms by Molecular Dynamics Simulation." *Surf. Sci.* 337 (1–2):L819–L824, 1995.

122. Varlamov, V. "Fractional Derivatives of Products of Airy Functions." *J. Math. Anal. Appl.* 337 (1):667–685, 2008.

123. Dowell, D. H.; Schmerge, J. F. "Erratum: Quantum Efficiency and Thermal Emittance of Metal Photocathodes [Phys. Rev. ST Accel. Beams 12 , 074201 (2009)]." *Phys. Rev. Spec. Top. - Accel. Beams* 12 (11):119901, 2009.

124. Michalik, A. M.; Sipe, J. E. "Analytic Model of Electron Pulse Propagation in Ultrafast Electron Diffraction Experiments." *J. Appl. Phys.* 99 (5):054908, 2006.

VITA

GOWRI ADHIKARI

gowriadhikari89@gmail.com
scholar.google.com/citations?user=A4ba61YAAAAJ&hl=en

EDUCATION

- **University of Illinois at Chicago (UIC). Chicago, IL**

Ph.D. in Physics. Aug 2015 – present
M.Sc. in Physics. Dec 2018

- **University of Peradeniya. Sri Lanka**

B.Sc. (Hons) in Physics. Jan 2015

PUBLICATIONS

1. S karkare, **G. Adhikari**, W. A. Schroeder, et.al., "Ultracold electrons via near-threshold photoemission from single-crystal Cu(100) Submitted to Physical Review Letters.

2. A.Galdi, L. Cultrera, W.A. Schroeder, **G. Adhikari**, W.H. Li, J.M. Maxson, H. Paik, D.G. Schlom, C. Parzyck, E.B. Lochocki, K.M. Shen, I.V. Bazarov, "Low energy photoemission from (100) Ba1−xLaxSnO3 thin films for photocathode applications" Eur. Phys. J. Special Topics 228, 713 (2019).

3. **G. Adhikari**, P. Riley and W. A. Schroeder, "Spectral characterization of a Rh (110) photocathode: Band structure interpretation" AIP Advances 9(6), 065305 (2019).

4. W. A Schroeder and **G. Adhikari**," Evaluation of photocathode emission properties in an electron gun: One-step photoemission from bulk-band to vacuum states" New Journal of Physics 21 033040 (2019).

5. G. Chen, **G. Adhikari**, L. Spentzious, K. K. Kovi, S. Antipoy, C. Jing, W. A. Schroeder and S. V. Baryshev, "Mean transverse energy of Ultracrystaline Diamond Photocathode" Applied Physics Letters,114 (09) 093103 (2019).

6. G.Chen, **G. Adhikari**, S. Antipov, E.Gomez, T. Nikhar, L. Spentzouris, W.A. Schroeder and S. V. Baryshev "Study of the mean transverse energy and the emission mechanism of (N)UNCD photocathodes." NAPAC (2019).

7. G.Chen, **G. Adhikari**, K. K Kovi, S. Antipov, C. Jing, L. Spentzouris, A. Schroeder and S. V. Baryshev "Study of mean transverse energy of (N)UNCD with tunable laser source." IPAC 1677 (2019).

8. A. Galdi, E. B Lochocki, H. Paik, C. T. Parazyck, D. G. Schlom, K. M. Shen, **G. Adhikari**, W. A Schroeder, I. V. Bazarov, L. Cultrera, W. H. Li, J. M. Maxson and C. M. Pierce, "Barium Tin Oxide Ordered photocathodes: First measurements and future perspectives" IPAC 1597 (2018).

9. S. S. Karkare, **G. Adhikari**, H. A. Padmore, W. A. Schroeder "Intrinsic emittance of single crystal cathodes" IPAC 4263 (2018).

10. W. A. Schroeder and **G. Adhikari**," Spectral Intrinsic Emittance Measurements of Mo (001) and PbTe (111) Photocathodes" European Workshop on Photocathodes for Particle Accelerator Application (EWPAA 2017).

PRESENTATIONS

1. Physics Fest: University of Illinois at Chicago, 2019

2. **G. Adhikari**, W. A. Schroeder*. "**Spectral characterization of single crystal photocathodes**".
European Workshop on Photocathodes for Particle Accelerator Application,2019

3. W.A. Schroeder*, **G. Adhikari**. "**Benchmarking photocathode performance to Ab initio theory**".
Photocathode Physics for Photoinjectors (P3) Workshop, 2018

4. **G. Adhikari**, W. A. Schroeder*. "**One-step photoemission simulation: Exact triangular barrier solution with bulk & vacuum electronic states**".
Photocathode Physics for Photoinjectors (P3) Workshop, 2018

5. **G. Adhikari**, W.A. Schroeder*. "**Band structure interpretation of Mo(001) and W(100) spectral emission properties**".
European Workshop on Photocathodes for Particle Accelerator Application,2017